

# UC Davis

## UC Davis Electronic Theses and Dissertations

### Title

EPR Characterization of the Radical SAM Enzyme HydG, Actinides, and Organic Radicals

### Permalink

<https://escholarship.org/uc/item/55x658b5>

### Author

Villarreal, David

### Publication Date

2023

Peer reviewed|Thesis/dissertation

EPR Characterization of the Radical SAM enzyme HydG, Actinides, and Organic Radicals

By

DAVID GERALDO VILLARREAL  
DISSERTATION

Submitted in partial satisfaction of the requirements for the degree of

DOCTOR OF PHILOSOPHY

in

Chemistry and Chemical Biology

in the

OFFICE OF GRADUATE STUDIES

of the

UNIVERSITY OF CALIFORNIA

DAVIS

Approved:

---

R. David Britt, Chair

---

David Goodin

---

Matthew Augustine

Committee in Charge

2023

## Acknowledgements

I would first like to thank Professor R. David Britt, for giving me the opportunity to learn about EPR and Mössbauer spectroscopy in his group. For his mentorship and support in the continuation of my career. The Department of Chemistry and Chemical Biology at UC Davis for the acceptance into their graduate program. My undergraduate mentor, Professor William Armstrong, for taking me into his research group at Boston College. This set me on a path with inorganic chemistry that continues to this day.

I would also like to thank my lab mates, coworkers, and former students. My lab mates Dr. Paul Stucky, Dr. Guodong Rao, Dr. Lizhi Tao, Dr. Aidin Balo, Dr. Khetpakorn Chakarawet, Dr. Mark Nesbit, Dr. Gary Chow, Dr. David Marchiori, Dr. Richard Sayler, Dr. Jarett Wilcoxon, Wen Fu, Trisha Nguyen, and Liam Twomey who all made this dissertation possible. From helping me understand biochemistry to spectroscopy, everyone has played a role in my graduate education and research accomplishments. My former administrators Dr. James P. Rader and Dr. Tiffeney Brown who consistently demonstrated leadership and kindness in the workplace. My former co-worker Brian Montgomery, who spent his entire career educating students in chemistry. From this I learned the importance to inspire the next generation of scientists. I also want to thank all my former high school chemistry students that made teaching exciting and so much fun.

Finally, I want to thank my family for their unconditional love and support. For always believing in me and supporting my career choices.

## Abstract

Many enzymes utilize metallocofactors to catalyze chemical transformations important to creating a sustainable world. Our research focuses on using electron paramagnetic resonance (EPR) spectroscopy as our main tool to study these metallocofactors, and the transformations that they catalyze. My research has more specifically involved the bio-assembly of the active site found in [FeFe]-hydrogenase enzymes. [FeFe]-hydrogenases are the most active enzymes in the production of molecular hydrogen. Their energetic efficiency and capacity to reduce protons to form H<sub>2</sub> makes hydrogenases important research targets in this context of renewable energy and sustainability. These [FeFe]-hydrogenase enzymes contain an active site H-cluster, consisting of a [4Fe-4S]<sub>H</sub> cluster linked to a [2Fe]<sub>H</sub> subcluster with CO, CN<sup>-</sup> and azadithiolate ligands. The research presented here focuses on understanding the biosynthesis of this H-cluster active site, and the role that the radical *S*-adenosyl-L-methionine (SAM) maturase enzyme HydG plays. The overall HydG reaction converts tyrosine, cysteine, and Fe(II) to the [Fe(II)(CN)(CO)<sub>2</sub>(cysteinate)]<sup>-</sup> product, Complex B. This HydG product is a diamagnetic (*S* = 0) low spin Fe(II) complex and is thus undetectable by EPR spectroscopy. We chose to use <sup>57</sup>Fe Mössbauer spectroscopy to probe the chemical environment of the Complex B Fe, even in its diamagnetic state. I observed evidence of the product Fe species, during HydG turnover by <sup>57</sup>Fe Mössbauer spectroscopy. With low isomer shifts and small quadrupolar splitting, the results are consistent with the expected low spin ferrous product of Complex B. I was able to observe this species in both fully and selectively <sup>57</sup>Fe labeled HydG experiments. The product Complex B subsequently serves as the substrate for the following radical SAM enzyme HydE, which activates the inert low spin Fe(II) complex for dimerization, either within HydE or on the protein HydF. This dimerization results in the formation of an Fe<sub>2</sub>S<sub>2</sub>(CO)<sub>4</sub>(CN)<sub>2</sub> species needing only the addition of the CH<sub>2</sub>NHCH<sub>2</sub> component of the adt bridge to complete the binuclear subcluster.



In addition to the work with radical SAM maturase enzymes, I have worked on several collaborations through EPR spectroscopy. I present work in collaboration with John Arnold's group at UC Berkeley, examining the electronic structure of Actinide compounds. We successfully observed a Uranium(III) species that was reduced to an EPR silent integer spin Uranium(II). I also present recent work in collaboration with Alan Balch's group here at UC Davis, where we observed and characterized the formation of DABCO radical species.

## Table of Contents

<b>1. Introduction to Spectroscopic Methods</b> .....	1
1.1. Introduction to Electron Paramagnetic (EPR) Spectroscopy.....	1
1.1.1. Spin Magnetic Moment and the Influence of Magnetic Fields.....	1
1.1.2. The Hyperfine Interaction.....	5
1.1.3. Anisotropy in $g$ and $A$ .....	8
1.1.4. The Quadrupole Interaction.....	10
1.1.5. Zero-Field Splitting.....	11
1.1.6. The Full Spin Hamiltonian.....	13
1.1.7. Electron Nuclear Double Resonance (ENDOR) Spectroscopy.....	14
1.2. Introduction to Mössbauer Spectroscopy.....	19
1.2.1. The Mössbauer Effect.....	19
1.2.2. The Mössbauer Transmission Spectrum.....	20
1.2.3. Mössbauer Hyperfine Interactions.....	22
1.2.3.1. The Mössbauer Isomer shift ( $\delta$ ).....	23
1.2.3.2. Quadrupolar Splitting ( $\Delta E_Q$ ).....	25
1.2.3.3. The Magnetic Dipole Moment.....	26
1.2.3.4. Combined Electric and Magnetic Hyperfine Interactions.....	28
1.3. References.....	29
<b>2. Radical S-adenosyl methionine (SAM) enzyme HydG and the Biosynthesis of the [FeFe]-hydrogenase H-cluster active site</b> .....	30
2.1. Introduction to Radical S-adenosyl methionine (SAM) enzymes.....	30
2.2. Introduction to [FeFe]-hydrogenase and the H-cluster.....	33
2.3. The Catalytic Mechanism for the Radical SAM enzyme HydG.....	38
2.4. Materials and Methods.....	46
2.4.1. Expression and Purification of HydG.....	46

2.4.2. Sample Preparation.....	47
2.4.3. Continuous-wave (CW) EPR Spectroscopy & Mössbauer spectroscopy.....	47
2.5. Zero-Field Splitting of the Aux-Cluster in HydG.....	48
2.6. Catalytic Turnover of HydG at Extended Periods.....	56
2.6.1. Regenerating Resting State HydG with L-Cysteine.....	64
2.7. HydG Mutants Y97F & R327K.....	69
2.7.1. Preparing Site-Specific Mutations.....	71
2.7.2. Results of Site-Specific Mutations on Catalytic Turnover.....	71
2.7.3. HydG <sup>R327K</sup> and HydG <sup>Y97F</sup> with Non-natural Substrates.....	75
2.8. References.....	77
<b>3. Characterizing the biosynthesis of the [Fe(II)(CN)(CO)<sub>2</sub>(cysteinate)]<sup>-</sup> organometallic product from fully labeled <sup>57</sup>Fe HydG.....</b>	<b>83</b>
3.1. <sup>57</sup> Fe Mössbauer of [FeFe]-hydrogenase and Biomimetic compounds.....	83
3.2. Oxidation states and Spin Dependent delocalization of Iron-Sulfur Clusters.....	84
3.3. <sup>57</sup> Fe Mössbauer and EPR Spectroscopy of fully labeled HydG.....	86
3.3.1. Expression and Purification of <sup>57</sup> Fe HydG.....	86
3.3.2. Materials and Methods.....	88
3.3.3. Observing the [Fe(II)(CN)(CO) <sub>2</sub> (cysteinate)] <sup>-</sup> product, Complex B, by <sup>57</sup> Fe Mössbauer Spectroscopy.....	88
3.4. References.....	95
<b>4. Characterizing the biosynthesis of the [Fe(II)(CN)(CO)<sub>2</sub>(cysteinate)]<sup>-</sup> organometallic product from selectively labeled <sup>57</sup>Fe HydG.....</b>	<b>96</b>
4.1. Introduction to the “dangler” Fe of HydG.....	96
4.1.1. Metal chelators removing the Dangler Fe.....	97
4.1.2. Preparing <sup>57</sup> Fe dangler labeled HydG.....	99
4.1.3. Observing the [Fe(II)(CN)(CO) <sub>2</sub> (cysteinate)] <sup>-</sup> product, Complex B, by <sup>57</sup> Fe Mössbauer Spectroscopy in selectively labeled HydG.....	101
4.2. <sup>57</sup> Fe Mössbauer of SynB.....	109
4.3. Discussion of <sup>57</sup> Fe Mössbauer Results for Fully and Selectively Labeled Experiments.....	110
4.4. Preparation of <sup>57</sup> Fe SynB.....	113

4.4.1. Preparation of $^{57}\text{FeBr}_2$ .....	113
4.4.2. Preparation of $\text{K}_2^{57}\text{Fe}_2(\text{CO})_8$ .....	114
4.4.3. $^{57}\text{Fe}_3(\text{CO})_{12}$ .....	115
4.4.4. Preparation of $^{57}\text{Fe}(\text{CO})_5$ (in THF).....	117
4.4.5. Preparation of $\text{Et}_4\text{N}[^{57}\text{Fe}(\text{CO})_4(\text{CN})]$ .....	119
4.4.6. Preparation of $^{57}\text{Fe}$ Syn-B.....	121
4.6. References.....	123
<b>5. Electron Paramagnetic Resonance (EPR) characterization of Actinide Compounds and Free Radicals.....</b>	<b>127</b>
5.1. Introduction to EPR of heavy elements.....	127
5.2. Uranium(II) that acts like a Uranium (I) Synthron Introduction.....	128
5.2.1. Uranium(II) that acts like a Uranium (I) Synthron.....	129
5.2.2. EPR of Uranium(II) that acts like a Uranium (I) Synthron.....	131
5.2.3. EPR of Uranium(II) that acts like a Uranium (I) Synthron Discussion.....	139
5.3. Introduction to EPR Spectroscopy of free radicals.....	139
5.3.1. Generating DABCO Free Radicals.....	140
5.3.2. X-band CW EPR of DABCO Free Radicals.....	141
5.3.3. Pulsed ENDOR of DABCO Radical Intermediate Species.....	143
5.3.4. Simulating X-band CW EPR of DABCO Radicals.....	145
5.4. Materials and Methods.....	147
5.5. References.....	148

## List of Figures & Tables

Figure 1.1.1.1. Electron Spin Magnetic Moment.....	1
Figure 1.1.1.2. Electron Zeeman Interaction.....	4
Figure 1.1.2. Energy level diagram $S = \frac{1}{2}, I = \frac{1}{2}$ .....	6
Figure 1.1.3.1. Principal axes for a paramagnetic system.....	8
Figure 1.1.3.2. Spectral envelopes for a $S = \frac{1}{2}$ system in the solid state.....	9
Figure 1.1.4. Energy level diagram $S = \frac{1}{2}, I = 1$ .....	11
Figure 1.1.5.1. Weak Zero-Field Splitting, $S = 1$ .....	12
Figure 1.1.5.2. Strong Zero-Field Splitting, $S = 5/2$ .....	13
Figure 1.1.7.1. Energy level diagram(s) $S = \frac{1}{2}, I = \frac{1}{2}$ , ENDOR Response.....	16
Figure 1.1.7.2. Energy level diagram $S = \frac{1}{2}, I = 1$ , ENDOR Response.....	17
Figure 1.1.7.3. Schematic Representation of Mims & Davies ENDOR.....	18
Figure 1.2.1. Decay Scheme of $^{57}\text{Co}$ and Resonant Absorption.....	19
Figure 1.2.2. Schematic Representation of a Mössbauer Transmission Experiment.....	22
Figure 1.2.3.1. The Mössbauer Isomer shift.....	24
Figure 1.2.3.2. Mössbauer Quadrupole Splitting.....	25
Figure 1.2.3.3. The Magnetic Dipole Moment.....	27
Scheme 2.1.1. General Mechanism of Radical SAM Enzymes.....	30
Figure 2.1.1. EPR Spectrum and Simulation of 5'-dAdo Radical.....	32
Scheme 2.2.1. Maturation of apo-HydA.....	33
Scheme 2.2.2. Potential Mechanism of [FeFe]-hydrogenase.....	35
Scheme 2.2.3. Sequential Model in the Biosynthesis of the H-Cluster.....	37
Figure 2.3.1. Crystal Structure of HydG.....	38
Scheme 2.3.1. Proposed Mechanism of L-Tyr Cleavage by HydG.....	40
Scheme 2.3.2. Proposed Mechanism at Auxiliary Cluster of HydG.....	41
Figure 2.3.2. EPR Spectrum and Simulation of HydG after 24s Turnover.....	43
Figure 2.3.3. EPR Spectra of HydG displaying both Fe-S Clusters.....	44

Figure 2.3.4. EPR Spectrum and Simulation of HydG after 60 min Turnover.....	45
Figure 2.5.1. Exchange Coupling Scheme of Auxiliary Cluster of HydG.....	48
Equation 2.5.1. EPR Intensity/Amplitude relationship with Zero-Field Splitting.....	49
Figure 2.5.2. Temperature dependence EPR Spectra of <i>SoHydG</i> Auxiliary Cluster.....	50
Figure 2.5.3. Temperature dependence data fit #1 for <i>SoHydG</i> .....	51
Equation 2.5.2. EPR Intensity/Amplitude relationship to Boltzmann distribution.....	52
Figure 2.5.4. Temperature dependence data fit #2 for <i>SoHydG</i> .....	52
Figure 2.5.5. Temperature dependence EPR Spectra of <i>TiHydG</i> Auxiliary Cluster.....	53
Figure 2.5.6. Temperature dependence data fit #1 for <i>TiHydG</i> .....	54
Figure 2.5.7. Temperature dependence data fit #2 for <i>TiHydG</i> .....	55
Figure 2.6.1. EPR Spectra time points for HydG #1.....	57
Figure 2.6.2. EPR Spectrum and Simulation of HydG after 20 min Turnover.....	58
Figure 2.6.3. Percent weight of EPR Species.....	59
Figure 2.6.4. EPR Spectra time points for HydG #2.....	60
Figure 2.6.5. EPR Spectrum and Simulation of HydG after 18 min Turnover.....	61
Figure 2.6.6. EPR Spectra Comparison of 18 and 60 min Turnover HydG.....	62
Figure 2.6.7. EPR Spectrum and Simulation of HydG after 60 min Turnover.....	63
Figure 2.6.1.1. EPR Spectra of HydG turnover in presence of L-Cys.....	65
Figure 2.6.1.2. EPR Spectra of <sup>13</sup> C-labeled L-Cys and L-Tyr turnover with HydG.....	66
Figure 2.6.1.3. ENDOR Spectrum <sup>13</sup> C-labeled L-Cys and L-Tyr turnover with HydG.....	67
Figure 2.6.1.4. EPR Spectra time dependence after addition of L-Cys.....	68
Figure 2.7.1. Crystal Structure of HydG Active Site.....	70
Figure 2.7.2.1. EPR Spectra after 24s Turnover for HydG <sup>wt</sup> and HydG <sup>R327K</sup> .....	73
Figure 2.7.2.2. EPR Spectra after 24s Turnover for HydG <sup>wt</sup> and HydG <sup>Y97F</sup> .....	73
Figure 2.7.2.3. EPR Spectra time points Turnover of HydG <sup>Y97F</sup> .....	74
Table 2.7.3.1. Non-natural Substrates and Catalytic activity.....	75
Table 3.1.1. Mössbauer parameters for low spin Fe in [FeFe]-hydrogenase.....	83
Figure 3.2.1. Fe-S Clusters Oxidation States.....	85

Figure 3.3.1.1. Fe Standard Curve.....	88
Figure 3.3.3.1. EPR Spectra of Fully labeled <sup>57</sup> Fe HydG.....	90
Figure 3.3.3.2. Mössbauer Spectrum of Resting State <sup>57</sup> Fe HydG.....	91
Figure 3.3.3.3. Mössbauer Spectrum of Resting State <sup>57</sup> Fe HydG with Simulation.....	91
Table 3.3.3.1. Mössbauer Fitting Parameters for Figure 3.3.3.3.....	92
Figure 3.3.3.4. EPR Spectrum and Simulation of Fully labeled <sup>57</sup> Fe HydG 60 min Turnover.....	92
Figure 3.3.3.5. Side by Side Mössbauer Spectra Comparison Fully labeled <sup>57</sup> Fe HydG.....	93
Figure 3.3.3.6. Overlaid Mössbauer Spectra Comparison Fully labeled <sup>57</sup> Fe HydG.....	93
Figure 3.3.3.7. Difference Spectrum and Simulation <sup>57</sup> Fe HydG.....	94
Figure 4.1.1.1. EPR Spectra HydG Treated with Metal Chelators.....	98
Figure 4.1.1.2. EPR Spectra HydG Treated with Metal Chelators at Low Field.....	99
Figure 4.1.2.1. Side by Side Mössbauer Spectra Comparison Reconstitution.....	100
Figure 4.1.3.1. EPR Spectra of Selectively labeled <sup>57</sup> Fe HydG.....	102
Figure 4.1.3.2. Mössbauer Spectrum of Resting State Selective <sup>57</sup> Fe HydG.....	103
Figure 4.1.3.3. Mössbauer Spectrum of Resting State Selective <sup>57</sup> Fe HydG with Simulation...	103
Table 4.1.3.1. Mössbauer Fitting Parameters for Figure 4.1.3.3.....	104
Figure 4.1.3.4. EPR Spectrum and Simulation of Selectively labeled <sup>57</sup> Fe HydG 60 min.....	105
Figure 4.1.3.5. Side by Side Mössbauer Spectra Comparison Selectively labeled <sup>57</sup> Fe HydG...	106
Figure 4.1.3.6. Overlaid Mössbauer Spectra Comparison Selectively labeled <sup>57</sup> Fe HydG.....	107
Figure 4.1.3.7. Difference Spectrum and Simulation Selectively labeled <sup>57</sup> Fe HydG.....	108
Figure 4.2.1. Mössbauer Spectrum and Simulation of <sup>57</sup> Fe Syn-B.....	110
Table 4.3.1. Mössbauer parameters Fe in Complex B, SynB, and Biomimetic Compounds.....	111
Scheme 4.4.1. Preparation of <sup>57</sup> Fe SynB.....	113
Figure 4.4.3.1. IR spectrum of <sup>57</sup> Fe <sub>3</sub> (CO) <sub>12</sub> in a THF solution at 22 °C.....	116
Figure 4.4.3.2. HR-MS spectrum of <sup>57</sup> Fe <sub>3</sub> (CO) <sub>12</sub> .....	116
Figure 4.4.4.1. IR spectra of <sup>57</sup> Fe(CO) <sub>5</sub> in THF solutions with varied concentrations at 22 °C..	118
Figure 4.4.4.2. Calibration plot of concentration of <sup>57</sup> Fe(CO) <sub>5</sub> and peak area.....	118
Figure 4.4.5.1. Negative-ion ESI mass spectrum of Et <sub>4</sub> N[ <sup>57</sup> Fe(CO) <sub>4</sub> (CN)]......	120

Figure 4.4.5.2. IR spectra of dried $^{57}\text{Fe}(\text{CO})_5$ .....	121
Figure 4.4.6.1. IR spectra of Syn-B and $^{57}\text{Fe}$ Syn-B in MeOH at 22 °C.....	122
Scheme 5.2.1. Synthesis of the Uranium Bis(Arene) Complex.....	129
Figure 5.2.1. X-ray Crystal Structures of 2 and 3.....	130
Figure 5.2.2.1. EPR Spectrum of a solid sample of 3.....	133
Figure 5.2.2.2. EPR Spectrum and Simulation of a solid sample of 4.....	134
Figure 5.2.2.3. EPR Spectra in Perpendicular and Parallel mode of 3.....	135
Figure 5.2.2.4. EPR Spectra in Perpendicular and Parallel mode of 4.....	136
Figure 5.2.2.5. EPR Spectra of Temperature Dependence of 4.....	137
Figure 5.2.2.6. Field-swept echo-detected EPR spectrum of 4 measured at 130 GHz.....	138
Scheme 5.3.1. Generation of free DABCO radical(s).....	140
Figure 5.3.2. EPR Spectra of DABCO with $\text{SbCl}_5$ at various time points.....	142
Figure 5.3.3.1. Q-band Davies-ENDOR of DABCO reaction mixture quenched at 10 s.....	143
Figure 5.3.3.2. Q-band Davies-ENDOR of DABCO reaction mixture quenched at 5 s.....	144
Figure 5.3.4. EPR of the $\text{DABCO}^{\bullet+}$ radical and Total Simulation.....	146



# Chapter 1

## Introduction to Spectroscopic Methods

### 1.1. Introduction to Electron Paramagnetic Resonance (EPR) Spectroscopy

Electron Paramagnetic Resonance spectroscopy (EPR) is a magnetic resonance technique used to study paramagnetic systems. In the area of chemistry and biochemistry, paramagnetic systems are often encountered as organic free radicals or transition metal ions with unpaired electrons.<sup>1</sup> EPR spectra of these unpaired electrons provides invaluable information on the environment and electronic geometry of the system under study. This Section will give a brief and concise overview on the theoretical background of EPR spectroscopy that has been applied in the research presented in subsequent Chapters.

#### 1.1.1. Spin Magnetic Moment and the Influence of Magnetic Fields

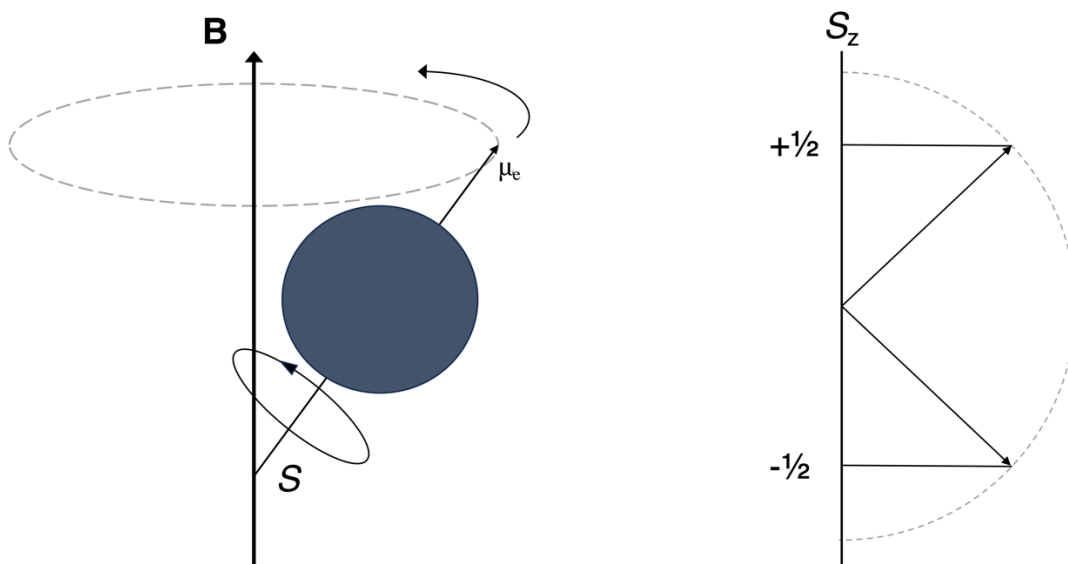


**Figure 1.1.1.1.** (Left) Electron with magnetic moment  $\mu_e$  precessing around an applied magnetic field (**B**). (Right) Representation of the space quantization of the electron spin angular momentum for a  $S = 1/2$ .

It is convenient to consider an electron as a particle of mass  $m_e$  and charge  $e$  rotating about an axis with spin angular momentum  $\mathbf{S}$ . The allowed orientations for the spin angular momentum along the z-axis are given by the  $m_s$  values of the spin, where  $m_s$  is the electron spin angular momentum quantum number, with  $2S+1$  values in integral steps between  $+S$  and  $-S$ :

$$m_s = -S, -S+1 \dots S-1, S$$

This unpaired electron can be thought of as a moving charged particle that will produce a current generating a magnetic dipole moment ( $\mu_e$ ) (**Figure 1.1.1.1**). The magnetic dipole  $\mu_e$  is related to the gyromagnetic ratio by the following equation:

$$\mu_e = -\gamma \mathbf{S} \hbar = -g_e \frac{e\hbar}{2m_e} \mathbf{S}$$

Here  $g_e$  is the free-electron g-factor, with an approximate value of 2.0023. This equation is

commonly expressed in terms of the Bohr magneton ( $\beta = \frac{e\hbar}{2m_e} = 9.274 \times 10^{-24} \text{ J T}^{-1}$ ):

$$\mu_e = -g_e \beta \mathbf{S}$$

The negative sign in the equation is due to the negative charge on the electron and the assignment that  $g_e$  and  $\beta$  are both positive values. This indicates that the magnetic moment is collinear and anti-parallel to the direction of the spin angular momentum (**Figure 1.1.1.1**).

The electron spin states are degenerate in the absence of a magnetic field, but this degeneracy is removed as soon as an external magnetic field ( $\mathbf{B}$ ) is applied (the magnetic field  $\mathbf{B}$  is taken to be along the z-axis). The z-component of the electron's magnetic moment ( $\mu_z$ ) along the applied magnetic field can be related to the  $m_s$  spin states, resulting in two magnetic dipole moments (for  $m_s = \pm 1/2$ ).

$$\mu_z = -g_e \beta m_s$$

The energy of the interaction between the electron magnetic moment and the axis aligned along the external magnetic field can be represented by:

$$E = -\mu_z \mathbf{B}$$

Substituting the expression for the magnetic dipole moment results in the following energy term:

$$E = g_e \beta m_s \mathbf{B}$$

The two components of the magnetic dipole along the z-direction give two states of different energy, stabilized when aligned parallel to the applied field and destabilized when aligned antiparallel. The interaction of these magnetic moments with  $\mathbf{B}$  is called the *Zeeman effect* or *Zeeman interaction* (**Figure 1.1.1.2.**)<sup>2</sup> The magnitude of this effect varies linearly with the intensity of  $\mathbf{B}$ .

In an EPR spectroscopy experiment, a paramagnetic sample is placed in an external magnetic field  $\mathbf{B}$  causing the unpaired electron spin states to align parallel or antiparallel to the field. The sample is then irradiated with electromagnetic radiation ( $h\nu$ ). When the energy quantum ( $h\nu$ ) matches the energy difference ( $\Delta E$ ) between electron spin states, resonance absorption occurs flipping the spin (**Figure 1.1.1.2.**):

$$\Delta E = h\nu = g_e \beta \mathbf{B}.$$

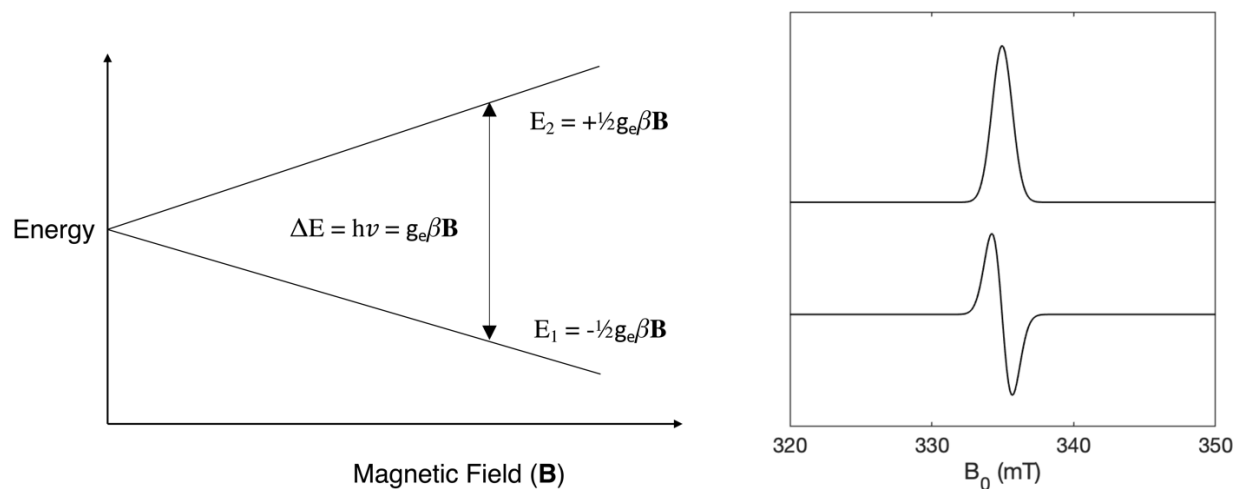


**Figure 1.1.1.2.** (Left) The electron Zeeman interaction, displaying the energy levels for an unpaired electron in an external magnetic field. (Right) Resonant energy absorption leading to an electron spin flip resulting in an EPR signal. EPR signal displayed as an absorption (Top) and first derivative (Bottom).<sup>1</sup>

The selection rule for EPR transitions to occur is  $\Delta m_s = \pm 1$ , which is required to conserve angular momentum. To find the conditions for which resonance can occur, either the frequency of electromagnetic radiation or the magnetic field strength can be varied while holding the other constant. Conventionally, standard instrumentation has utilized a fixed frequency (commonly between 3-36 GHz) and a variable magnetic field.<sup>1,3</sup> In addition, as the temperature is lowered the population of spins in the more stable orientation will increase due to the Boltzmann distribution. With more spins being in the lower energy state, the probability of absorbing microwaves will also be increased. The sensitivity is therefore improved at lower temperature, with most experiments being run between 4–77K.

### 1.1.2. The Hyperfine Interaction

The presence of nuclei with magnetic spin ( $I$ ) adds further magnetic interactions to the paramagnetic spin system, which can result in multiline EPR spectra. For isotopes with nuclear spin, an interaction with the magnetic field  $\mathbf{B}$  will result in *nuclear Zeeman splitting*. The interaction between the nuclear magnetic moment and the unpaired electron is described by the hyperfine interaction.

Nuclei that possess a non-zero nuclear spin quantum number,  $I$ , will have an associated magnetic moment analogous to an unpaired electron:

$$\mu_N = g_N \beta_N I$$

Where  $g_N$  is the effective nuclear g-factor,  $\beta_N$  is the nuclear magneton ( $\beta_N = \frac{e\hbar}{2m_p} = 5.0508 \times 10^{-27}$  J T<sup>-1</sup>), and  $m_p$  is the mass of a proton. In the presence of an applied magnetic field, a nucleus can adopt  $2I+1$  orientations, as specified by the allowed values of  $m_I$ .

$$m_I = -I, -I+1 \dots I-1, I$$

Like the spin of an unpaired electron, the z-component of the nuclear magnetic dipole moment is related to the nuclear spin,  $m_I$ , by:

$$\mu_z = g_N \beta_N m_I$$

The degeneracy of the  $2I+1$  nuclear energy levels is removed by the influence of a magnetic field. The energy of individual nuclear Zeeman levels is given by:

$$E = g_N \beta_N m_I \mathbf{B}$$

The gap between Zeeman energy levels is related through the gyromagnetic ratio and magnetic field,  $\gamma \mathbf{B}$ , which gives smaller splitting's than the electron Zeeman separation due to the smaller value for  $\beta_N$ .

For an unpaired electron interacting with a nuclear magnetic moment, each of the non-degenerate electron Zeeman levels will split into  $2I+1$  nuclear Zeeman levels. For a simple  $S = \frac{1}{2}$ ,  $I = \frac{1}{2}$  system, this would result into four discrete energy levels and two EPR allowed transitions separated by the strength of the hyperfine interaction. (**Figure 1.1.2.**)

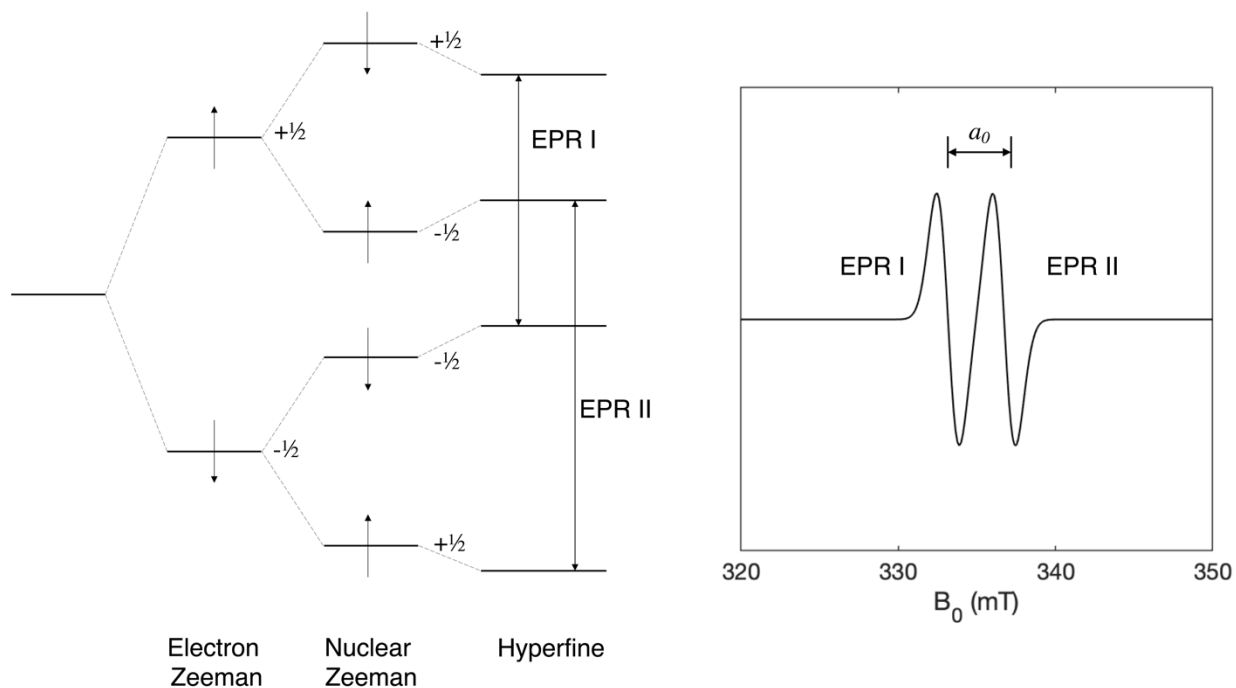


**Figure 1.1.2.** (Left) Energy level diagram with a fixed magnetic field for a  $S = \frac{1}{2}$  and  $I = \frac{1}{2}$  system. Labeled are the electron Zeeman interaction, nuclear Zeeman interaction, and resulting is hyperfine perturbation. (Right) EPR spectrum showing the two transitions due to the hyperfine interaction on the unpaired electron and the magnitude of the isotropic hyperfine interaction  $a_0$ .<sup>1</sup>

The electron spin energies can be summarized as:

$$E = g_e\beta m_s \mathbf{B} - g_N\beta_N m_l \mathbf{B} + a m_s m_l$$

The final term  $a m_s m_l$  arises from the interaction between the electron and nuclear magnetic dipole moments. The extent of the perturbation to the energy levels is reflected in the magnitude

by the hyperfine splitting  $a$ . Two factors contribute to the hyperfine interaction arising from the space inside and outside of the nuclear volume. These are the isotropic ( $a_0$ ) and anisotropic or dipolar interactions ( $T$ ).

Inside the nucleus, the hyperfine originating from the nuclear magnetic dipole is constant in all directions. This hyperfine interaction is called the isotropic hyperfine interaction ( $a_0$ ), or Fermi contact interaction and is a result of the probability that the unpaired electron will be at the nucleus. The magnitude of the experimentally observed isotropic hyperfine coupling can be related to the spin density located at a specific nucleus. The second contribution to the hyperfine interaction arises from a dipole-dipole interaction ( $T$ ), due to the hyperfine interaction through the space external to the nucleus. The energy of this dipole interaction depends on the orientation and distance between the electron and nuclear magnetic dipole moments. If the molecule containing the unpaired electron is rapidly tumbling, the anisotropy with respect to the external field is averaged. Dipole-dipole hyperfine interactions can therefore be observed best in solid state spectra which will be discussed further in the next section.

### 1.1.3. Anisotropy in $g$ and $A$

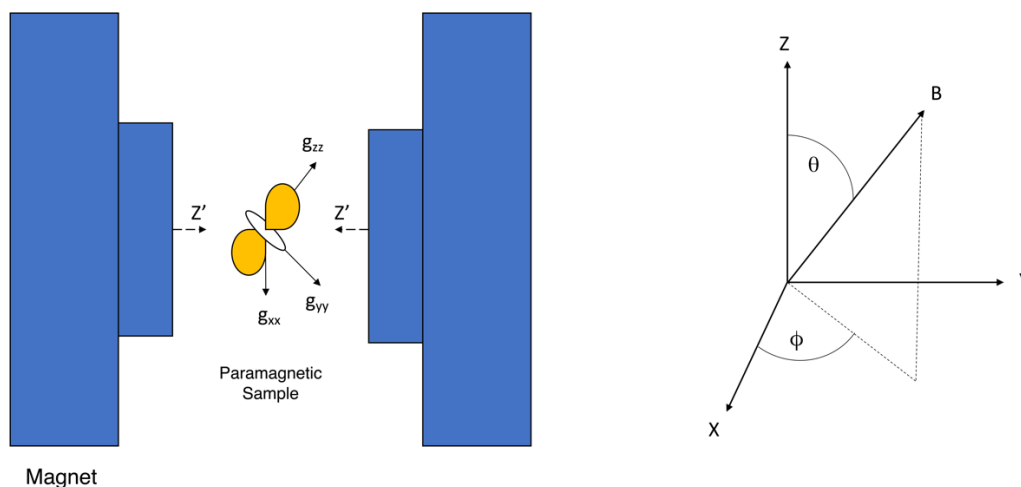


**Figure 1.1.3.1.** (Left) Diagram of a paramagnetic sample in a magnetic field (axis  $Z'$ ) and principal  $g$  axes ( $x,y,z$ ). (Right) Orientation of external magnetic field with orthogonal  $g$  tensor axes ( $x,y,z$ ) with cartesian coordinates and angles  $\theta$  and  $\phi$ .

EPR spectra of paramagnetic centers can be studied in the solid phase as single crystals, solid powders, or frozen solutions. This section will discuss in more detail the latter two cases where the sample contains a paramagnetic center randomly oriented with respect to the applied magnetic field as a solid powder or frozen solution, resulting in a powder spectrum. The information attained from a powder spectrum includes the *anisotropic*  $g$  and  $A$  tensors, containing additional information about the symmetry, bonding, structure, and electronic configuration of the paramagnetic system.

If a paramagnetic system is anisotropic and placed into a magnetic field, it may take up to nine numbers ( $3 \times 3$  array known as a tensor) to fully characterize it. The  $g$ -values may also show significant deviation from that of a free electron ( $g_e = 2.0023$ ). The source of this deviation is



primarily due to the interaction of the unpaired electron spin with the magnetic field and is orientationally dependent. The localization of the unpaired electron within a particular orbital introduces orbital angular momentum, and so spin-orbit coupling is the source of this anisotropy in  $g$ . A  $g$  tensor is needed to fully describe anisotropic interactions. This tensor can be described by principal axes rotating in cartesian space (specified by the angles  $\theta$  and  $\phi$ ) (**Figure 1.1.3.1**).

For resonance absorption to occur, one must satisfy the previous resonance equation:

$$\Delta E = h\nu = g(\theta, \phi) \beta \mathbf{B}$$

The effective anisotropic  $g$  value for any orientation  $(\theta, \phi)$ , with respect to the magnetic field  $\mathbf{B}$ , can be found from the following equation:

$$g(\theta, \phi) = (g_{xx}^2 \cos^2 \phi \sin^2 \theta + g_{yy}^2 \sin^2 \phi \sin^2 \theta + g_{zz}^2 \cos^2 \theta)^{1/2}$$

EPR spectra calculated according to this equation exhibit the following limiting cases (**Figure 1.1.3.2**). When  $g_x = g_y = g_z$ , the magnetic moment is independent of orientation, it is *isotropic* and a symmetric EPR signal will be observed. When  $g_x = g_y < g_z$  or  $g_x = g_y > g_z$ , the spectrum is said to be *axial*. In *axial* spectra the two common  $g$  values are often referred to as  $g_{\perp}$  and  $g_{\parallel}$ .

Finally, when  $g_x \neq g_y \neq g_z$  the spectrum is said to be *rhombic*.

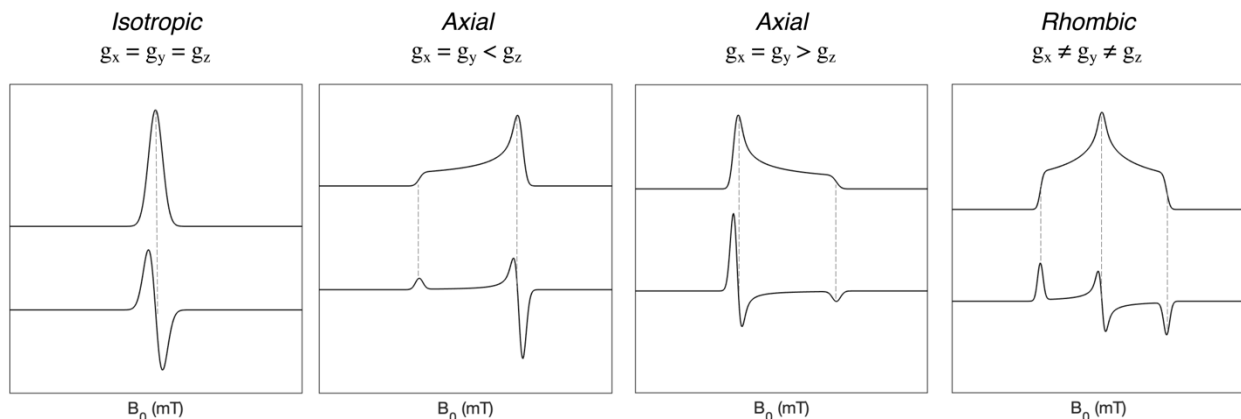


**Figure 1.1.3.2.** (Top) Spectral envelopes for a  $S = \frac{1}{2}$  paramagnetic center and the corresponding first derivative EPR spectrum (Bottom).

In the same way that the value of  $\mathbf{g}$  is most completely described as a tensor, the hyperfine interaction as well has anisotropy and must be fully described through the  $\mathbf{A}$  tensor. The anisotropic behavior of the hyperfine interaction will be described in more detail in **Section 1.1.6**.

#### 1.1.4. The Quadrupole Interaction

Many nuclei have  $I > \frac{1}{2}$ , which means a non-spherical distribution of charge is present at the nucleus and this generates a quadrupole moment ( $\mathbf{P}$ ). The quadrupole moment interacts with the electric field gradient at the nucleus. Therefore, analysis of the nuclear-quadrupole parameter ( $\mathbf{P}$ ) provides valuable information on the nature of the atomic orbitals at the nucleus and the electron distributions. The principal values of the nuclear quadrupole tensor ( $\mathbf{P}$ ) are:

$$P_{xx} = [-(e^2qQ/(4h))](1-\eta)$$

$$P_{yy} = [-(e^2qQ/(4h))](1+\eta)$$

$$P_{zz} = e^2qQ/(2h)$$

Where  $\eta$  is the asymmetry parameter and  $Q$  is the electric quadrupole moment. Since the quadrupole tensor  $\mathbf{P}$  is traceless, it can be determined by the two parameters  $\eta$  and  $Q$ . The quadrupole coupling does not contribute to the frequencies of EPR transitions, it creates only small second order perturbations in the energy levels that are often unnoticeable in EPR spectra (**Figure 1.1.4**). Quadrupole effects to the first order are readily observed in hyperfine spectra, such as ENDOR, which will be described in more detail in **Section 1.1.6**.

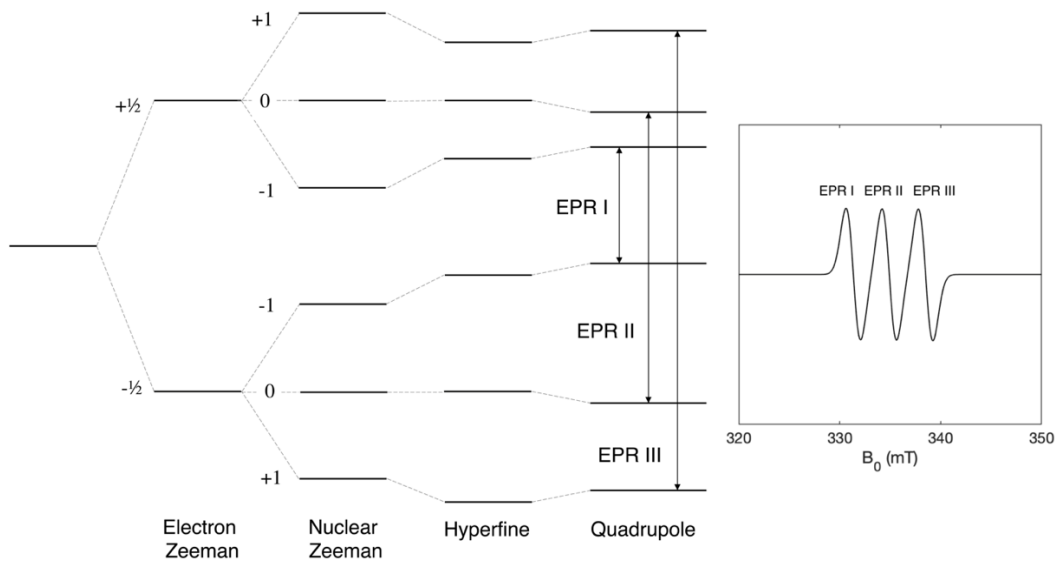


**Figure 1.1.4.** (Left) Energy level diagram with a fixed magnetic field for a  $S = 1/2$  and  $I = 1$  system. Labeled are the electron Zeeman interaction, nuclear Zeeman interaction, hyperfine, and quadrupole perturbation. (Right) EPR spectrum showing the three transitions due to the hyperfine and quadrupole interactions on the unpaired electron.<sup>1</sup>

### 1.1.5. Zero-Field Splitting

Many paramagnetic systems have  $S > 1/2$ , where the unpaired electrons have dipole-dipole interactions analogous to the hyperfine interaction. The dipole-dipole interaction is anisotropic and depends on the distance between the electrons and their relative orientation to each other. The dipole-dipole interaction is described by the dipolar tensor  $\mathbf{D}$ . In these systems the electron energy levels will not be degenerate in the absence of a magnetic field and the energy level splitting is known as zero-field splitting (ZFS). Diagonalizing the traceless tensor  $\mathbf{D}$  results in the parameters  $D$  and  $E$  which characterize the dipole interaction:

$$D = 3/2D_{zz}; \quad E = 1/2(D_{xx} - D_{yy})$$

Two unpaired electrons with total spin  $S = 1$ , will be split by this dipole-dipole interaction into three energy levels corresponding to the  $m_s$  value  $-1, 0,$  and  $+1$ . This example illustrated in **Figure 1.1.5.1.**, which shows the effect of weak zero-field splitting, leading to EPR transitions at different energies than would otherwise be expected for a free electron.

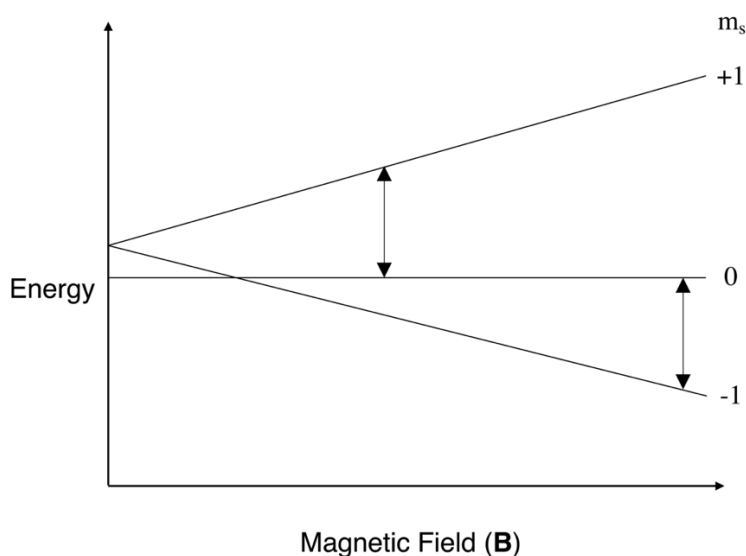


**Figure 1.1.5.1.** Effect of weak zero-field splitting on the EPR spectrum of a triplet state,  $S = 1$ . The EPR transitions,  $\Delta m_s \pm 1$ , are labeled with arrows.<sup>4</sup>

In the case of transition metal ions, zero-field splitting is dominated by spin-orbit coupling rather than dipole-dipole interactions. Zero-field splitting in these paramagnetic systems can be much stronger than any other magnetic interactions, including the electron Zeeman interaction. This shifts any observable transitions outside the range of a standard X-band frequency. High frequency/high field EPR instruments are needed to observe transitions between energy levels in these complex paramagnetic systems, though in many cases the energy splitting is still too large. For paramagnetic systems with an integer spin ( $S = 1, 2 \dots$ ), transitions between energy levels (called non-Kramer's doublets) are often difficult to observe. Parallel

mode is often used to study integer spin systems, in which the microwave irradiation is parallel to the external magnetic field. Half-integer spin systems ( $S = 3/2, 5/2\dots$ ) are often easier to observe in a standard perpendicular EPR experiment. Though if the zero-field splitting is too large, only transitions within each energy level doublet (called Kramer's doublets) is possible (Figure 1.1.5.2.). These transitions can be treated as effective  $S' = 1/2$  systems, whose anisotropy depends on the ratio between the zero field splitting parameters  $E/D$ .

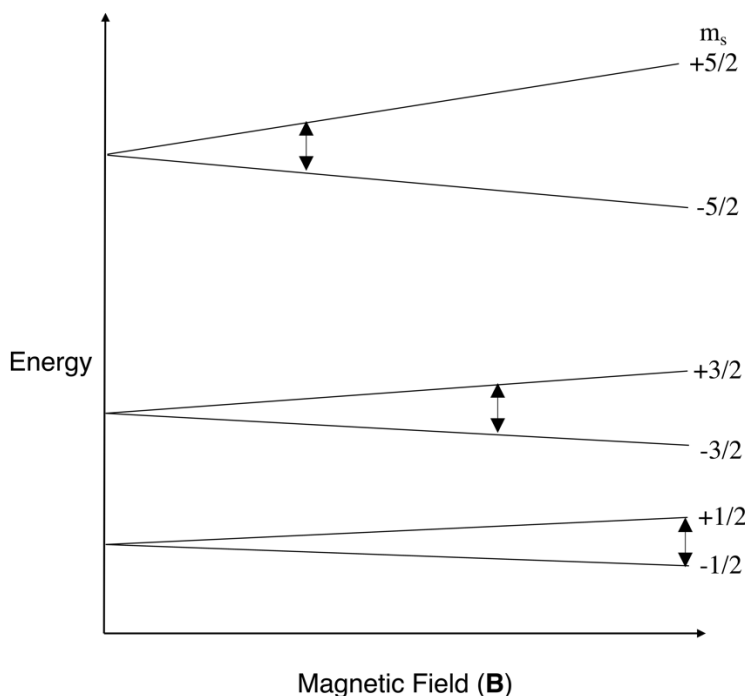


**Figure 1.1.5.2.** Effect of strong zero-field splitting on the EPR spectrum of a  $S = 5/2$  system.

The EPR transitions,  $\Delta m_s \pm 1$ , are labeled with arrows.<sup>4</sup>

### 1.1.6. The Full Spin Hamiltonian

The shape and intensity of the experimental EPR spectrum for a paramagnetic system can be fully interpreted by constructing a “spin Hamiltonian”. This is done by adding the operators describing the magnetic interactions involving its unpaired electrons. Combining the interactions

introduced in the preceding sections that describe the electron and nuclear spins with each other and their environment, the following complete spin Hamiltonian can be constructed:

$$\hat{H} = g_e \beta S + SDS + SAI$$

The first term takes into account the electron Zeeman interaction which is dependent on the magnetic field, and the following two terms account for the zero-field splitting and nuclear hyperfine interactions which are both independent of the applied magnetic field. Depending on the electron and nuclear spin quantum numbers and the magnitude of their interactions, some terms may be neglected or further added in to describe the paramagnetic system.

### 1.1.7. Electron nuclear double resonance (ENDOR) Spectroscopy

EPR Spectra provide useful information about paramagnetic systems through the observable  $g$ -values, but detailed information about the electron-nuclear hyperfine and quadrupole interactions is often left unresolved because of how small the energy values are for these interactions. Pulsed EPR techniques like Electron Spin Echo Envelope Modulation (ESEEM) and Electron Nuclear Double Resonance (ENDOR) can be used to study these hyperfine interactions that are otherwise too small to be resolved within the EPR linewidth. This section will focus specifically on ENDOR and how it can be used to gain structural information about paramagnetic systems.

ENDOR observes nuclear spin flip transitions within an electron spin manifold. The resonance lines are narrower in ENDOR spectroscopy, on the order of a thousand or more in enhanced resolution. In an ENDOR experiment, the magnetic field is set on a particular line in the EPR spectrum, such as in the example with a  $S = \frac{1}{2}$ ,  $I = \frac{1}{2}$  (**Figure 1.1.2.**). The EPR transition is partially or fully saturated, then the radio frequency is swept. When the

radiofrequency matches a NMR transition, the nuclear spin flips. The flipping of the nuclear spin causes the spin populations to no longer be equal and this restores EPR absorption.

In an ENDOR experiment, there are three limiting cases depending on the strength of the hyperfine relative to the Larmor frequency,  $\nu_N$ :

$$\begin{aligned} \nu_N > A/2 & \quad \nu_{\text{ENDOR}} = \nu_N \pm A/2 \\ \nu_N = A/2 & \quad \nu_{\text{ENDOR}} = \nu_N \pm A/2 = 2\nu_N \\ \nu_N < A/2 & \quad \nu_{\text{ENDOR}} = A/2 \pm \nu_N \end{aligned}$$

The result of these three limiting cases can be seen in **Figure 1.1.6.1**. In the case of weak hyperfine, the ENDOR spectrum will be observed centered at the Larmor frequency  $\nu_N$ , with splitting equal to the hyperfine value  $A$ . On the opposite extreme, when the hyperfine interaction is strong it will be centered at  $A/2$ , with a splitting of  $2\nu_N$ .

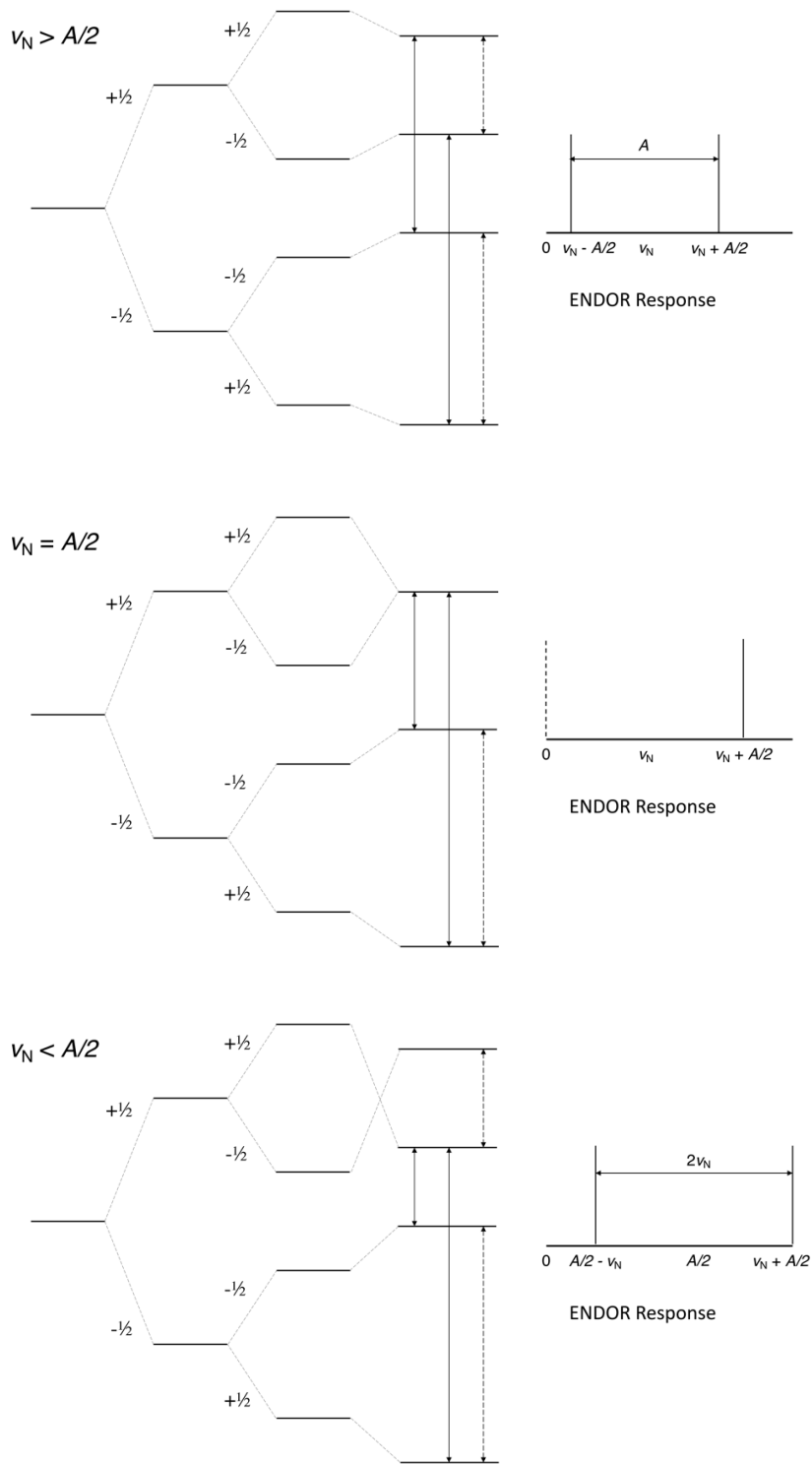


**Figure 1.1.7.1.** (Left) Energy level diagram with a fixed magnetic field for a  $S = 1/2$  and  $I = 1/2$  system. Solid arrows show EPR transitions and dotted arrows show NMR transitions. (Right) ENDOR response stick spectrum.<sup>1</sup>



In the case for when  $I \geq 1$ , the quadrupole interaction must also be considered. Each ENDOR peak is further split by the quadrupole moment into  $2I$  lines dictated by the following equation:

$$v_{\pm}(m_I) = \left| v_N \pm \frac{A}{2} \pm \frac{3P(2m_I-1)}{2} \right|$$

The hyperfine coupling observed may again be weak or strong, though for each case the observed quadrupole splitting is the same,  $3P$  (Figure 1.1.7.2).

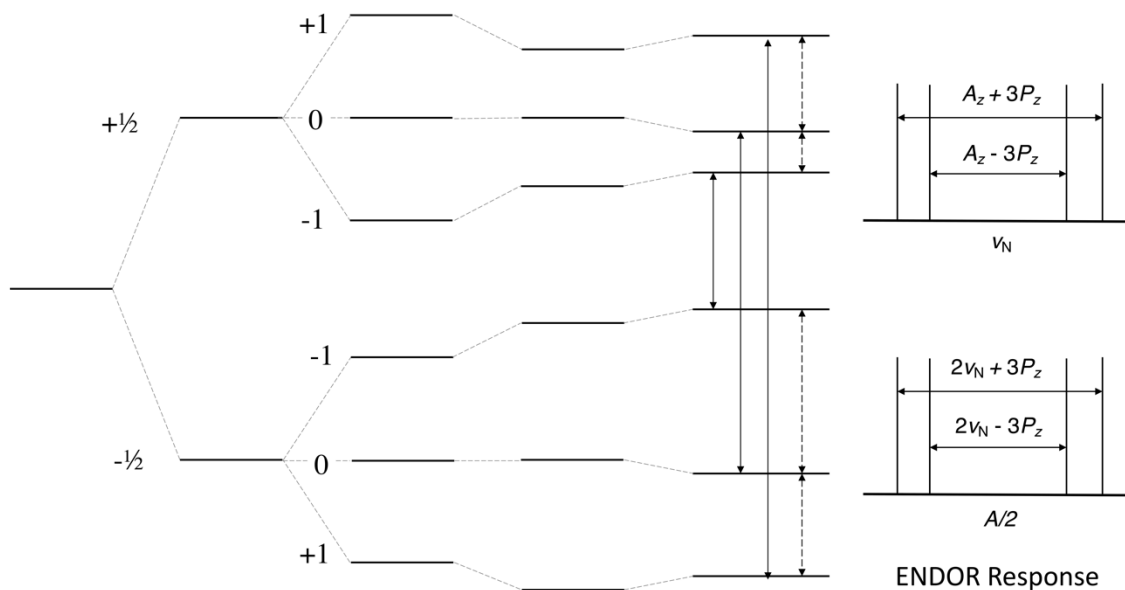
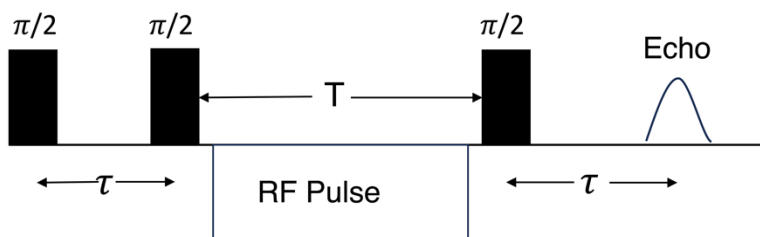


**Figure 1.1.7.2.** (Left) Energy level diagram with a fixed magnetic field for a  $S = 1/2$  and  $I = 1$  system. Solid arrows show EPR transitions and dotted arrows show NMR transitions. (Right) ENDOR response stick spectrum for weak (Top) or strong (bottom) hyperfine interaction.<sup>1</sup>

ENDOR spectra may be collected with continuous wave (CW) EPR instrumentation, by holding the magnetic field static and sweeping an applied radiofrequency for NMR transitions. Pulsed ENDOR techniques may also be used which can give better-resolved ENDOR line shapes

and resolve weaker hyperfine couplings. There are two fundamental pulsed ENDOR techniques, Mims and Davies ENDOR.<sup>5,6</sup> Mims ENDOR is based on a three-pulse stimulated electron spin echo:  $\pi/2 - \tau - \pi/2 - T - \pi/2 - \tau - \text{echo}$  (**Figure 1.1.7.3**). A radiofrequency pulse is applied during time T. Mims ENDOR is most useful for small hyperfine couplings less than 4 MHz. For larger hyperfine couplings, Davies ENDOR is more useful having the sequence,  $\pi - T - \pi/2 - \tau - \pi - \tau - \text{echo}$ . Again, the radiofrequency pulse is applied during time T.

### Mims ENDOR



### Davies ENDOR

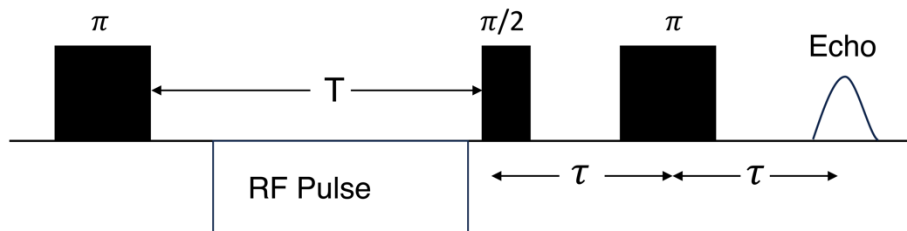


**Figure 1.1.7.3.** Schematic representation of Mims and Davies ENDOR.<sup>6</sup>

## 1.2. Introduction to Mössbauer Spectroscopy

The Mössbauer Effect has been observed for 43 elements and has been used to study the electronic environment by probing the magnetism, electronic relaxation, chemical bonding, or redox properties of these nuclei. The most utilized Mössbauer isotope is  $^{57}\text{Fe}$ , which has allowed Mössbauer spectroscopy to play an important role in characterizing iron-containing compounds in inorganic chemistry and metallobiochemistry.<sup>7</sup> This section will outline the basic principles for  $^{57}\text{Fe}$  Mössbauer Spectroscopy, a spectroscopic technique utilized in later chapters.

### 1.2.1. The Mössbauer Effect

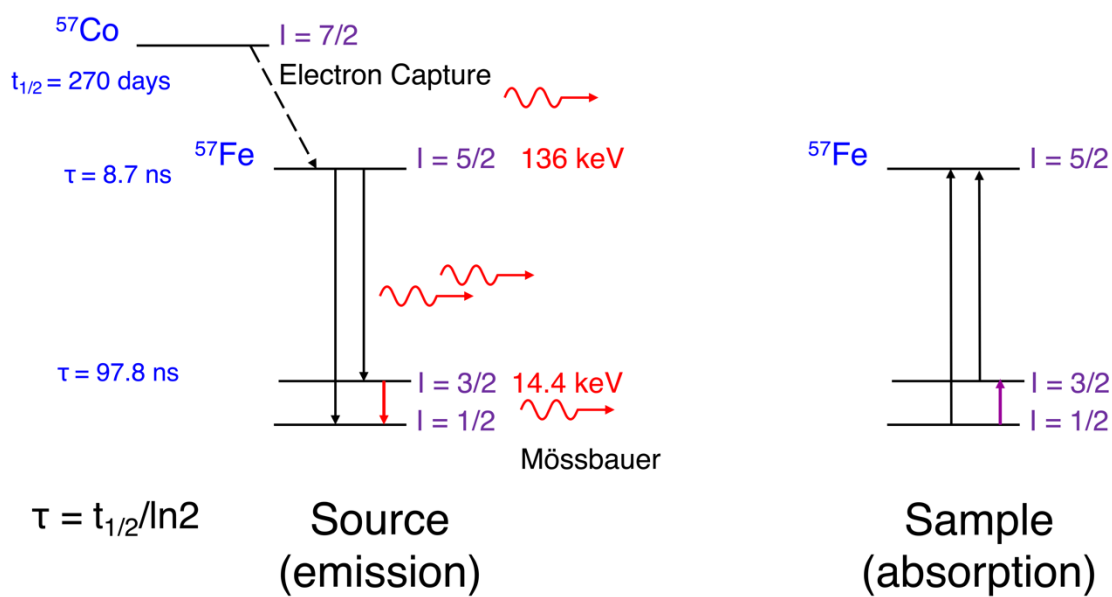


**Figure 1.2.1.** Decay scheme of  $^{57}\text{Co}$  and emission of Mössbauer  $\gamma$ -radiation. Sample containing  $^{57}\text{Fe}$  undergoes resonant absorption.

Mössbauer spectroscopy is based on recoilless emission and resonant absorption of  $\gamma$ -radiation by atomic nuclei. For nuclear  $\gamma$ -resonance absorption to occur, the  $\gamma$ -radiation must be emitted by nuclei of the same isotope as the absorber. In the case of  $^{57}\text{Fe}$  Mössbauer

spectroscopy,  $^{57}\text{Co}$  is the  $\gamma$ -ray source.  $^{57}\text{Co}$  has a half-life ( $t_{1/2}$ ) of 270 days and decays by K-capture, yielding  $^{57}\text{Fe}$  in a 136 keV excited state. Within 10 ns, the 136 keV state of  $^{57}\text{Fe}$  undergoes a transition to the ground state either directly by the emission of a 136 keV  $\gamma$ -photon (15%), or via the 14.4 keV Mössbauer excited state by the emission of a 122 keV photon first (85%) (**Figure 1.2.1**).<sup>8</sup> This  $^{57}\text{Co}$  Mössbauer source is prepared by diffusing the radioactive isotope into a matrix of nonmagnetic metal with cubic crystal lattice, typically rhodium metal. It is essential that the solid matrix impose neither a magnetic moment nor an electric field gradient to the source nuclei. In addition to using low temperatures, the solid metal matrix increases the probability that the  $\gamma$ -radiation will be emitted *recoilless*. The  $\gamma$ -photon that is emitted without recoil will have the correct energy to be absorbed by a  $^{57}\text{Fe}$  nucleus, whereby a transition to an excited state takes place. This phenomenon is known as nuclear resonance absorption, or the Mössbauer effect.<sup>9, 10</sup>

### 1.2.2. The Mössbauer Transmission Spectrum

In a Mössbauer experiment, the radioactive source is periodically moved with controlled velocities  $+v$  toward and away  $-v$  away from the absorber (**Figure 1.2.2**). The forward and backward motion modulates the energy of the  $\gamma$ -photons arriving at the absorber because of the Doppler effect:

$$E_{\gamma} = E_0(1+v/c)$$

The transmitted  $\gamma$ -rays are detected and recorded as a function of the Doppler velocity, which yields a Mössbauer spectrum. For a standard  $^{57}\text{Fe}$  experiment, the Doppler velocity is given in  $\text{mm s}^{-1}$  with  $1 \text{ mm s}^{-1} = 4.8 \times 10^{-8} \text{ eV}$ .

A source moving with velocity  $v$  will contain an unsplit emission line with a Lorentzian line shape and natural line width  $\Gamma$ . The number of recoil-free emitted  $\gamma$ -rays with energy  $E_\gamma$  in the range  $E$  to  $E+dE$  is given by:

$$N(E, v) = f_s N_0 \frac{\Gamma(2\pi)}{\left[ E - E_0(1 + \frac{v}{c}) \right]^2 + (\Gamma/2)^2}$$

Here the total number of  $\gamma$ -quanta emitted by the source per unit time traveling toward the detector is  $N_0$  and  $f_s$  is the recoil-free fraction.  $E_0$  is the mean energy of the nuclear transition, and  $E_0(1+v/c)$  is the Doppler-shifted center of the emission line. For the absorber, we assume the mean energy  $E_0$  between nuclear excited and ground states are the same as the source, but with an additional shift  $\Delta E$  due to the chemical environment. The absorption line would be expected to have the same Lorentzian line shape as the emission line, assuming the same full-width at half maximum  $\Gamma$ . The absorption line would have the cross section  $\sigma(E)$  given by:

$$\sigma(E) = \sigma_0 \frac{(\Gamma/2)^2}{(E - E_0 - \Delta E)^2 + (\Gamma/2)^2}$$

In the case of  $^{57}\text{Fe}$  the  $\sigma(E)$  is  $2.56 \times 10^{-18} \text{ cm}^2$ . For an actual experimental Mössbauer spectrum of a thin single-line absorber, with Lorentzian line width, the full-width at half maximum is twice that natural line width of the separate emission and absorption lines:  $\Gamma_{\text{exp}} = 2\Gamma$  (**Figure 1.2.2.**).

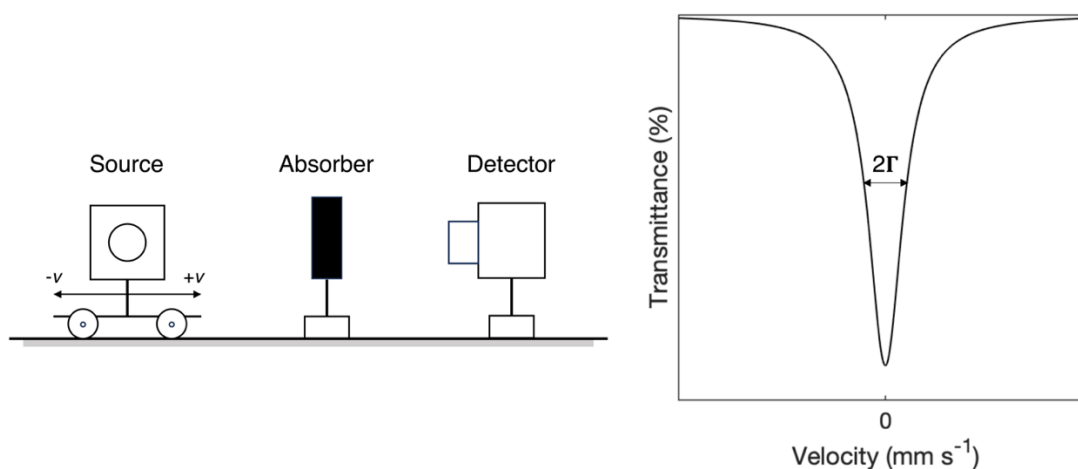


**Figure 1.2.2.** Schematic illustration of a Mössbauer experiment. (Left) Experimental set up of source and absorber for doppler shifted  $\gamma$ -radiation. (Right) Mössbauer transmission spectrum.<sup>11</sup>

### 1.2.3. Mössbauer Hyperfine Interactions

<sup>57</sup>Fe nuclei are exposed to electric and magnetic fields created by the electrons on the absorber atom or by other atoms in the nearby chemical environment. These fields interact with the magnetic dipole moment of the <sup>57</sup>Fe nucleus and perturb its nuclear energy states. This nuclear hyperfine interaction may shift nuclear energy levels such as in the electric monopole interaction, or split degenerate energy levels as seen in the electric quadrupole interaction and magnetic dipole interaction.<sup>11-13</sup> Most of the valuable information regarding a chemical system can be extracted from these hyperfine interactions. The following is a brief overview of the three main hyperfine interactions that perturb the Mössbauer nuclei's energy levels.

### 1.2.3.1. The Mössbauer Isomer shift ( $\delta$ )

The electric monopole interaction between a nucleus and its environment is a product of the nuclear charge distribution  $ZeR^2$  and the electronic charge density  $e|\psi(0)|^2$  at the nucleus. Nuclei of the same mass and charge but with different nuclear states will have different charge distributions ( $ZeR_g^2 \neq ZeR_e^2$ ). Therefore, the energies of a Mössbauer nuclei found in different chemical environments, in the ground state and excited state will be shifted by different energies relative to those of a bare nucleus. This occurrence is responsible for the Mössbauer *isomer shift* ( $\delta$ ).<sup>14</sup> Provided that the electron densities  $|\psi(0)|_s^2$  and  $|\psi(0)|_A^2$  at the Mössbauer nuclei in the source and the absorber material are different because of different chemical compositions, the transition energies  $E_{\text{source}}$  and  $E_{\text{absorber}}$  will also be different. For this reason,  $\gamma$ -resonant absorption in the Mössbauer experiment does not appear at a Doppler velocity of zero but is instead shifted by an amount ( $\delta$ ), the *isomer shift* (**Figure 1.2.3.1.**). For a comparison of experimental Mössbauer isomer shifts, the values must be referenced to a common standard. For  $^{57}\text{Fe}$  Mössbauer spectroscopy, the spectrometer is usually calibrated by using the known absorption spectrum of metallic iron ( $\alpha$ -iron).

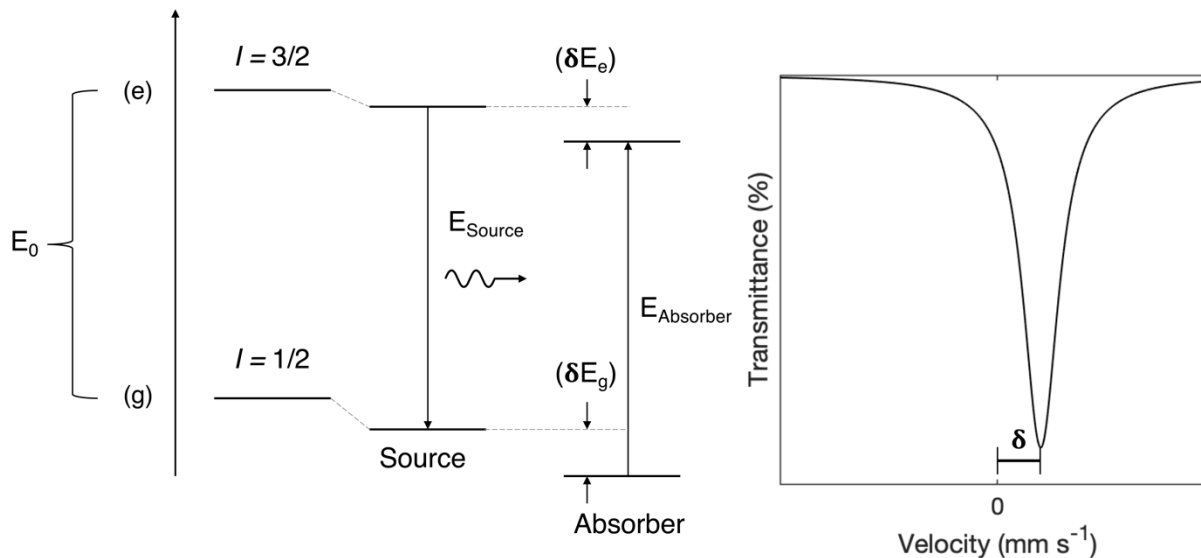


**Figure 1.2.3.1.** (Left) Diagram showing the electric monopole interaction between the nuclear charge and the electron density, shifting the energy of the nuclear states. (Right) The resulting Mössbauer transmission spectrum with the *isomer shift* labeled.<sup>11</sup>

The electron density  $|\psi(0)|^2$  at the nucleus primarily originates from the ability of s-electrons to penetrate the nucleus. The core-shell 1s and 2s electrons have the largest *direct* effect to the s-electron density found at the nucleus. This s-electron density will increase or decrease based on the amount of shielding of nuclear potential by other electrons. An additional *indirect* effect to the s-electron density experienced at the nucleus, is by the participation of valence s-orbitals in the formation of molecular orbitals (MOs). The isomer shift ( $\delta$ ) can therefore an excellent probe into oxidation state, spin state, and chemical bonds formed by the Mössbauer nuclei. A chemical environment that increases s-electron density at the nucleus leads to lower isomer shifts, whereas decreasing the s-electron density has the opposite effect leading to higher isomer shifts. Therefore, high oxidation states tend to have low isomer shifts due to decreased shielding of core s-electrons. Covalent (*soft*) ligands give lower isomer shifts in



comparison to ionic (*hard*) ligands because of better orbital overlap with valence s-electrons. Ligands that are excellent  $\pi$ -acceptors will as well lead to lower isomer shifts as they shift electron density away from the nuclei and onto the ligand, decreasing shielding of core s-electrons. Finally, the length of the iron-ligand bond that forms is also a strong determinant of the *isomer shift* observed. Compounds that exhibit strong short covalent bonds lead to contraction of the orbitals on the Mössbauer nuclei. For this reason, ligands with excellent  $\sigma$ -donor and  $\pi$ -acceptor properties will exhibit low isomer shifts.

### 1.2.3.2. Quadrupolar Splitting ( $\Delta E_Q$ )

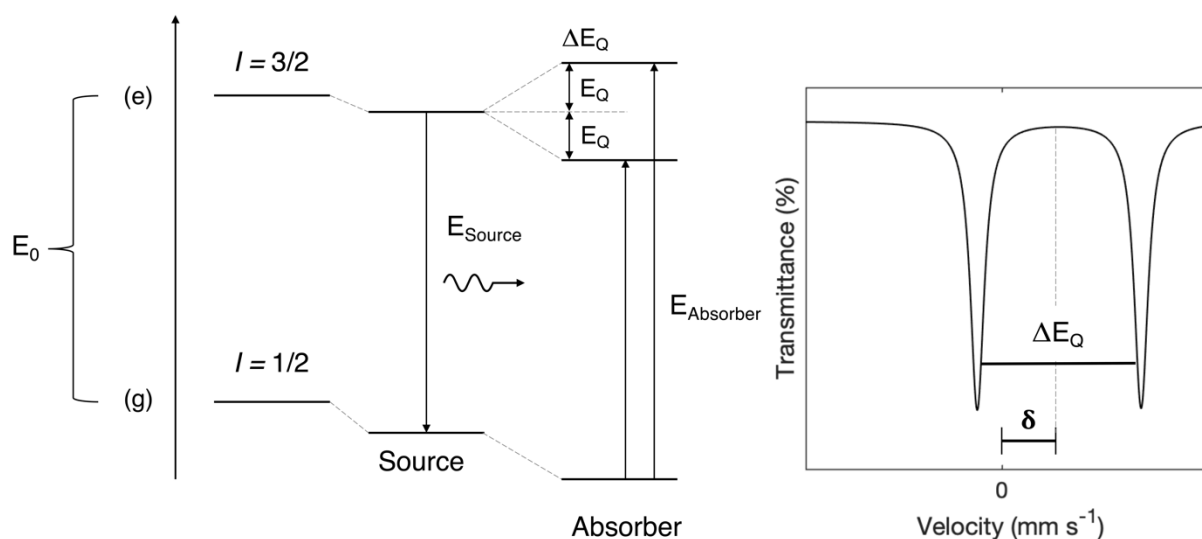


**Figure 1.2.3.2.** (Left) Diagram showing the quadrupole splitting of the excited state of  $^{57}\text{Fe}$  with  $I = 3/2$  into two degenerate sublevels with energy separation  $\Delta E_Q = 2E_Q$ . (Right) The resulting Mössbauer transmission spectrum with *quadrupole splitting* and *isomer shift* labeled.<sup>11</sup>

As described previously in **Section 1.1.4.**, an  $^{57}\text{Fe}$  nucleus will be subject to a quadrupole moment in the excited state. The electric quadrupole interaction causes a splitting of the  $(2I + 1)$

magnetic substates without shifting the mean energy of the nuclear spin manifold. For  $^{57}\text{Fe}$ , the ground state remains unsplit because of the lack of quadrupole moment for  $I = 1/2$ , though the excited state with  $I = 3/2$  splits into two doubly degenerate substates (**Figure 1.2.3.2.**). The energy difference  $\Delta E_Q$  between the two substates is given by:

$$\Delta E_Q = E_Q(\pm 3/2) - E_Q(\pm 1/2) = eQV_{zz}/2$$

The parameter  $\Delta E_Q$  provides information about bond properties and local symmetry at the iron site. Since the quadrupole interaction does not alter the mean energy of the nuclear ground and excited states, the isomer shift ( $\delta$ ) and quadrupole splitting ( $\Delta E_Q$ ) can be determined directly from the spectrum.

Valence electrons belonging to the Mössbauer nuclei make the strongest contribution to the electric field gradient and therefore the observed quadrupole splitting. Large quadrupole splitting results when the electric field gradient deviates from spherical symmetry, which is determined by the molecular orbitals formed between the Mössbauer atom and the ligands. An example is the difference seen in quadrupole splitting for high-spin and low-spin Fe(II). Assuming an octahedral ligand environment, low-spin Fe(II) would have a near spherical electric field gradient with evenly distributed valence electrons, leading to small quadrupole splitting. Whereas high spin Fe(II) contains asymmetrically distributed valence electrons, giving the often observed large quadrupole splitting. The quadrupole splitting value is thus very informative to the ligand coordination environment for the Mössbauer nuclei.

### 1.2.3.3. The Magnetic Dipole Moment

As previously described in **Section 1.1.2.**, a nucleus with spin quantum number  $I > 0$  will interact with a magnetic field through its magnetic dipole moment  $\mu_N$ . The nuclear Zeeman interaction will split the nuclear state with spin quantum number  $I$  into  $2I+1$  equally spaced

and nondegenerate substates. For  $^{57}\text{Fe}$ , the magnetic dipole interaction splits the excited state  $I = 3/2$  into four magnetic substates and the ground state  $I = 1/2$  into two substates (**Figure 1.2.3.3**). The allowed transitions are given by,  $\Delta I = 1$   $\Delta m_I = 0, \pm 1$  resulting in 6 allowed transitions. The magnetic hyperfine splitting allows the determination of the effective magnetic field acting on the nucleus, which can be a superposition of an applied magnetic field  $\mathbf{B}_{\text{ext}}$  and an internal field  $\mathbf{B}_{\text{int}}$  arising from a magnetic moment of the valence electrons. Magnetically split spectra are most frequently observed at low temperatures where relaxation is slow.

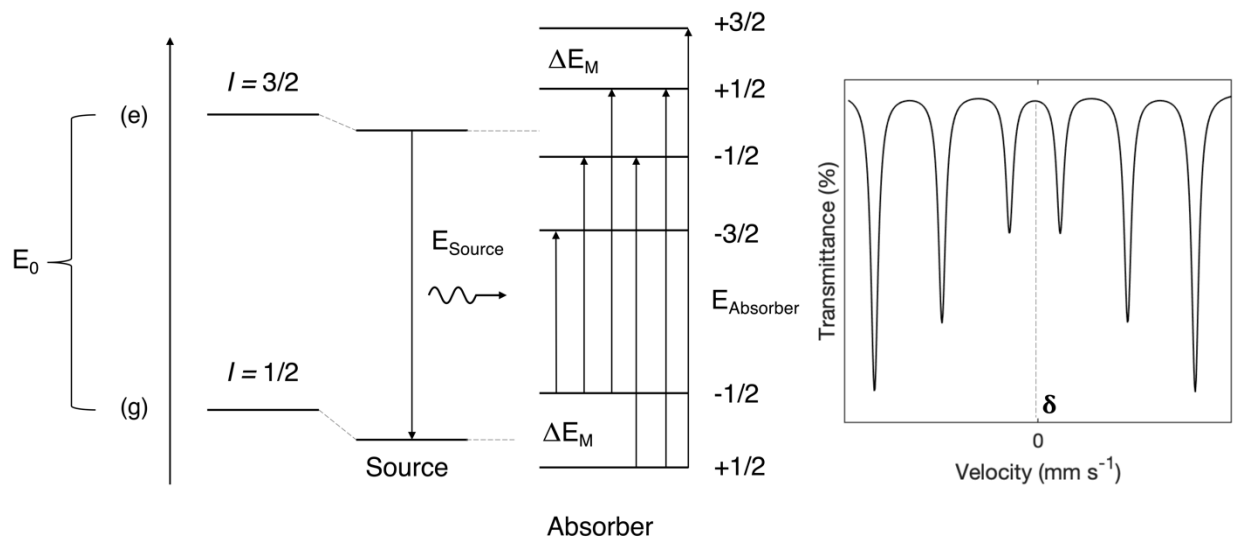


**Figure 1.2.3.3.** (Left) Magnetic dipole splitting in  $^{57}\text{Fe}$  and (Right) resulting Mössbauer transmission spectrum.<sup>11</sup>

#### 1.2.3.4. Combined Electric and Magnetic Hyperfine Interactions

Most frequently, a nuclear state is perturbed simultaneously by all three types of hyperfine interaction – electric monopole, electric quadrupole, and magnetic dipole.

$$\hat{H} = \delta E + \hat{H}_Q + \hat{H}_M$$

The monopole interaction  $\delta E$ , which yields the isomer shift, can be treated easily as it is additive to all transition energies. The Magnetic dipole interaction  $\hat{H}_M$  and electric quadrupole interaction  $\hat{H}_Q$  both depend on the magnetic quantum numbers of the nuclear spin. Often, they can be treated as a perturbation if one interaction of the two is much weaker than the other. However, if the interactions are of the same order of magnitude  $g_N \mu_N \mathbf{B} \approx eQV_{zz}/2$  the full nuclear Hamiltonian must be evaluated.

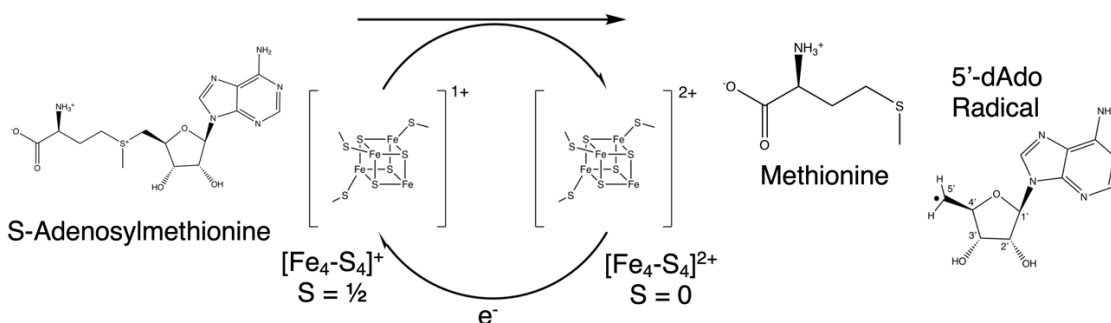
### 1.3. References

1. Que, L., *Physical Methods in Bioinorganic Chemistry*. University Science Books: Sausalito, California, 2000.
2. Weil, J. A. B., J.R., *Electron Paramagnetic Resonance: Elementary Theory and Practical Applications*. Wiley-Interscience: Hoboken, New Jersey, 2007; p 664.
3. Poole, C. P., *Electron Spin Resonance: A Comprehensive Treatise on Experimental Techniques*. Second Edition ed.; Dover Publications Inc.: Mineola, New York, 1982.
4. Bertrand, P., *Electron Paramagnetic Spectroscopy: Fundamentals*. Springer International Publishing: 2020.
5. Mims, W. B., Pulsed Endor Experiments. *Royal Society* **1965**, 283, 452-457.
6. Davies, E. R., A New Pulse ENDOR Technique. *Phys Lett* **1974**, 47A, 1-2.
7. Greenwood, N. N., Chemical and biological applications of Mossbauer spectroscopy. *Endeavour* **1968**, 27 (100), 33-7.
8. Kock, W. E., The Mossbauer Radiation. *Science* **1960**, 131 (3413), 1588-90.
9. Mossbauer, R. L., Recoilless Nuclear Resonance Absorption of Gamma Radiation: A new principle yields gamma lines of extreme narrowness for measurements of unprecedented accuracy. *Science* **1962**, 137 (3532), 731-8.
10. Dunlap, R. A., *The Mössbauer Effect*. Morgan & Claypool Publishers: San Rafael, CA, 2019.
11. Gutlich, P.; Bill, E.; Trautwein, A. X., Mossbauer Spectroscopy and Transition Metal Chemistry: Fundamentals and Applications. *Mossbauer Spectroscopy and Transition Metal Chemistry: Fundamentals and Applications* **2011**, 1-568.
12. Cohen, R. L., *Applications of Mössbauer Spectroscopy*. New York: Academic Press: 1976.
13. Greenwood, N. N.; Gibb, T. C., *Mössbauer Spectroscopy* London, Chapman and Hall: 1971; p 659.
14. Shenoy, G. K.; Wagner, F. E., *Mössbauer Isomer Shifts*. North-Holland Pub. Co.: New York, 1978.

## Chapter 2

### Radical S-adenosyl methionine (SAM) enzyme HydG and the Biosynthesis of the [FeFe]-hydrogenase H-cluster active site

#### 2.1. Introduction to Radical S-adenosyl methionine (SAM) enzymes



**Scheme 2.1.1.** General mechanism of Radical SAM enzymes to generate a 5'-dAdo radical.<sup>1</sup>

Radical SAM enzymes are metalloenzymes that utilize a unique [Fe<sub>4</sub>-S<sub>4</sub>]<sub>RS</sub> cluster and S-Adenosylmethionine (SAM) co-substrate to catalyze a variety of biochemical reactions.<sup>2</sup> Bioinformatics had initially identified 650 members of this Radical SAM family, but the number has since grown to include over 100,000 homologous enzymes.<sup>3,4</sup> To biochemically be considered part of the Radical SAM family, enzymes must contain a unique three-cysteine motif that binds the [Fe<sub>4</sub>-S<sub>4</sub>]<sub>RS</sub> cluster. This structure leaves the apical iron free to bind SAM in a bidentate manner. The [CX<sub>3</sub>CX<sub>2</sub>C] motif is associated with a single domain and is conserved in more than 90% of known Radical SAM proteins.<sup>4</sup> SAM as a co-substrate has long been known to be important in cellular methylation, transcription, translation, gene regulation, signal transduction, and the biosynthesis of essential metabolites.<sup>1,5</sup> But the more recent emergence of Radical SAM enzymes has revealed a large array of catalytic reactions from the formation of metallocofactors such as those found in [FeFe]-hydrogenase to organic cofactors such as biotin.

Radical SAM enzymes also have critical importance to human health. If dysfunctional, Radical SAM enzymes may lead to diseases such as amyotrophic lateral sclerosis (ALS), congenital heart disease, impaired cardiac and respiratory function, and diabetes mellitus.<sup>1</sup> A detailed mechanistic understanding of Radical SAM catalysis therefore underscores a wide range of research areas including the environment and human health.

It is widely accepted that the general mechanism for Radical SAMs begins with SAM binding to the apical Fe of the  $[\text{Fe}_4\text{-S}_4]_{\text{RS}}$  cluster, inner-sphere electron transfer from the reduced cluster to the sulfonium atom results in bond cleavage of a S-C bond (**Scheme 2.1.1**).<sup>6,7</sup> Depending on orientation of SAM to the  $[\text{Fe}_4\text{-S}_4]_{\text{RS}}$  cluster, orbital overlap into antibonding orbitals may lead to homolytic cleavage of S-C forming either catalytically active 5'-dAdo radical or the 3-amino-3-carboxypropyl radical. In the case of SAM-methylation, heterolytic bond cleavage of the S-C bond leads to methyl transfer from SAM to an available enzyme-based nucleophile.<sup>8</sup> Recently direct observation of the 5'-dAdo radical by EPR has come through two different approaches.<sup>9,10</sup> In one approach flash photolysis led to the cleavage of the S-C bond in the absence of substrate, generating an isolated 5'-dAdo radical.<sup>9</sup> In the second approach, an alternate substrate altered the thermodynamics such that the 5'-dAdo radical reached an equilibrium with the non-natural substrate.<sup>10</sup> In each case, the 5'-dAdo radical can be easily identified with its unique proton hyperfine pattern generated from the two hydrogens on the 5'-carbon and one from the 4'-carbon (**Scheme 2.1.1., Figure 2.1.1.**). In the natural catalytic cycle, the generated 5'-dAdo radical, a strong oxidant, will catalyze a variety of important transformations by hydrogen atom abstraction or in more rare instances substrate reduction.

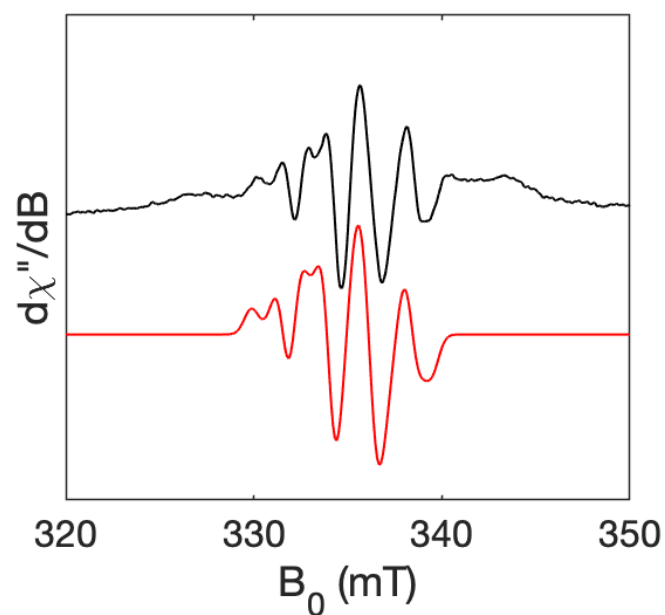
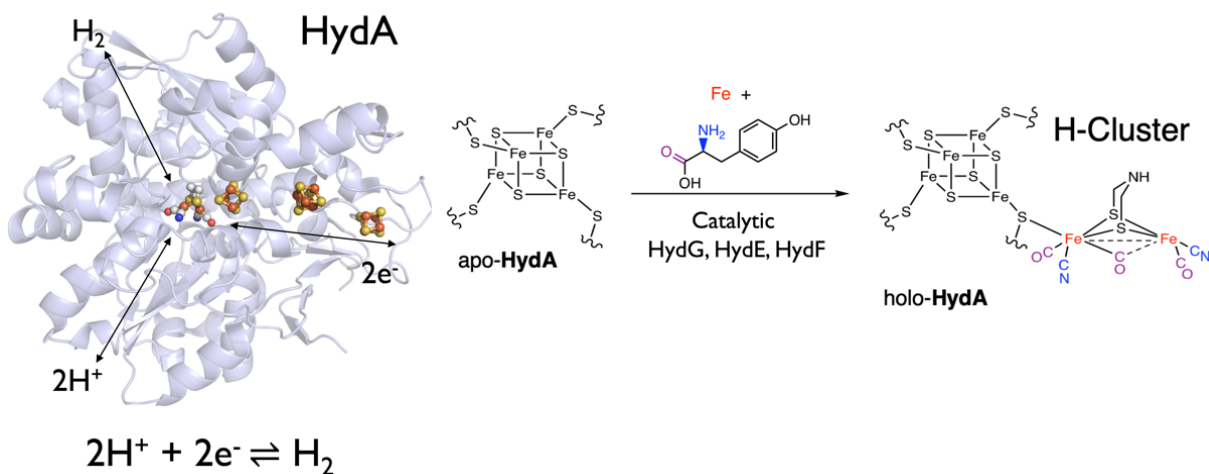


**Figure 2.1.1.** X-band (9.4 GHz) CW EPR spectrum of the 5'-dAdo• and total simulation (red trace). Simulation parameters  $g = [2.006 \ 2.004 \ 2.002]$ ,  $A(5'_{\text{Endo}}) [-25 \ -58 \ -107]$ ,  $A(5'_{\text{Exo}}) [-25 \ -58 \ -107]$ ,  $A(4'_{\text{Endo}}) [69 \ 62 \ 79]$ .<sup>10</sup>



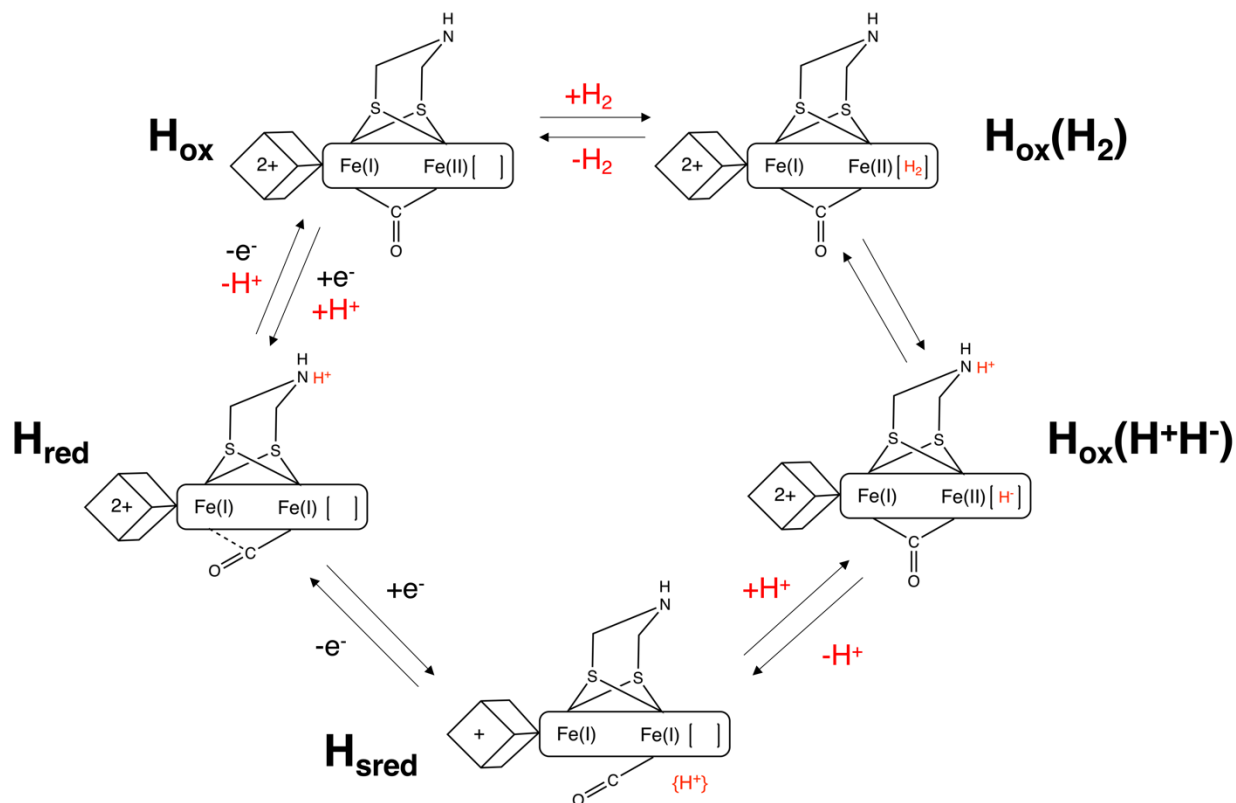
## 2.2 Introduction to [FeFe]-hydrogenase and the H-cluster



**Scheme 2.2.1.** Maturation of apo-HydA. pdb: 1HFE

[FeFe]-hydrogenases are the most active enzymes in the production of molecular hydrogen. Their reversible catalysis, consuming or producing hydrogen, fulfills the metabolic demands of diverse bacteria and many eukaryotes.<sup>11</sup> Their energetic efficiency and capacity to reduce protons to form  $\text{H}_2$  makes hydrogenases important research targets in the context of renewable energy.<sup>12, 13</sup> In efforts to replicate these catalysts, much attention has focused on their active sites. The active site of [FeFe]-hydrogenase, the H-cluster, contains a  $[\text{4Fe-4S}]_{\text{H}}$  with three cysteine-ligated Fe's and a fourth Fe linked by a cysteinyl bridge to the proximal Fe of a unique  $[\text{2Fe}]_{\text{H}}$  active site. This binuclear  $[\text{2Fe}]_{\text{H}}$  active site has two CO and two CN<sup>-</sup> terminal ligands, plus a bridging azadithiolate (adt), and a bridge from an additional CO (**Scheme 2.2.1**).<sup>14, 15</sup> Despite being phylogenetically unrelated, the active sites across all classes of hydrogenases [FeFe], [NiFe] and the [Fe]-only also feature thiolate and CO ligation.<sup>11</sup> This distinctive environment enables catalysis by stabilizing low spin states and the formation of hydride and dihydrogen complexes.<sup>16</sup>

The three CO and CN<sup>-</sup> ligands bound on the H-cluster can be seen by FTIR in a region free of other protein bands. Reduced states for the H-cluster provide stronger back-bonding to the CO ligands, leading to FTIR bond stretches at lower frequency. Signals from CN<sup>-</sup> and CO can be used to monitor the appearance and disappearance of the various H-cluster oxidation states.<sup>17</sup> The H-cluster when poised in paramagnetic oxidation states will each give characteristic EPR signals. The H<sub>ox</sub> state, found in all known [FeFe] hydrogenases, is a mixed valent binuclear subcluster ([4Fe-4S]<sup>2+</sup>[Fe(I)Fe(II)]). When CO inhibits the H<sub>ox</sub> state, the H<sub>ox</sub>-CO state is produced with the same electronic structure but different EPR and FTIR spectra. Reducing the H<sub>ox</sub> state results in the H<sub>red</sub> state, ([4Fe-4S]<sup>2+</sup>[Fe(I)Fe(I)]), which is EPR silent. [FeFe]-hydrogenase from *Chlamydomonas reinhardtii* can be even further reduced to ([4Fe-4S]<sup>+</sup>[Fe(I)Fe(I)]), in which the additional electron is stored in the cubane subcluster. The EPR spectrum for this “super-reduced”, H<sub>sred</sub>, state is typical for a [4Fe-4S] cluster.<sup>18,19</sup> Collectively these H-cluster oxidation states establish the possible states that would exist during enzymatic turnover (**Scheme 2.2.2**).



**Scheme 2.2.2.** Potential mechanism of [FeFe]-hydrogenase in *Chlamydomonas reinhardtii*.

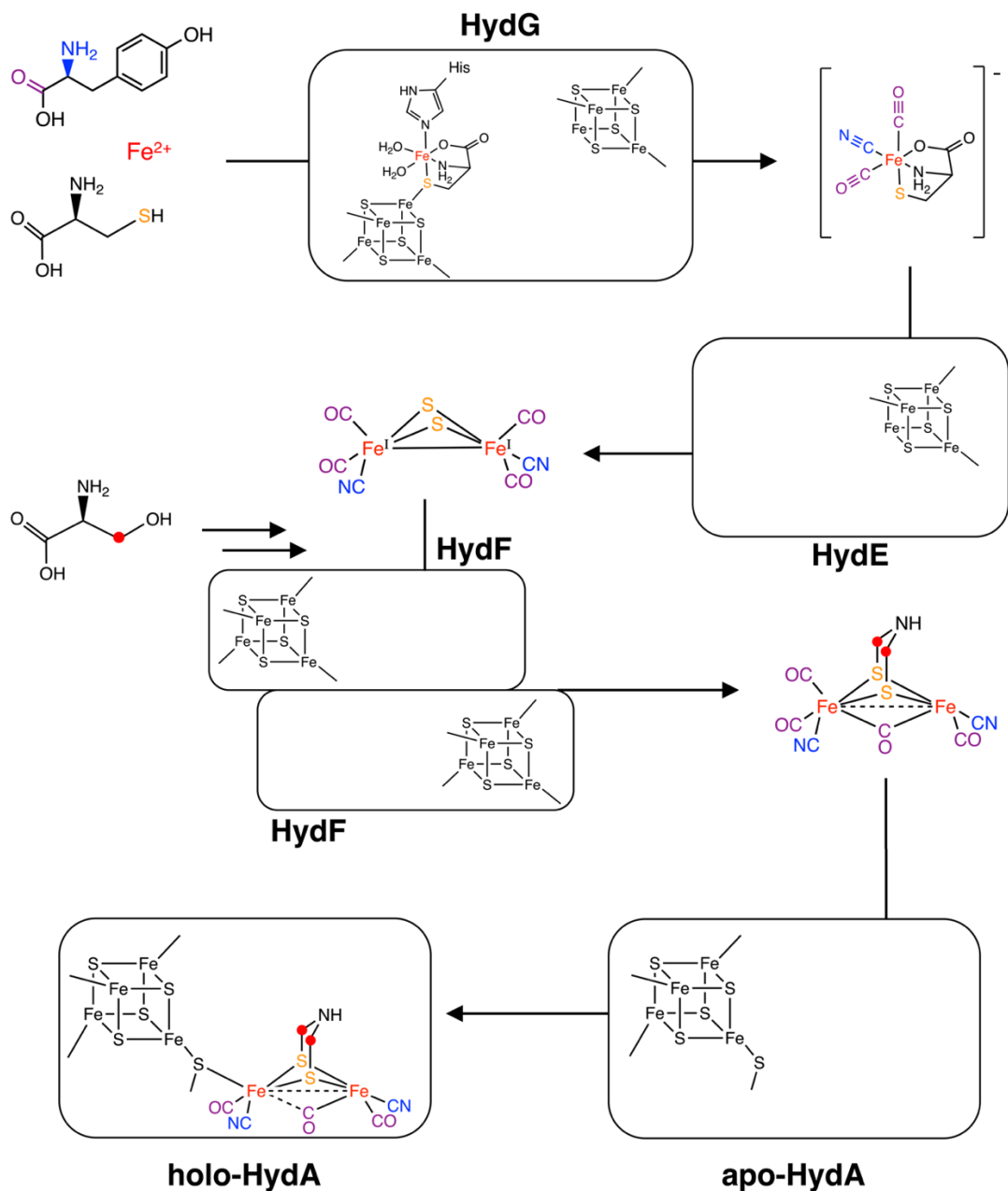
{H<sup>+</sup>} indicates a proton associated in the active site, close to the H-cluster. The cube represents the [4Fe-4S] cluster linked to the dinuclear Fe subcluster. The rectangular box around the dinuclear Fe represents the uncertainty in bonding during catalytic turnover between Fe and the CO and CN ligands.<sup>20</sup>

Two “resting states” exist for [FeFe]-hydrogenase during the catalytic cycle, the H<sub>ox</sub> and H<sub>red</sub> state. Following a model that involves proton coupled electron transfer, additional transient states can be proposed to complete the mechanism involving a metal hydride and completed H<sub>2</sub> molecule ([Fe(II)Fe(II)]H<sup>-</sup>, [Fe(II)Fe(I)]H<sub>2</sub>)(**Scheme 2.2.2.**)<sup>12, 21, 22</sup> Through this proposed catalytic mechanism, the [4Fe-4S] subcluster remains in the oxidized for all states except the H<sub>sred</sub> state. Protein cyclic voltammetry studies have shown that at the low potential where H<sub>sred</sub>

occurs, high catalytic currents from hydrogen production are observed.<sup>19</sup> This observation strongly suggests that the  $H_{\text{sred}}$  state is part of the catalytic mechanism. In the proposed catalytic mechanism, an available proton in the vicinity to the  $H_{\text{sred}}$  state would be able to quickly generate a hydride bound to the mixed valence state ( $H_{\text{ox}}$ ) which combines with a proton available at the adjacent amine group to form  $H_2$ , reestablishing the  $H_{\text{ox}}$  resting state. DFT and experimental studies support the hydride formed in the catalytic cycle to be a terminal hydride, in place of a more stable bridging hydride species.<sup>23-29</sup> The unique structure of the H-cluster and protein environment allow for this catalytic cycle to produce  $H_2$  up to  $\sim 10^4$  molecules per second at room temperature.<sup>30</sup>

Our research into the chemistry of the active site of the [FeFe]-hydrogenase has recently focused on its biosynthesis involving three Fe-S cluster containing “maturase” enzymes, HydE, HydF, and HydG.<sup>31-33</sup> In addition to the three maturases, the biosynthesis of the [2Fe] H-cluster requires low molecular weight components, including some amino acids and small molecule cofactors (**Scheme 2.2.1**). Two of these maturases, HydE and HydG, belong to the radical S-adenosyl-L-methionine (SAM) superfamily of enzymes.<sup>2</sup> Evidence suggests a sequential mechanism for the maturation, from HydG to HydE and finally HydF (**Scheme 2.2.3**).<sup>34</sup> Much of the biosynthetic mechanism has come as the result of studying HydG, HydE, and HydF *in vivo* and *in vitro* by heterologously expressing the proteins from *Clostridium acetobutylicum* and *Shewanella oneidensis*. *E. Coli* having only the *hydA1* gene produces a protein with only the [4Fe-4S]<sub>H</sub> component of the H-cluster.<sup>35</sup> This apo-HydA can be activated with protein extract containing HydE, HydF, and HydG.<sup>36</sup> Kuchenreuther et al. demonstrated the ability to carry out an *in vitro* maturation with individually expressed HydE, HydF, and HydG.<sup>37</sup> Results highlighted that only HydG was absolutely required for producing active [FeFe] hydrogenase. In

another separate semisynthetic approach,  $[\text{Fe}_2(\text{adt})(\text{CN})_2(\text{CO})_4]^{2-}$  was prepared and shown to be capable of maturing an apo-HydA, including in the absence of HydF.<sup>38,39</sup>



**Scheme 2.2.3.** Sequential model for the biosynthesis of the H-cluster in [FeFe]-hydrogenase from the maturase enzymes HydE, HydF, and HydG using molecular components L-Tyr, L-Cys, and L-Ser.<sup>34</sup>

The maturase enzymes HydE, HydF, and HydG each play a unique role in the maturation of the H-cluster, of which many of mechanistic details are currently being resolved. HydG, a known Radical SAM enzyme, uses SAM to cleave L-Tyrosine (L-Tyr) to produce dehydroglycine (DHG) and *p*-cresol as a byproduct.<sup>40</sup> This cleavage is analogous to the enzyme ThiH.<sup>41</sup> HydG is responsible for producing CO and CN<sup>-</sup> from the substrate L-Tyr that eventually bind to produce a [Fe(II)(CN)(CO)<sub>2</sub>(cysteinate)]<sup>-</sup> product, which will be discussed in detail in the following section. The remaining components found on the completed H-cluster that are not sourced from the product of HydG, are the CH<sub>2</sub>NHCH<sub>2</sub> of the adt bridge. It was originally proposed that the bridge was assembled and installed by HydE alone, but recent evidence suggested additional proteins are needed for the complete assembly of the bridge.<sup>33,42,43</sup> The detailed mechanism for HydE and HydF is currently under investigation.

### 2.3. The Catalytic Mechanism for the Radical SAM enzyme HydG

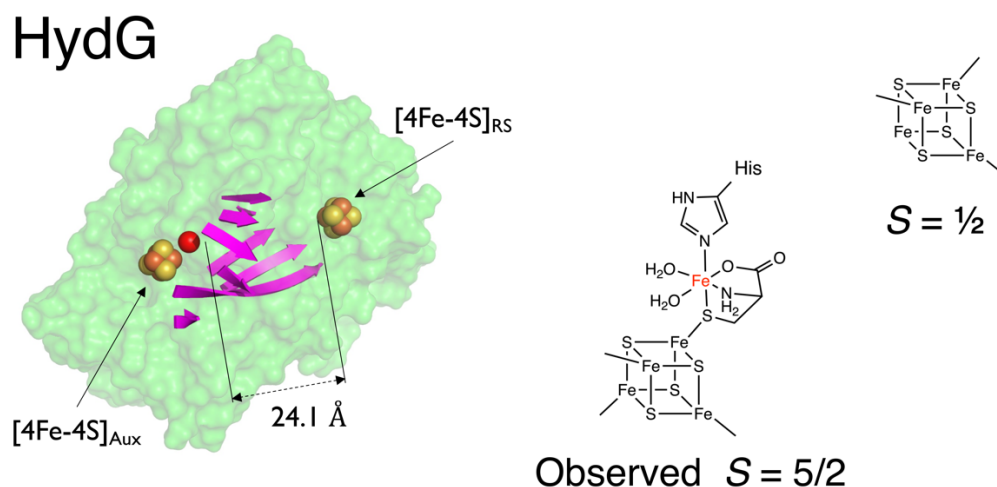
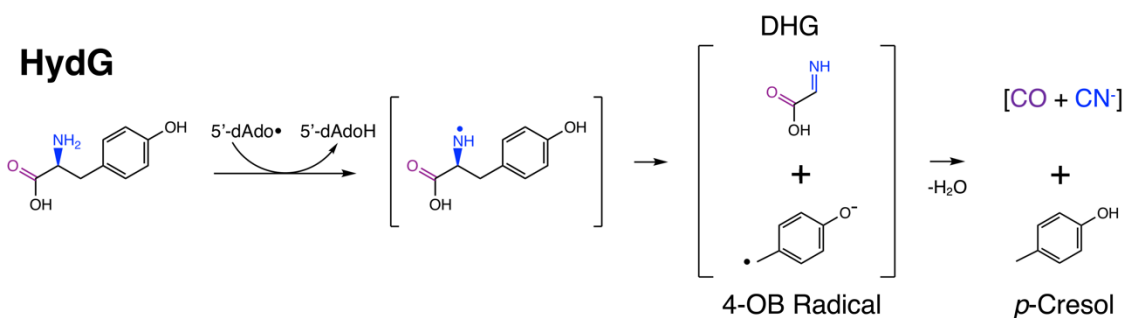


**Figure 2.3.1.** (Left) HydG with observed Fe-S clusters in the reduced state (Right). pdb: 4WCX

A variety of experiments, crucially including  $^{57}\text{Fe}$  ENDOR studies, have shown that the biosynthesis of the H-cluster begins with HydG.<sup>44,45</sup> HydG is a bifunctional enzyme, containing two Fe-S clusters, a N-terminal  $[4\text{Fe-4S}]_{\text{RS}}$  cluster, and a C-terminal  $[4\text{Fe-4S}]_{\text{aux}}$  cluster (**Figure 2.3.1**). The C-terminal  $[4\text{Fe-4S}]_{\text{aux}}$  cluster is unique, being linked to an additional fifth “dangler” Fe(II) by the thiolate of a labile cysteine.<sup>46</sup> The overall HydG reaction converts tyrosine, cysteine, and Fe(II) to the  $[\text{Fe(II)(CN)(CO)}_2(\text{cysteinate})]^-$  product (or “synthon”). The process begins at the  $[4\text{Fe-4S}]_{\text{RS}}$  cluster, which generate a 5'-deoxyadenosyl radical (5'-dAdo•) that abstracts an H-atom from the amine of its substrate L-tyrosine (L-Tyr). This dehydrotyrosyl radical fragments at its  $\text{C}_\alpha\text{-C}_\beta$  bond to give a 4-oxidobenzyl radical (4OB•) that is observable by EPR,<sup>47,48</sup> along with a proposed dehydroglycine (DHG) intermediate (**Scheme 2.3.1**). Fe-bound CO and  $\text{CN}^-$  are formed from the DHG intermediate via a radical cascade, as unveiled by computational QM/MM studies.<sup>34,49</sup> Time-resolved FTIR and freeze quench EPR experiments have been used to follow the details of CO and  $\text{CN}^-$  binding to the dangler Fe. The first tyrosine lysis leads to an intermediate, Complex A, with one  $\text{CN}^-$  and one CO bound. A second tyrosine lysis leads to the  $[\text{Fe(II)(CN)(CO)}_2(\text{cysteinate})]^-$  product, termed Complex B, and a cyanide-bound  $[4\text{Fe-4S}]_{\text{aux}}$  cluster that is regenerated into the resting state of HydG with exogenous cysteine and  $\text{Fe}^{2+}$  (**Scheme 2.3.2**).<sup>44,50</sup> This  $[\text{Fe(II)(CN)(CO)}_2(\text{cysteinate})]^-$  product then serves as the substrate for the second radical SAM enzyme HydE<sup>51-53</sup>, which activates the inert low spin Fe(II) complex for dimerization, either within HydE or on the protein HydF<sup>34</sup>. This dimerization results in the formation of an  $\text{Fe}_2\text{S}_2(\text{CO})_4(\text{CN})_2$  species needing only the addition of the  $\text{CH}_2\text{NHCH}_2$  component of the adt bridge to complete the binuclear subcluster. Semisynthetic approaches to [2Fe] H-cluster biosynthesis have shown that a synthetic version of Complex B, termed Syn-B, is also capable of in vitro maturation by acting as the substrate for HydE in the

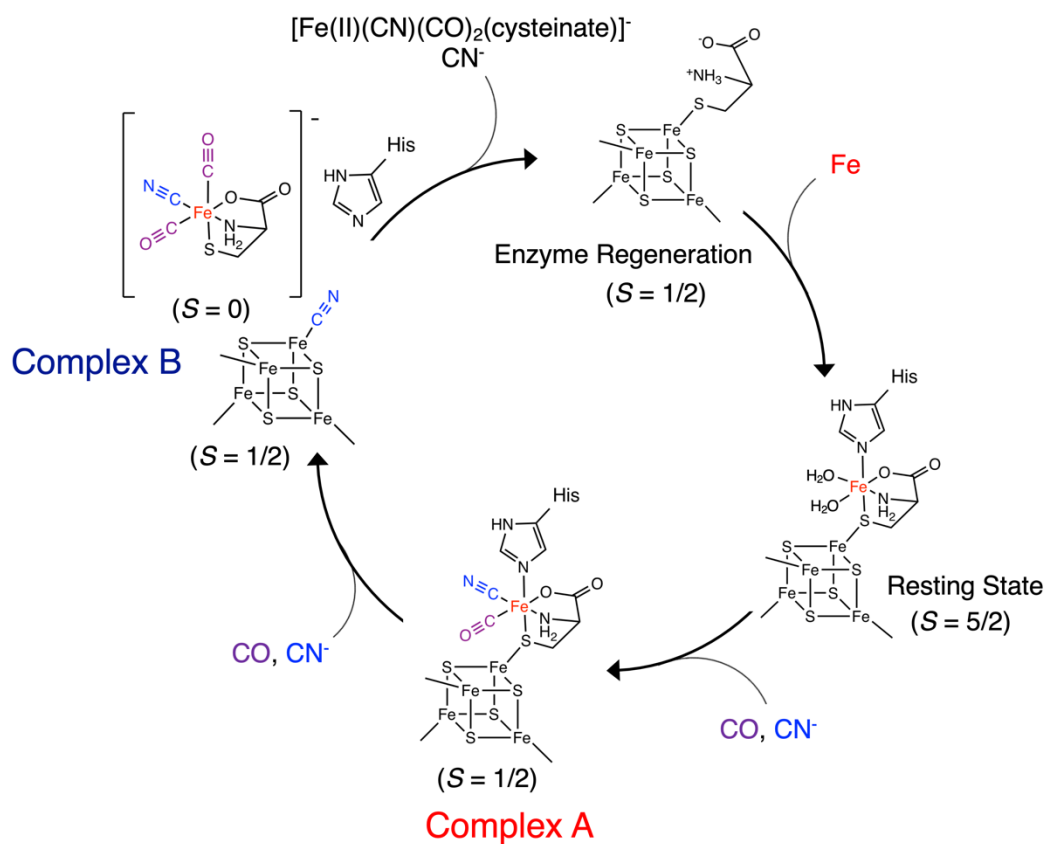
absence of HydG.<sup>51,52</sup> This highlights the importance of the [Fe(II)(CN)(CO)<sub>2</sub>(cysteinate)]<sup>-</sup> organometallic product structure along the maturation pathway and preventing the release of cytotoxic CO and CN<sup>-</sup>.



**Scheme 2.3.1.** Proposed mechanism by which the [4Fe-4S]<sub>RS</sub> cluster of HydG cleaves L-Tyr into *p*-Cresol, CO and CN<sup>-</sup>.

When reduced by dithionite (DTH), HydG typically displays two EPR signals: an  $S = \frac{1}{2}$  signal corresponding to the [4Fe-4S]<sub>RS</sub> (RS = radical SAM) cluster, and a distinctive  $S = 5/2$  signal corresponding to a unique [5Fe-4S]<sub>aux</sub> cluster. This unique [5Fe-4S]<sub>aux</sub> cluster is composed of a [4Fe-4S]<sub>aux</sub> cluster coupled to a dangler Fe ion (high spin,  $S = 2$  before CO/CN binding) (**Figure 2.3.3**).<sup>46, 47, 54-56</sup> The latter  $S = 5/2$  signal serves as a useful spectroscopic marker for monitoring conversion of the [5Fe-4S]<sub>aux</sub> cluster into Complex A and Complex B. This indirect probe allows monitoring of the conversion of the ferrous “dangler” to low spin ( $S = 0$ ) state upon the CO/CN<sup>-</sup> binding (**Scheme 2.3.2**).





**Scheme 2.3.2.** Proposed mechanism by which the auxiliary cluster of HydG generates an  $[\text{Fe}(\text{II})(\text{CN})(\text{CO})_2(\text{cysteinate})]^-$  (Complex B) with Complex A as an intermediate.

The chemistry of HydG is initiated by reductant in the presence of SAM and L-Tyr, which induces generation of CO and  $\text{CN}^-$  at the radical SAM site. As initially determined by FTIR spectroscopy,<sup>44</sup> freeze quenching about 30 s after the addition of SAM, L-Tyr, and reductant gives Complex A. According to EPR spectroscopic analysis, the cryotrapped Complex A consists of a reduced  $[4\text{Fe}-4\text{S}]_{\text{aux}}-\text{Fe}(\text{CO})(\text{CN})-\text{L-cysteinate}$  species. Complex A is characterized by a rhombic  $S = 1/2$  EPR signal with  $g = [2.057, 1.920, 1.883]$  (**Figure 2.3.2**).<sup>50</sup> Freeze quenching at longer times (ca. 5 minutes) reveals a new species, characterized by an EPR

signal also indicative of an  $S = 1/2$  species ( $g = [2.084, 1.930, 1.925]$ ), assigned to the adduct  $[4\text{Fe-4S}]_{\text{aux}}\text{-CN}$  produced alongside Complex B (**Figure 2.3.3, Figure 2.3.4**). The timescale for the evolution of Complex B by EPR and FTIR spectroscopies match.

The two  $S = 1/2$  sets of signals are assigned to  $\text{Fe(II)(Cys)(CN)(CO)}_x$  species bound to the  $[4\text{Fe-4S}]_{\text{aux}}$  cluster. These species are the 5Fe ensembles Complex A- $[4\text{Fe-4S}]_{\text{aux}}$  ( $x = 1$ ) and Complex B- $[4\text{Fe-4S}]_{\text{aux}}$  ( $x = 2$ ), respectively. In the former, the dangler Fe(II) site is bound to Cys, CO,  $\text{CN}^-$  and a protein histidine. The coordination sphere of the dangler Fe in Complex B- $[4\text{Fe-4S}]_{\text{aux}}$  is better defined, consisting of tridentate Cys, as well as  $\text{CN}^-$  and two CO ligands. Subsequent to the formation of Complex A- $[4\text{Fe-4S}]_{\text{aux}}$ , two processes occur, the lysis of a second tyrosine produces one equiv each of CO and  $\text{CN}^-$ . These ligands attack the 5Fe ensemble Complex A- $[4\text{Fe-4S}]_{\text{aux}}$  sequentially. First the CO binds to the dangler Fe to give the 5Fe ensembles Complex B- $[4\text{Fe-4S}]_{\text{aux}}$ . Subsequently, the second  $\text{CN}^-$  attacks the site-differentiated Fe of the  $[4\text{Fe-4S}]$  cluster, displacing Complex B and forming an EPR-detectable cyanide-bound  $[4\text{Fe-4S}]_{\text{aux}}$  cluster (**Scheme 2.3.2**).<sup>54</sup> The released  $[\text{Fe(II)(CN)(CO)}_2(\text{cysteinate})]^-$  complex then transfer to HydE, the next enzyme on the biosynthesis pathway. The EPR signal assigned to  $[4\text{Fe-4S}]_{\text{aux}}\text{-CN}$  continues to increase when the enzyme is allowed to turnover for up to 60 min (**Section 2.3.3**). At this stage, the  $S = 5/2$  EPR signal from the resting state  $[5\text{Fe-4S}]$  cluster nearly vanishes. Thus, all of  $[4\text{Fe-4S}]_{\text{aux}}$  is poised in the CN-bound state alongside the production of Complex B. In addition, the contribution of Complex A in the  $S = 1/2$  region of the EPR spectrum also disappears, at which point nearly all the dangler Fe is converted to Complex B (**Figure 2.3.3, Figure 2.3.4**).

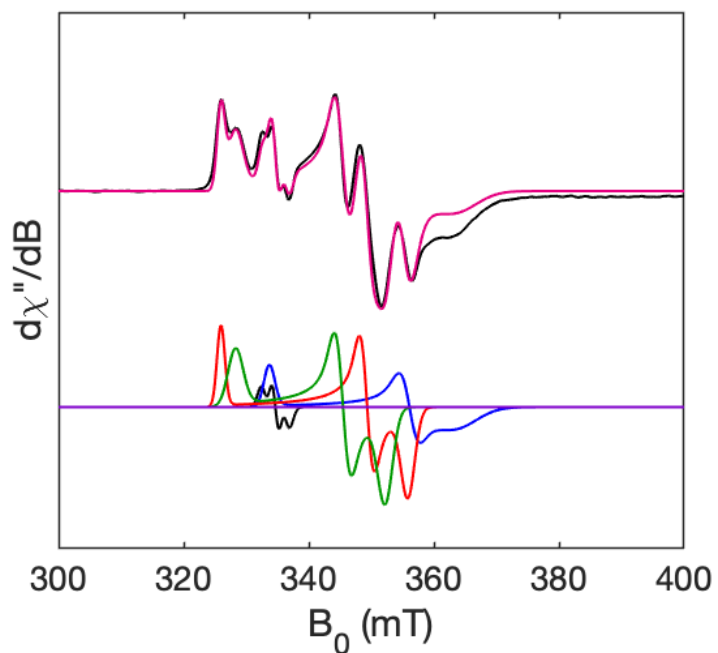


**Figure 2.3.2.** X-band (9.4 GHz) CW EPR of HydG after turnover for 24s with DTH, SAM, and L-Tyr (black trace), and total simulation (magenta trace). Bottom: simulations of the top black trace with three species: SAM-bound  $[4\text{Fe-4S}]_{\text{RS}^+}$  cluster (26.3%, blue trace), unknown structure (37.6%, green trace), Complex A (36.1%, red trace), and OB radical (<1%, black trace). The parameters for X-band (9.4 GHz) CW EPR are temperature, 10 K; microwave power, 0.1 mW; modulation amplitude, 0.5 mT.<sup>50</sup>

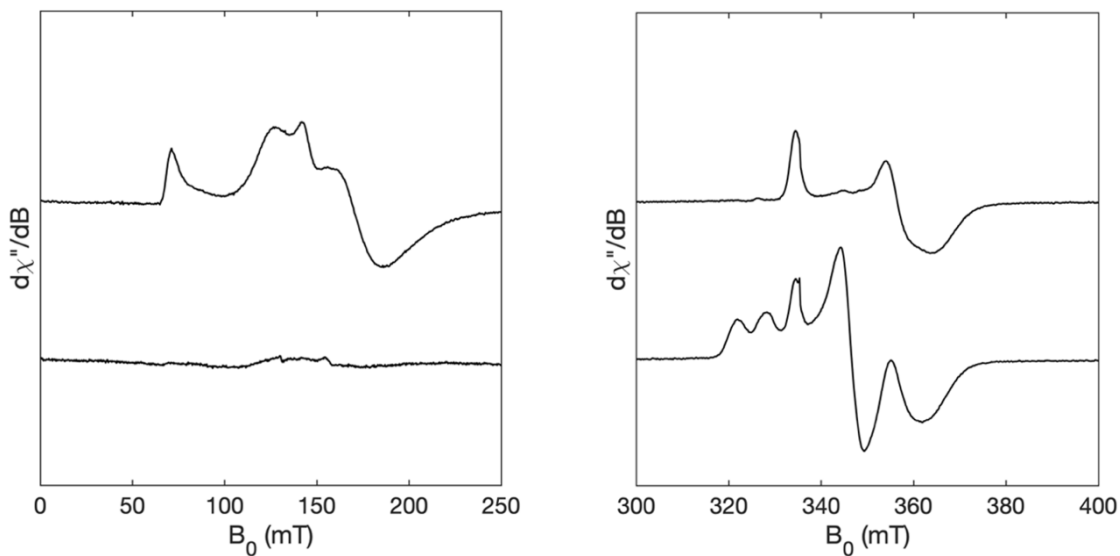


**Figure 2.3.3.** X-band (9.4 GHz) CW-EPR of HydG (Top) in the presence of DTH and SAM. (Bottom) HydG after 60 min turnover in the presence of DTH, SAM, and L-Tyr. Conditions: temperature, 10 K; microwave power 1 mW (Left), 0.1 mW (Right); modulation amplitude, 0.5 mT.

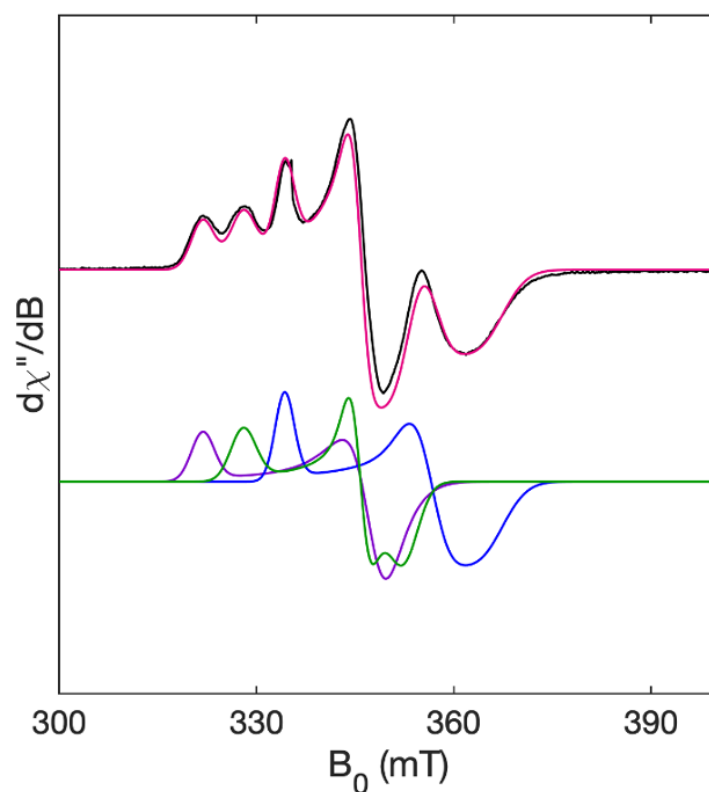


**Figure 2.3.4.** X-band (9.4 GHz) CW EPR of HydG after turnover for 60 min with DTH, SAM, and L-Tyr (black trace), and total simulation (magenta trace). Bottom: simulations of the top black trace with three species SAM-bound  $[4\text{Fe-4S}]_{\text{RS}}^+$  cluster (44%, blue trace), unknown structure (27%, green trace), and CN-bound  $[4\text{Fe-4S}]_{\text{Aux}}^+$  cluster (29%, purple trace). The parameters for X-band (9.4 GHz) CW EPR are temperature, 10 K; microwave power, 0.1 mW; modulation amplitude, 0.5 mT.

## 2.4 Materials and Methods

Non-isotopically enriched chemicals were purchased from common commercial vendors. Tyrosine solutions were prepared by first dissolving L-tyrosine to a final concentration of 200 mM in 600 mM KOH solution, followed by diluting into 100 mM Hepes buffer (pH = 7.2).

### 2.4.1 Expression and Purification of HydG

The pET-21(b) Strep-tag II-hydG was used to produce the *Shewanella oneidensis* (*So*)HydG<sup>WT</sup> containing an N-terminal affinity tag. HydG was expressed in *Escherichia coli* strain BL21(DE3)  $\Delta$ iscR strain under anaerobic conditions (<2 ppm O<sub>2</sub>). Four liters of cells were grown in 25 g/L LB media containing 40  $\mu$ g/L kanamycin, 100  $\mu$ g/mL ampicillin, 4 mM Fe<sup>3+</sup>, 0.5% (w/v) glucose and 100 mM 3-(N-morpholino)propane sulfonic acid (MOPs, pH = 7.8), at 30°C to an OD<sub>600</sub> of ~0.5. The cultures were pooled, transferred to an anaerobic chamber, and supplemented with 5 mM L-Cys and 10 mM fumarate. The pooled culture was stirred in the anaerobic chamber at room temperature (25 °C) for 1 hr to use up the remaining oxygen, then induced by 0.50 mM isopropyl  $\beta$ -D-1-thiogalactopyranoside (IPTG). Cells were further incubated in the anaerobic chamber with gentle stirring at room temperature for 20 h before transferred into the centrifugation bottles (inside the glovebox) and pelleted by centrifugation. The cells were then lysed using 1x BugBuster<sup>®</sup> Protein Extraction Reagent (Novagen), in HEPES pH = 8.0, with freshly-made sodium dithionite, 25 U/mL benzonase, 1 kU/mL rLysozyme (EMD Millipore) and EDTA-free protease inhibitor table (Roche). Lysates were clarified by centrifugation for 15 min at 18,000 rpm. HydG was isolated using a Strep-Tactin<sup>®</sup> Superflow<sup>®</sup> high capacity resin (IBA GmbH) washed with 50 mM HEPES buffer (pH = 8.0) with 50 mM KCl and eluted with 50 mM HEPES buffer (pH = 8.0) with 50mM KCl and 3.0 mM desbiotin .

The HydG protein eluate fractions were frozen using liquid N<sub>2</sub> in the as-isolated state and without desalting or concentration.

#### **2.4.2 Sample Preparation**

EPR samples were prepared in an anaerobic glove box under a N<sub>2</sub> atmosphere (< 2 ppm O<sub>2</sub>) and frozen using liquid nitrogen before spectroscopic analysis. Unless otherwise indicated, the final substrate concentrations for these samples and all other samples were as follows: freshly thawed HydG fractions, ~100-300  $\mu$ M was concentrated to a final sample concentration of 700 – 1000  $\mu$ M; DTH, 10 mM; L-Tyr, 10 mM; SAM, 5 – 10 mM; L-Cys, 5 mM. Other than HydG, each component was added as a solution of 10-fold to 20-fold higher concentration than its final concentration. For example DTH (4  $\mu$ L at 200 mM), L-Tyr (8  $\mu$ L at 100 mM), SAM (8  $\mu$ L at 100 mM), to HydG (60  $\mu$ L at 1000  $\mu$ M). Reagents were added in the order DTH, SAM, and L-Tyr to initiate turnover.

#### **2.4.3 Continuous-wave (CW) EPR Spectroscopy & Mössbauer spectroscopy**

EPR spectroscopy was performed in the Cal-EPR center in Department of Chemistry, University of California at Davis. CW-EPR experiments were performed on the Bruker Biospin EleXsys E500 spectrometer with a super high Q resonator (ER4122SHQE) in perpendicular mode. Cryogenic temperatures were achieved by using ESR900 liquid helium cryostat with a temperature controller (Oxford Instrument ITC503) and gas flow controller. All CW-EPR spectra were recorded under slow-passage, non-saturating conditions. Spectrometer settings were as following: conversion time = 60 ms, modulation amplitude = 0.5 mT, modulation frequency = 100 kHz, and other settings as given in the corresponding figure captions.

Simulations of CW and pulse EPR spectra were performed in Matlab 2021a with EasySpin 5.2.35 toolbox<sup>57</sup>.

Mössbauer spectra were recorded at zero field on a See Co. MS4 spectrometer equipped with a Janis 9T MOSS-OM-12SVT cryostat. Spectra were calibrated using an Fe foil standard at room temperature. Spectra were processed and least-squares fit using MossWinn. Quadrupole doublets were fit to Voigt profiles with Lorentzian linewidths and variable Gaussian linewidths.

## 2.5. Zero-Field Splitting of the Aux-Cluster in HydG

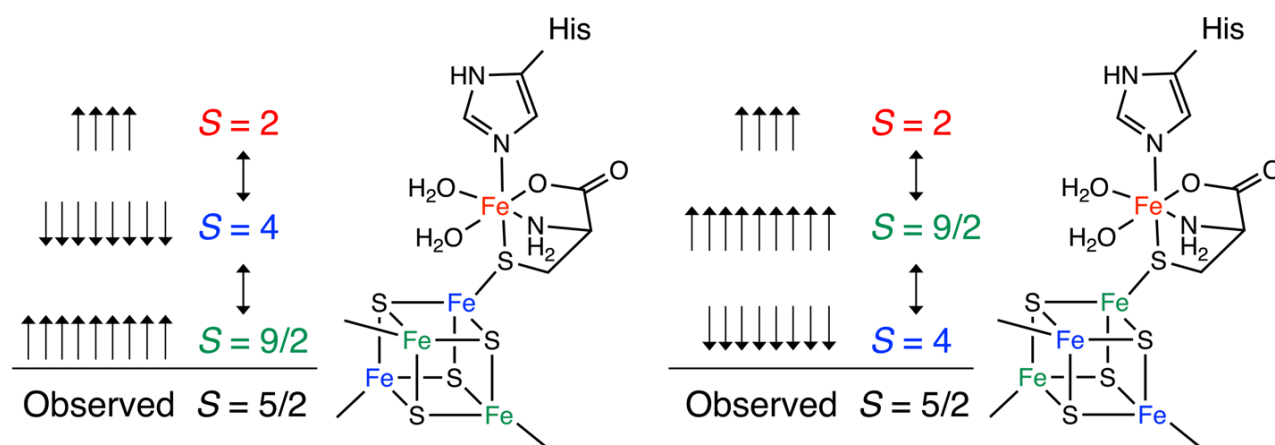


**Figure 2.5.1.** Exchange coupling scheme for the auxiliary cluster of HydG with antiferromagnetic (Left) and ferromagnetic (Right) exchange. Blue:  $[\text{Fe}^{2+}\text{Fe}^{2+}]$  mixed-valence pairs; green  $[\text{Fe}^{2.5+}\text{Fe}^{2.5+}]$  mixed-valence pairs; and red:  $\text{Fe}^{2+}$  “dangler” ion.<sup>46</sup>

The auxiliary cluster of HydG is composed of a  $[\text{4Fe-4S}]^+$  aux-cluster,  $S = \frac{1}{2}$ , coupled to a high spin Fe(II),  $S = 2$ , giving the observed  $S = 5/2$  species when reduced (**Figure 2.5.1**).<sup>46</sup> The unpaired electron’s energy levels arrange into “Kramer’s doublets”, separated by a few wave



numbers in the absence of magnetic fields (**Section 1.1.5**). When magnetic fields are applied these Kramer's doublets split into spin up and spin down sublevels. EPR absorption will be observed when the operating frequency matches the splitting produced by the magnetic field strength, transitioning an electron's spin state. If  $D > 0$ , the energy difference between the lowest-lying Kramer's doublet and the middle doublet for a  $S = 5/2$  paramagnetic system will be equal to  $2D$ , whereas the difference between the middle and uppermost doublet will equal to  $4D$  (**Figure 1.1.5.2**). When the temperature approaches very low values ( $\sim 1\text{K}$ ), the spins will populate only the lowest Kramer's doublet. Increasing the temperature causes the spins to populate the middle and upper doublets until the temperature is raised high enough that each doublet approaches equal  $1/3$  spin population. To determine the zero-field splitting of the  $S = 5/2$  auxiliary cluster in HydG, the temperature dependence was examined from 5K to 20K for *SoHydG* (**Figure 2.5.2**) and *TiHydG* (**Figure 2.5.5**). Analysis to determine the zero field splitting value  $D$ , was done by fitting the peak intensity at  $g_{\text{eff}} = 9.5$  and  $g_{\text{eff}} = 4.7$  to a Boltzmann distribution (**Equation 2.5.1, and 2.5.2**).<sup>58</sup>

$$\text{Amplitude} \propto \frac{\exp\left(-\frac{Z}{kT}\right)}{T\left[1 + \exp\left(-\frac{Z}{kT}\right) + \exp\left(-\frac{2Z}{kT}\right)\right]} \quad \text{Eq. 2.5.1}$$

$$\text{Intensity} \propto \frac{\exp\left(-\frac{3.2D}{T}\right)}{T\left[1 + \exp\left(-\frac{3.2D}{T}\right) + \exp\left(-\frac{6.8D}{T}\right)\right]} \quad \text{Eq. 2.5.2}$$

**Equation 2.5.1.** EPR Intensity/Amplitude relationship with temperature and zero field splitting.

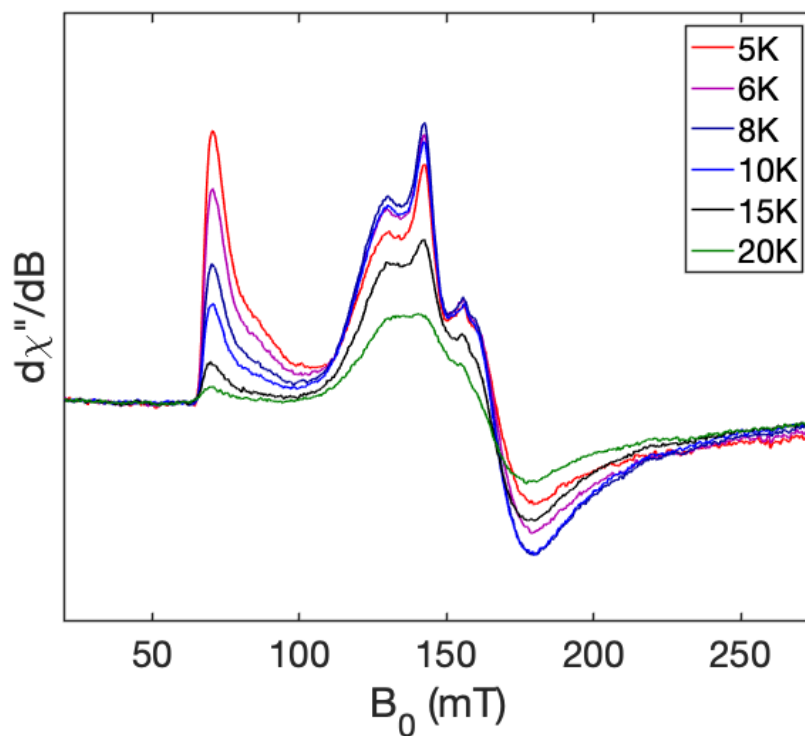


**Figure 2.5.2.** CW EPR of *SoHydG* auxiliary cluster at various temperatures: 5 K (red trace), 6 K (purple trace), 8 K (navy trace), 10 K (blue trace), 15 K (black trace), and 20 K (green trace). The parameters for X-band (9.4 GHz) CW EPR are temperature, 10 K; microwave power, 5 mW; modulation amplitude, 0.5 mT.

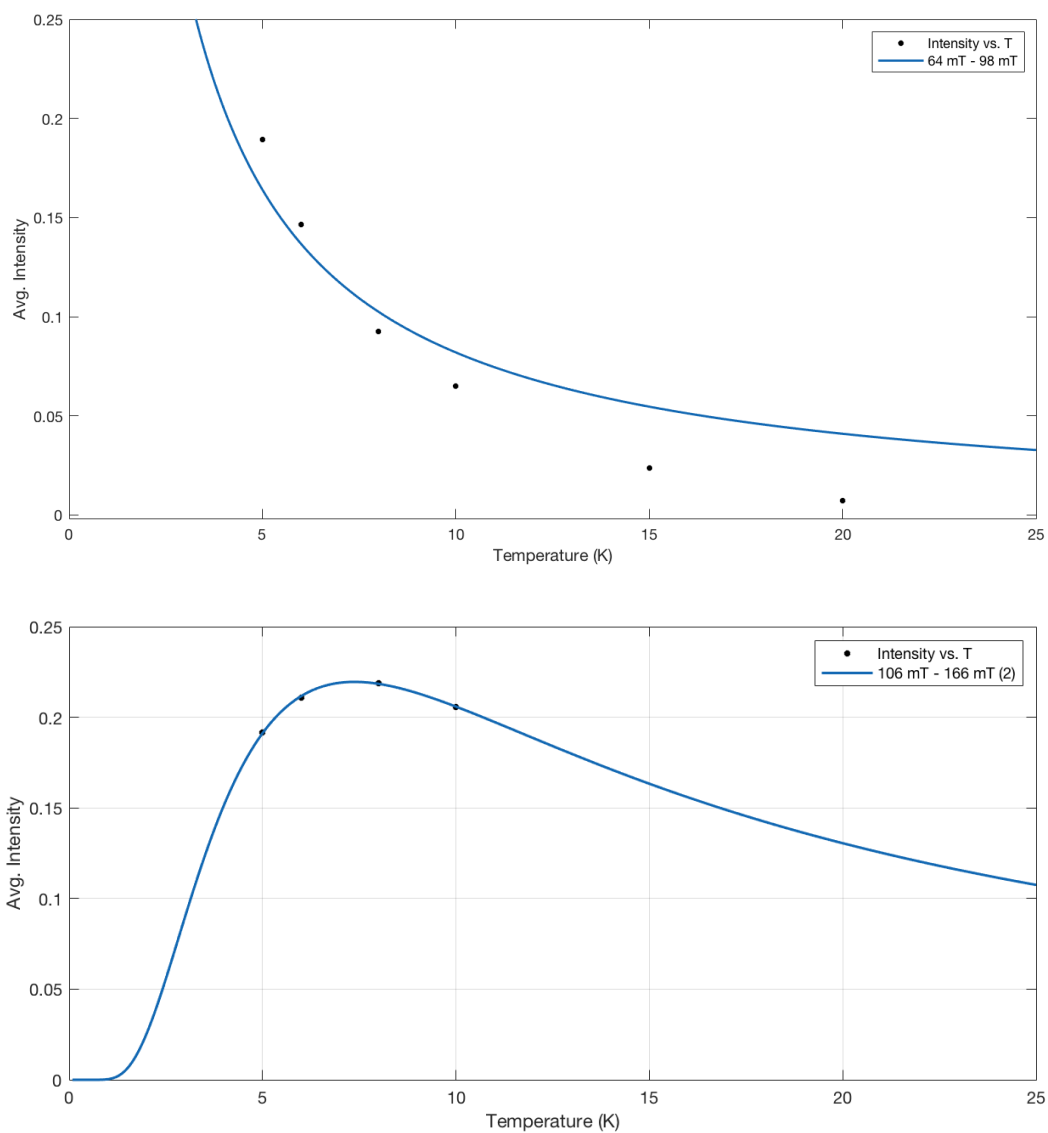


**Figure 2.5.3.** *SoHydG* temperature dependence peak intensity at (Top)  $g_{\text{eff}} = 9.5$  (64-98 mT) and (Bottom)  $g_{\text{eff}} = 4.7$  (106–166mT) fit to **Equation 2.5.1**. Only the lowest 4 temperatures were used in the second trace to improve the accuracy of the fit.

Data may also be fit to a Boltzmann equation having the form:

$$C \frac{I_1}{I_2} = e^{-\Delta E/kT}$$
$$\ln \frac{I_1}{I_2} = -\frac{\Delta E}{kT} - \ln(C) \quad \Delta E = 2D$$

**Equation 2.5.2.** EPR signal intensity in relation to a Boltzmann distribution.

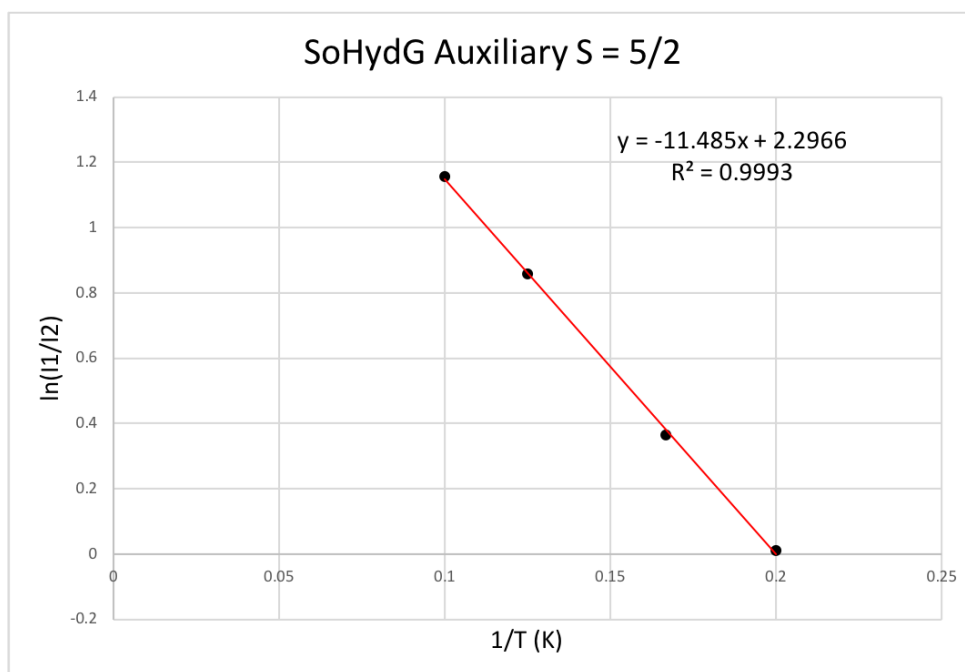


**Figure 2.5.4.** SoHydG temperature dependence peak intensity at  $g_{\text{eff}} = 9.5$  ( $I_2$ ) and  $g_{\text{eff}} = 4.7$  ( $I_1$ ) fit to **Equation 2.5.2**. Only the lowest 4 temperatures were used in the second trace to improve the accuracy of the fit.

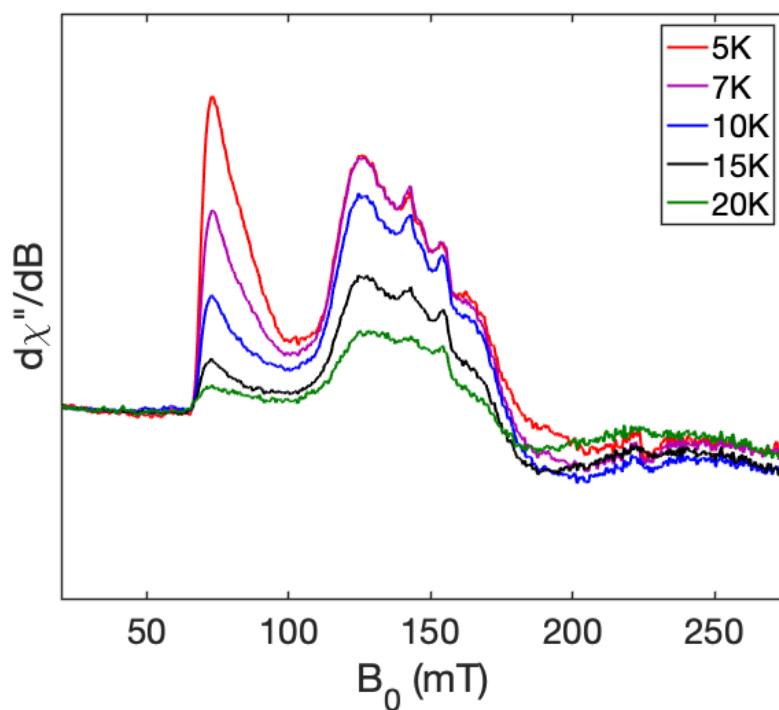


**Figure 2.5.5.** CW EPR of *TiHydG* auxiliary cluster at various temperatures: 5 K (red trace), 7 K (purple trace), 10 K (blue trace), 15 K (black trace), and 20 K (green trace). The parameters for X-band (9.4 GHz) CW EPR are temperature, 10 K; microwave power, 5 mW; modulation amplitude, 0.5 mT.

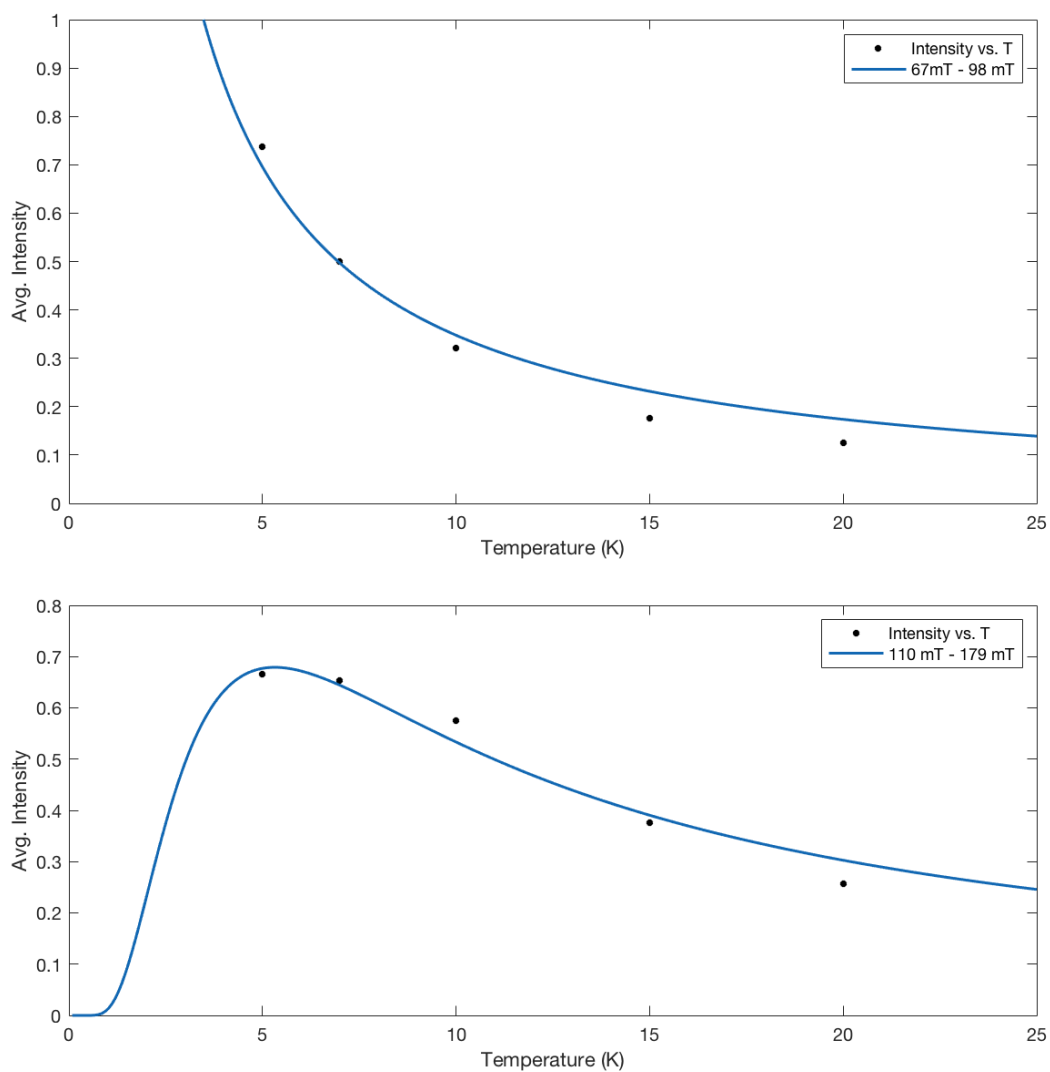


**Figure 2.5.6.** *TiHydG* temperature dependence peak intensity at (Top)  $g_{\text{eff}} = 9.5$  (64-98 mT) and (Bottom)  $g_{\text{eff}} = 4.7$  (106–166mT) fit to **Equation 2.5.1**.

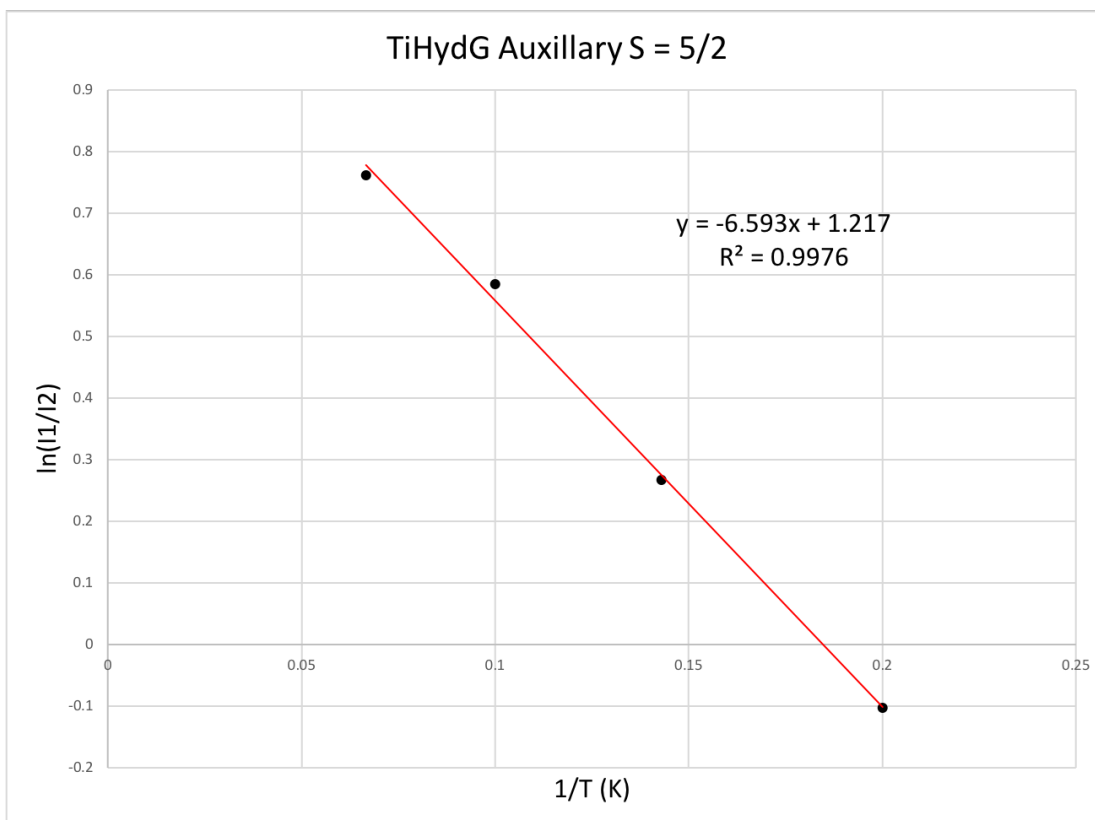


**Figure 2.5.7.** *TiHydG* temperature dependence peak intensity at  $g_{\text{eff}} = 9.5$  ( $I_2$ ) and  $g_{\text{eff}} = 4.7$  ( $I_1$ ) fit to **Equation 2.5.2**. Only the lowest 4 temperatures were used in the second trace to improve the accuracy of the fit.

Results for *SoHydG* temperature dependence data fit to **Equation 2.5.1** give a zero-field splitting  $D$  value of  $3.193 \text{ cm}^{-1}$ . When fit to **Equation 2.5.2**, the value of  $D = 3.989 \text{ cm}^{-1}$ . The discrepancy in values likely comes from the improved fit of the values to the latter equation. This suggests that  $D = 3.989 \text{ cm}^{-1}$  is a more accurate value, which agrees well with the previously published value of  $D = 4.5 \text{ cm}^{-1}$ .<sup>54</sup> Temperature dependence data for *TiHydG* when fit to **Equation 2.5.1**, gives  $D = 2.302 \text{ cm}^{-1}$ . When fit to **Equation 2.5.2**,  $D = 2.290 \text{ cm}^{-1}$  can be extracted. The close agreement in values indicates the accuracy of the zero-field splitting value of  $2.3 \text{ cm}^{-1}$  for the  $S = 5/2$  signal seen for *TiHydG*. Overall the difference seen in the value of  $D$

for *TiHydG* and *SoHydG*, reflects differences in the ligand environment created by the protein secondary structure for the high spin Fe(II) and [4Fe-4S] aux cluster.

## 2.6. Catalytic Turnover of HydG at Extended Periods

While the EPR species observed when HydG turns over at short time periods is well established (**Section 2.3**), the changes that occur at longer periods of time have been less known.<sup>50</sup> In order to establish species generated concomitantly with Complex B, EPR samples were freeze Quenched at time points >10 min (**Figure 2.6.1** and **Figure 2.6.4**). Simulating the individual EPR spectra (**Figure 2.6.2** and **Figure 2.6.5**) and mapping out the intensities gives a visual indication which species are changing during turnover (**Figure 2.6.3**). An EPR signal associated with a SAM-bound [4Fe-4S]<sub>RS</sub> cluster,  $g = [2.009 \ 1.884 \ 1.845]$  displays a cycling behavior, increasing and decreasing as the enzymes catalyzes the cleavage of L-Tyr. The EPR absorption associated with Complex A  $g = [2.058 \ 1.921 \ 1.885]$  equally shows a cycling pattern as it is converted into the product Complex B inside the enzyme. At time periods that display a decrease in SAM-bound [4Fe-4S]<sub>RS</sub> cluster and Complex A, it appears that the Unknown EPR species increases, though it is possible that it remains relatively constant over time. Close examination of cycling time points (**Figure 2.6.1** and **2.6.4**) reveals an additional species that steadily grows in with a shoulder at  $g = 2.083$ . This axial signal can be seen clearly when the spectra are simulated (**Figure 2.6.2** and **2.6.5**). This species is associated with a cyanide-bound [4Fe-4S]<sub>aux</sub><sup>+</sup> cluster,  $g = [2.083 \ 1.930 \ 1.925]$ , that is generated simultaneously with the formation of Complex B (**Scheme 2.3.2**). This species serves as an indirect marker to produce the diamagnetic product Complex B. Stopped flow FTIR data previously published indicated that the enzyme reaches a product maximum at 20 min. To examine if HydG under ambient conditions continues to produce more product Complex B if allowed to react for longer periods



of time, samples were prepared to observe turnover by EPR all the way up to 60 min (**Figure 2.6.6**). Once simulated, the EPR data becomes visually clear that the cyanide-bound  $[4\text{Fe-4S}]_{\text{aux}}^+$  cluster species continues to accumulate, indicating that product Complex B continues to be generated. This data establishes useful time points for future experiments completed with Mössbauer spectroscopy, to directly observe the product Fe in Complex B.

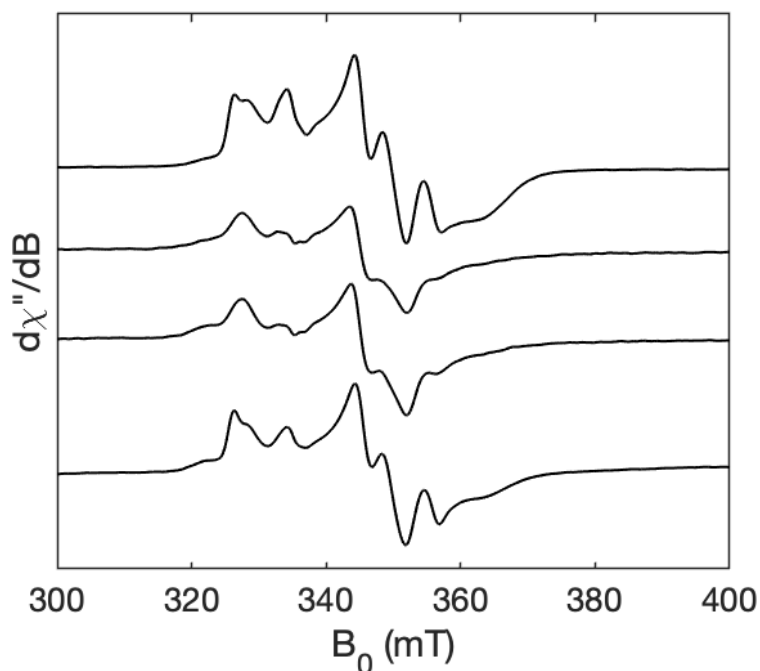


**Figure 2.6.1.** X-band (9.4 GHz) CW EPR of HydG after turnover from top to bottom 10 min, 15 min, 20 min, and 25 min with DTH, SAM, and L-Tyr. The parameters for X-band (9.4 GHz) CW EPR are temperature, 10 K; microwave power, 0.1 mW; modulation amplitude, 0.5 mT.

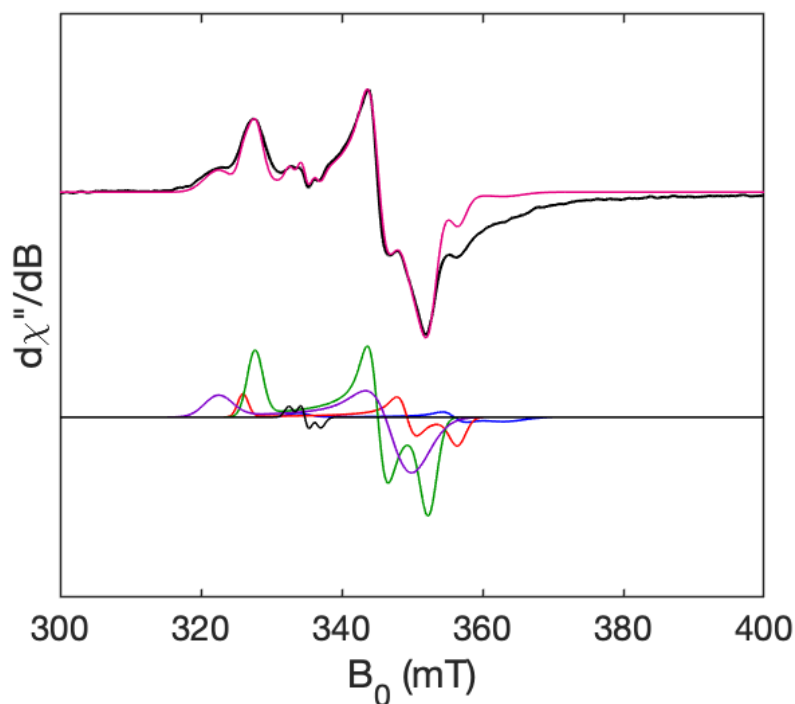


**Figure 2.6.2.** Top: CW EPR of HydG after turnover for 20 min with DTH, SAM, and L-Tyr (black trace), and total simulation (magenta trace). Bottom: simulations of the top black trace with four species SAM-bound  $[4\text{Fe-4S}]_{\text{RS}}^+$  cluster  $g = [2.009 \ 1.884 \ 1.845]$  (5%, blue trace), unknown structure  $g = [2.044 \ 1.943 \ 1.885]$  (46%, green trace), Complex A  $g = [2.058 \ 1.921 \ 1.885]$  (15%, red trace), and cyanide-bound  $[4\text{Fe-4S}]_{\text{aux}}^+$  cluster  $g = [2.080 \ 1.930 \ 1.920]$  (19%, purple trace) (Full simulation details in Supplemental Information). The parameters for X-band (9.4 GHz) CW EPR are temperature, 10 K; microwave power, 0.1 mW; modulation amplitude, 0.5 mT.

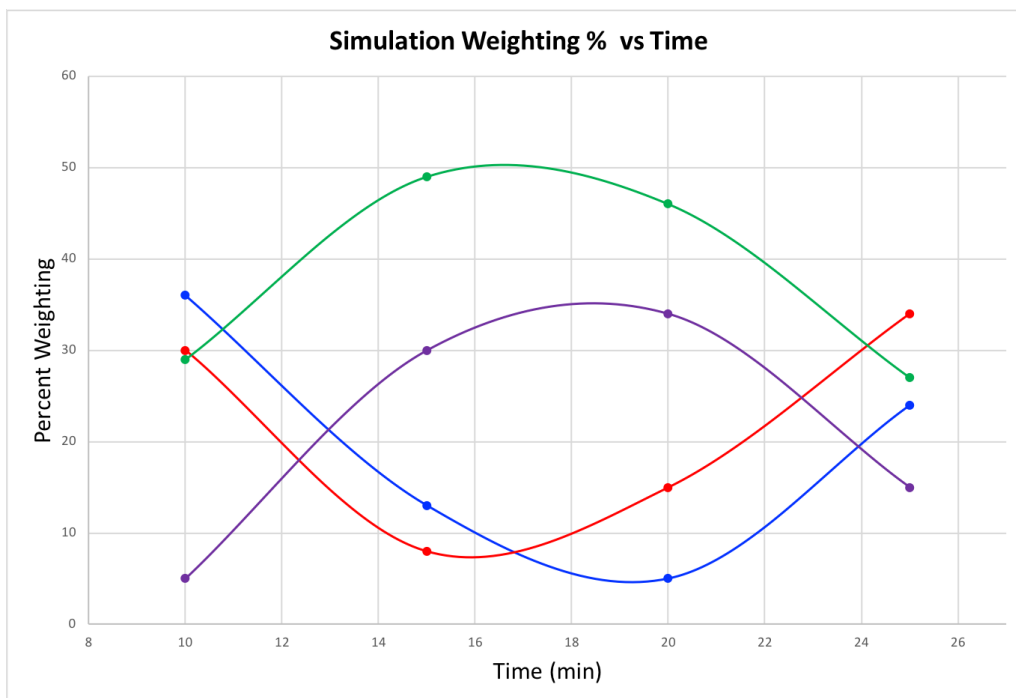


**Figure 2.6.3.** EPR simulation data from time point experiments in **Figure 2.6.1.**, plotted as a percentage of the overall simulation vs. time.

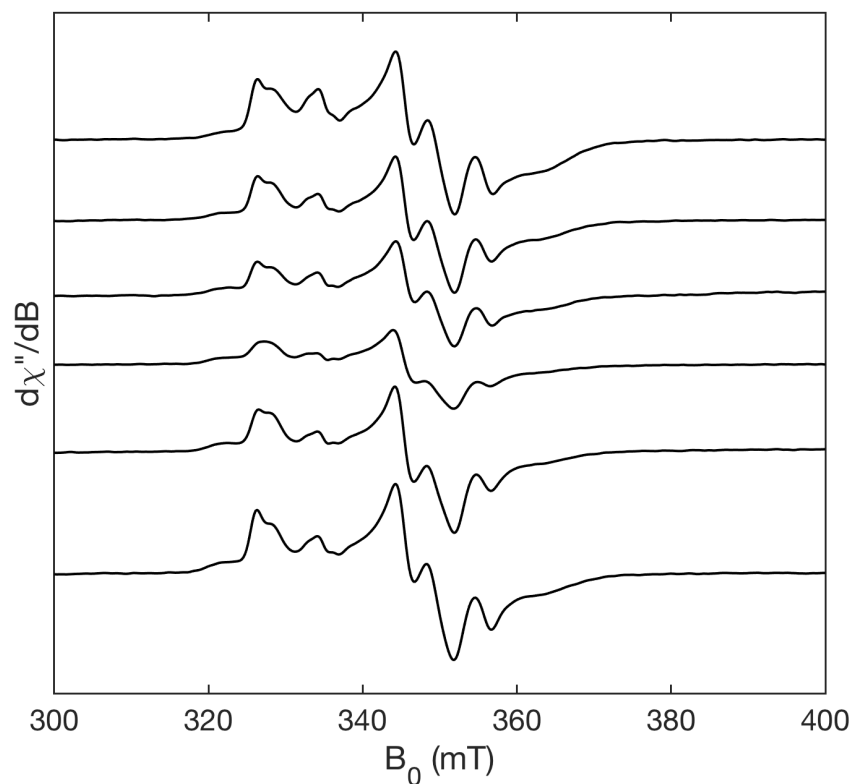


**Figure 2.6.4.** X-band (9.4 GHz) CW EPR of HydG after turnover from top to bottom 8 min, 11 min, 14 min, 16 min, 18 min, and 20 min with DTH, SAM, and L-Tyr. The parameters for X-band (9.4 GHz) CW EPR are temperature, 10 K; microwave power, 0.1 mW; modulation amplitude, 0.5 mT.

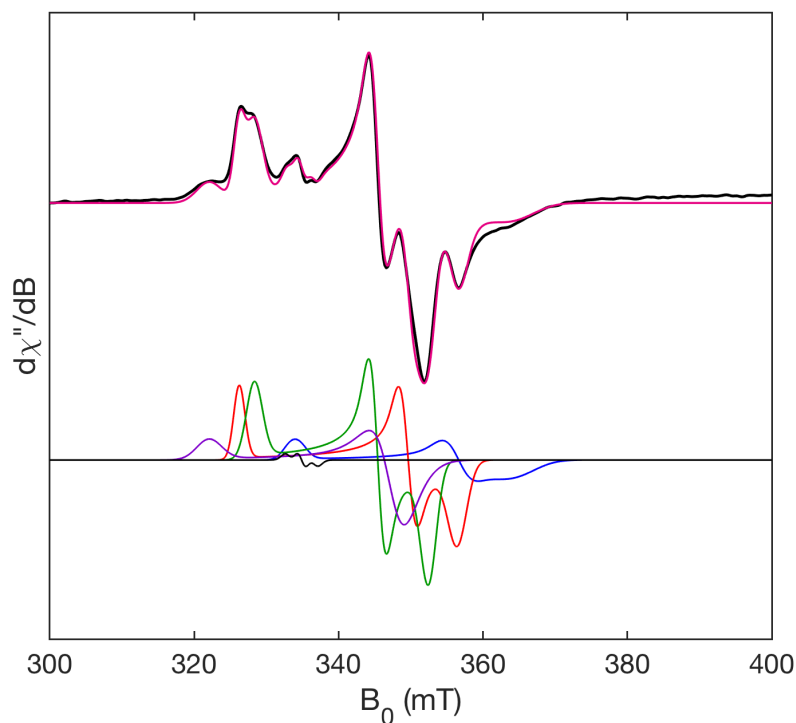


**Figure 2.6.5.** Top: CW EPR of HydG after turnover for 18 min with DTH, SAM, and L-Tyr (black trace), and total simulation (magenta trace). Bottom: simulations of the top black trace with four species SAM-bound  $[4\text{Fe-4S}]_{\text{RS}^+}$  cluster  $g = [2.009 \ 1.881 \ 1.842]$  (15%, blue trace), unknown structure  $g = [2.044 \ 1.943 \ 1.904]$  (35%, green trace), Complex A  $g = [2.057 \ 1.919 \ 1.883]$  (31%, red trace), and cyanide-bound  $[4\text{Fe-4S}]_{\text{aux}^+}$  cluster  $g = [2.083 \ 1.930 \ 1.925]$  (19%, purple trace) (Full simulation details in Supplemental Information). The parameters for X-band (9.4 GHz) CW EPR are temperature, 10 K; microwave power, 0.1 mW; modulation amplitude, 0.5 mT.

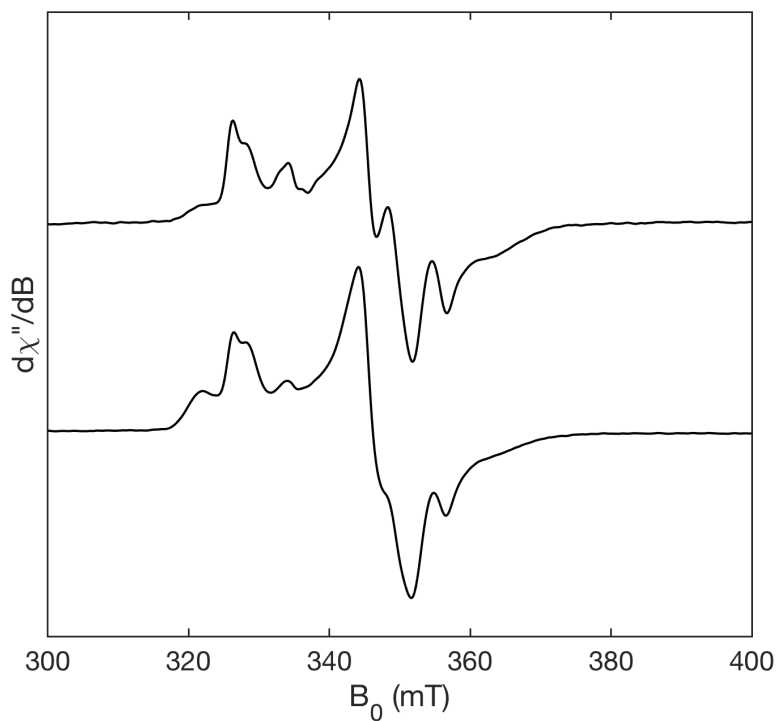


**Figure 2.6.6.** X-band (9.4 GHz) CW EPR of HydG after turnover for (Top) 20 min and (Bottom) 60 min with DTH, SAM, and L-Tyr. The parameters for X-band (9.4 GHz) CW EPR are temperature, 10 K; microwave power, 0.1 mW; modulation amplitude, 0.5 mT.

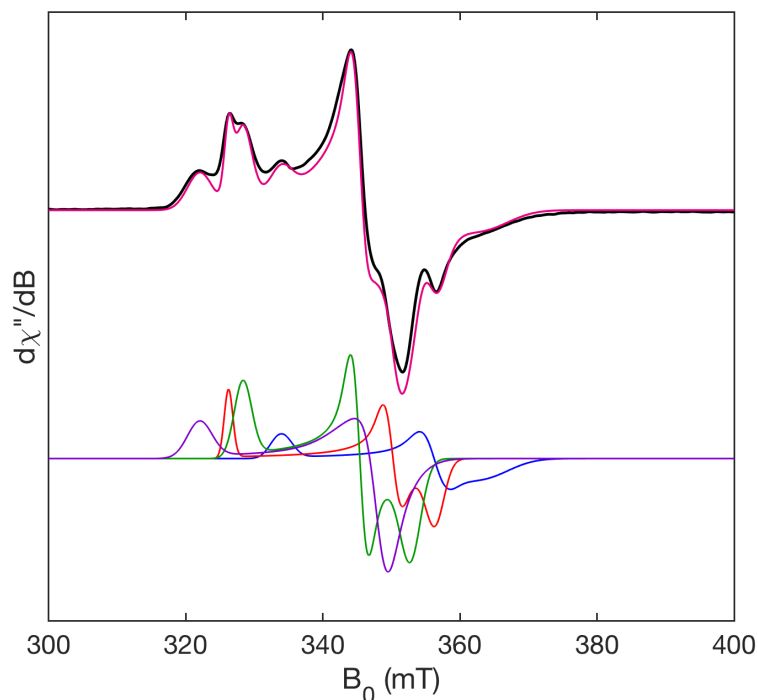


**Figure 2.6.7.** Top: CW EPR of HydG after turnover for 60 min with DTH, SAM, and L-Tyr (black trace), and total simulation (magenta trace). Bottom: simulations of the top black trace with four species SAM-bound  $[4\text{Fe-4S}]_{\text{RS}}^+$  cluster  $g = [2.009 \ 1.882 \ 1.843]$  (16%, blue trace), unknown structure  $g = [2.044 \ 1.943 \ 1.902]$  (34%, green trace), Complex A  $g = [2.057 \ 1.917 \ 1.883]$  (20%, red trace), and cyanide-bound  $[4\text{Fe-4S}]_{\text{aux}}^+$  cluster  $g = [2.084 \ 1.926 \ 1.925]$  (30%, purple trace) (Full simulation details in Supplemental Information). The parameters for X-band (9.4 GHz) CW EPR are temperature, 10 K; microwave power, 0.1 mW; modulation amplitude, 0.5 mT.

### 2.6.1 Regenerating Resting State HydG with L-Cysteine

To examine the ability for the enzyme to regenerate back to the resting state, turnover was performed in the presence of L-Cysteine (L-Cys). Enzymatic turnover up to 60 minutes in the presence of L-Cys results in an EPR spectrum which lacks the axial signal at  $g = 2.084$ , the signal associated with the cyanide-bound  $[4\text{Fe-4S}]_{\text{aux}}^+$  cluster (**Figure 2.6.1.1**). Instead, the spectrum displays a strong signal at  $g = 2.057$ , a peak typically characteristic of Complex A. Though if the enzyme is poised in the resting state with L-Cys bound at the auxiliary cluster and lacks the high spin Fe(II) ion, the EPR signal produced will be nearly identical to that for Complex A. To examine if the resulting signal is primarily a result of Complex A or a resting state enzyme lacking the “dangler” high spin Fe(II) ion, the enzyme was incubated in the presence of excess DTH, SAM,  $1\text{-}^{13}\text{C-L-Tyr}$ , and  $3\text{-}^{13}\text{C-L-Cys}$ , allowed to turnover for 60 min and then frozen to be examined by Mims ENDOR (**Figure 2.6.1.2**). Results from Mims ENDOR indicate the presence of hyperfine from the intermediate Complex A and L-Cys bound to the Auxiliary cluster. Hyperfine from both  $^{13}\text{C}$  atoms, on CO and on L-Cys are observed (**Figure 2.6.1.3**).<sup>50</sup> This experiment demonstrates that after 60 min with the mixture of substrate and cofactor, but lacking additional Fe, the resulting enzyme exists in a mixture of species which includes intermediate Complex A and an enzyme that has fully regenerated to the resting state that lacks the “dangler” Fe.

In a final set of experiments HydG was allowed to turn over for 60 min, then a sub stoichiometric amount of L-Cys was added and frozen at time periods after addition. In comparison to a control sample, EPR samples frozen after 20 and 60 s after L-Cys was added show an incremental decrease in the signal at  $g = 2.083$  and an overall loss in EPR intensity (**Figure 2.6.1.4**). An interesting observation from this experiment is that the EPR signal



associated with L-Cys lacking the “dangler” Fe at  $g = 2.057$  does not immediately grow in. Possibilities for this result could be that the  $[4\text{Fe-4S}]_{\text{aux}}$  cluster is not immediately in a reduced state, but instead undergoes oxidation as cyanide is released. Further studies are needed to determine the exact fate of the cyanide ligand that is released from the enzyme upon turnover with L-Cys.

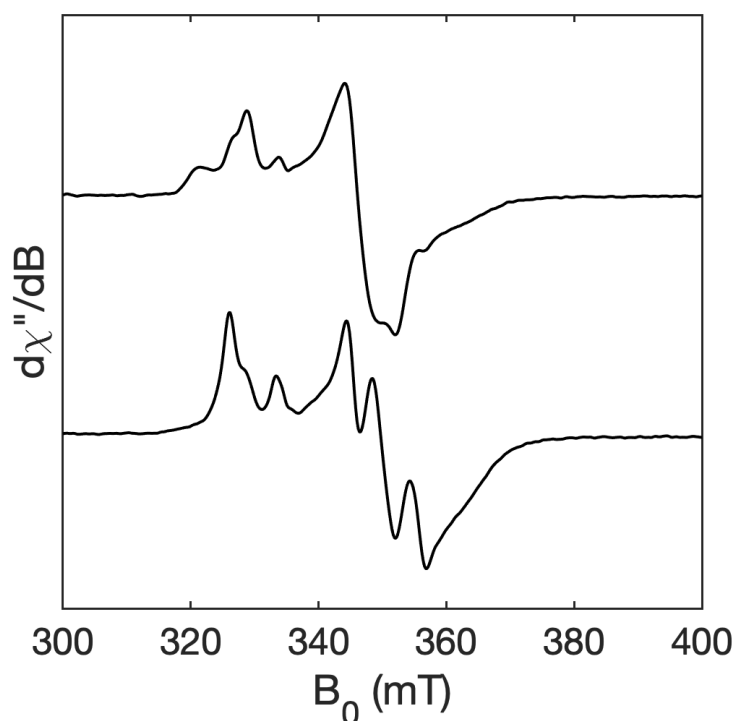


**Figure 2.6.1.1.** X-band (9.4 GHz) CW EPR of HydG after turnover for (Top) 60 min with DTH, SAM, and L-Tyr and (Bottom) with DTH, SAM, L-Tyr, and L-Cys. The parameters for X-band (9.4 GHz) CW EPR are temperature, 10 K; microwave power, 0.1 mW; modulation amplitude, 0.5 mT.

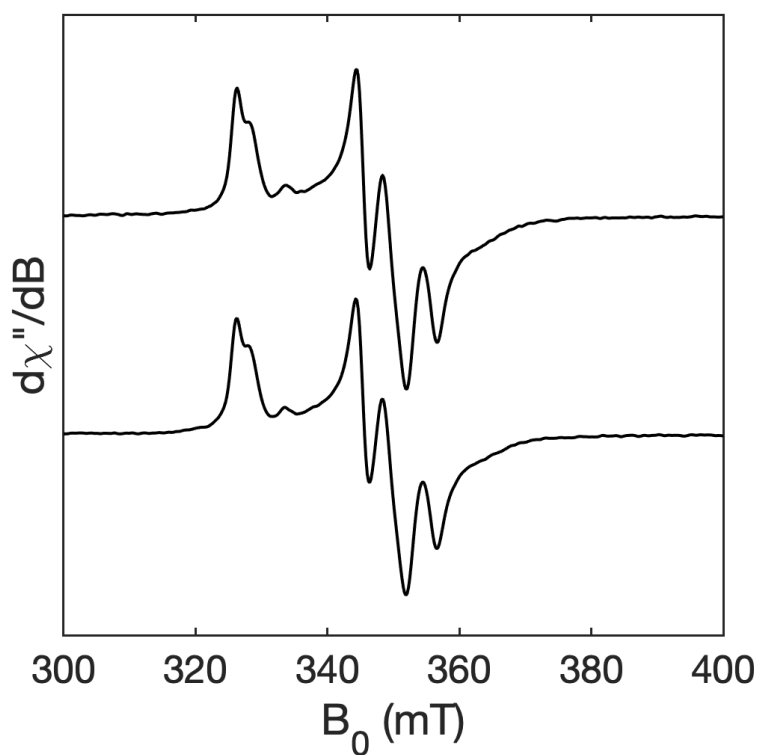


**Figure 2.6.1.2.** X-band (9.4 GHz) CW EPR of HydG after turnover for (Top) 60 min with DTH, SAM, L-Tyr, and 3-<sup>13</sup>C-L-Cys and (Bottom) with DTH, SAM, 1-<sup>13</sup>C-L-Tyr, and 3-<sup>13</sup>C-L-Cys. The parameters for X-band (9.4 GHz) CW EPR are temperature, 10 K; microwave power, 0.1 mW; modulation amplitude, 0.5 mT.

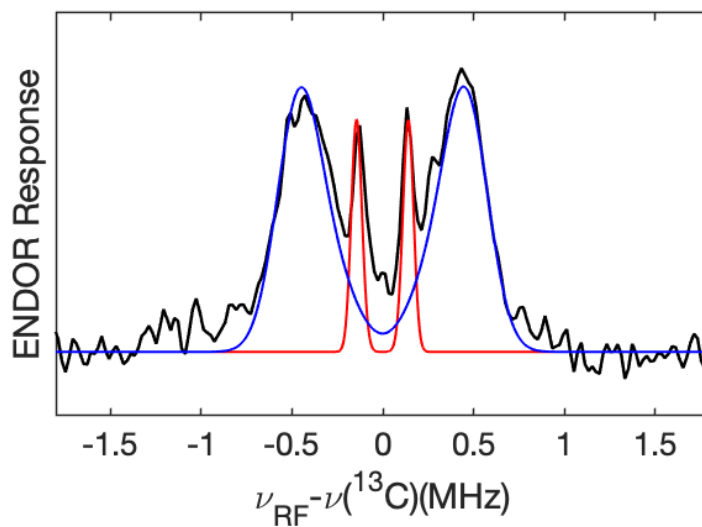


**Figure 2.6.1.3.** Field-dependent  $^{13}\text{C}$  Mims-ENDOR spectra of the HydG reaction mixture generated by using  $1\text{-}^{13}\text{C}$ -Tyr (red trace) +  $3\text{-}^{13}\text{C}$ -Cys (blue trace). The parameters for the simulations are  $g = [2.058, 1.922, 1.881]$ ;  $A = [0.20, 0.31, 0.28]$  MHz, Euler angle,  $[0, 30, 0]^\circ$  (red trace).  $A = [1.00, 0.20, 1.00]$  MHz; Euler angle,  $[60, 35, 60]^\circ$  (blue trace). The parameters for Mims-ENDOR are temperature, 10 K;  $\pi/2$ , 12 ns;  $\tau$ , 300 ns; radio frequency pulse, 30  $\mu\text{s}$ .

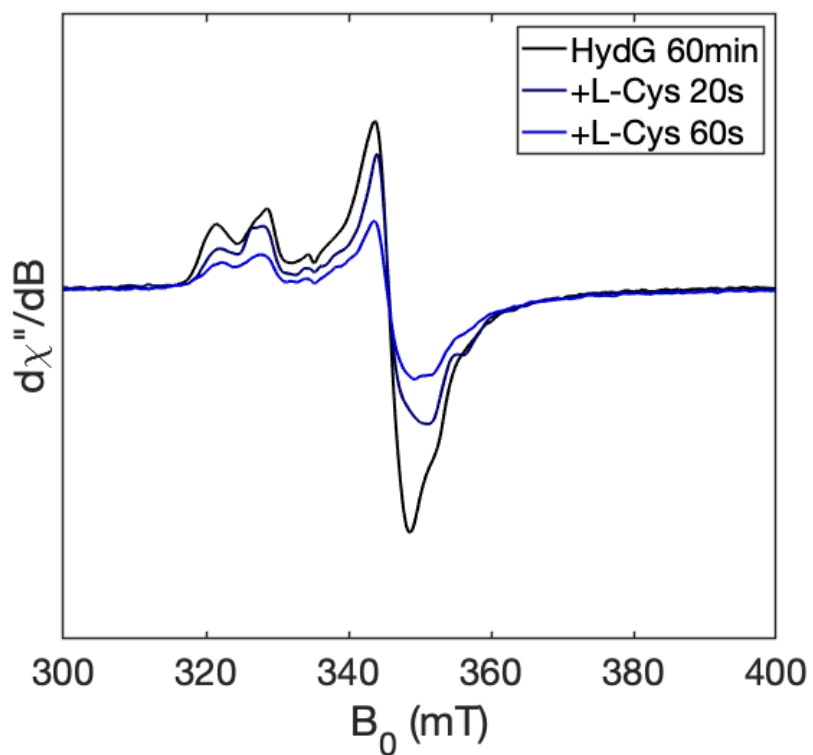


**Figure 2.6.1.4.** X-band (9.4 GHz) CW EPR of HydG after turnover for 60 min (black trace) with DTH, SAM, L-Tyr, then L-Cys added and frozen after 20 s (navy trace) and 60 s (blue trace). The parameters for X-band (9.4 GHz) CW EPR are temperature, 10 K; microwave power, 0.1 mW; modulation amplitude, 0.5 mT.

## 2.7. HydG Mutants Y97F & R327K

The binding pocket for HydG is structured to coordinate L-Tyr in the vicinity of SAM and the  $[4\text{Fe-4S}]_{\text{RS}}$  cluster for efficient catalytic turnover. Among the conserved residues in the binding pocket across lyase enzymes are an L-Arg that coordinates to the carboxylic end of the amino acid and a L-Tyr that coordinates to the substrate amine (**Figure 2.7.1**). To examine these residues effect on catalysis and to potentially allow for binding of non-natural substrates, a “bump and hole” approach was pursued by mutating the two highly conserved amino acid residues Arginine-327 and Tyrosine-97. Mutating these residues can potentially remove any electrostatic or steric interference that may inhibit specific non-natural substrates from binding near the active site  $[4\text{Fe-4S}]_{\text{RS}}$  cluster.

The specific mutations that were undertaken here were arginine to lysine (R327K) and tyrosine to phenylalanine (Y97F). The mutation R327K retains the same charge but removes additional steric hinderance from the larger R-side chain on arginine. The second mutation Y97F, changes the polarization at the binding pocket and slightly removes steric hinderance of the hydroxyl group. These two changes could open the door to non-natural substrates that may otherwise not bind at the active site.

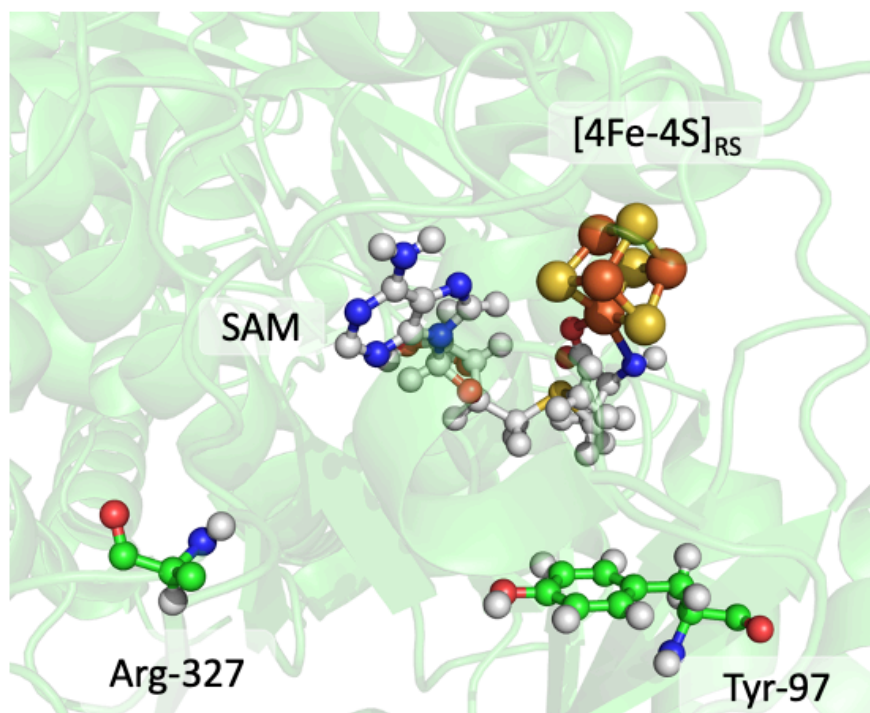


**Figure 2.7.1.** Crystal structure of *TiHydG* (PDB:4WCX) showing SAM bound to the [4Fe-4S]<sub>RS</sub> cluster. pdb: 4WCX

### 2.7.1. Preparing Site Specific Mutations

HydG<sup>R327K</sup> and HydG<sup>Y97F</sup> mutants were generated using the QuikChange Lightning (Agilent) site-directed mutagenesis kit. Sequencing was performed at the UC Davis, UC DNA sequencing facility.

[FeFe]-hydrogenase H-cluster radical SAM maturase HydG [*Shewanella oneidensis*] sequence:

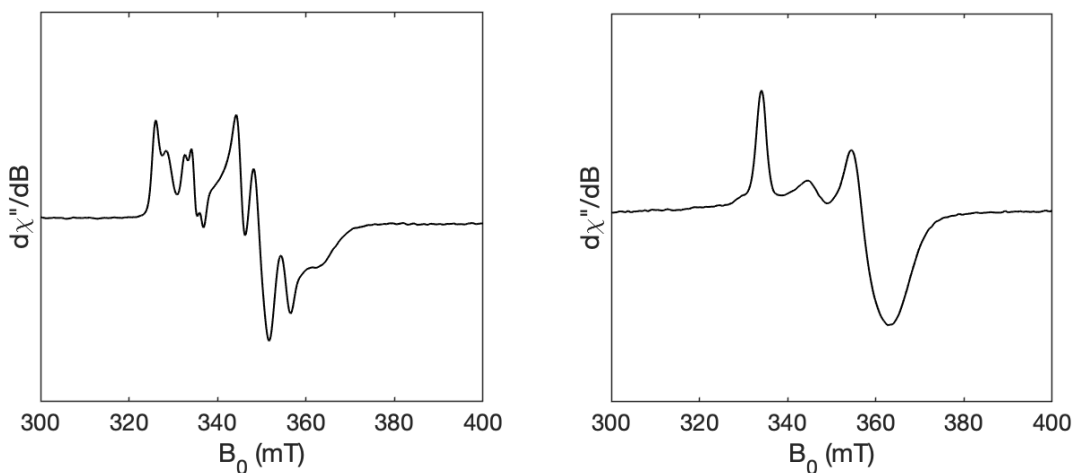
```
1      msthehsit vsdynpnvsf iddqaiwqai edashpsrdq iqailekarq ceglsireta
61     llqnqdkal dealfavare ikntiygnri vmfaplyvsn hcanscsycg fnadnhelkr
121    ktlkqdeirq evtileemgh krilavygeh prnnvqaive siqtmysvkq gkggeirrin
181    vncapmsved fkqlktaaig tyqcfqetyh qdtyskvhlk gkktdylyrl yamhrameag
241    iddvigigalf glydhrfell amlthvqqle kdcgigphti sfpripahg salsekppye
301    vddecfkri vaitrlavpyt glimstrena alrkellelg vsqisagsrt apggyqdskl
361    nqhdaeqfsl gdhramdeii yelvtldsai psfctgcyrk grtgdhfmgl akqqfigkfc
421    qpnalitfre ylndyasdkt reagnalier elakmspsre rnvrscclkp mrvngisiyk
```

### 2.7.2. Results of Site-Specific Mutations on Catalytic Turnover

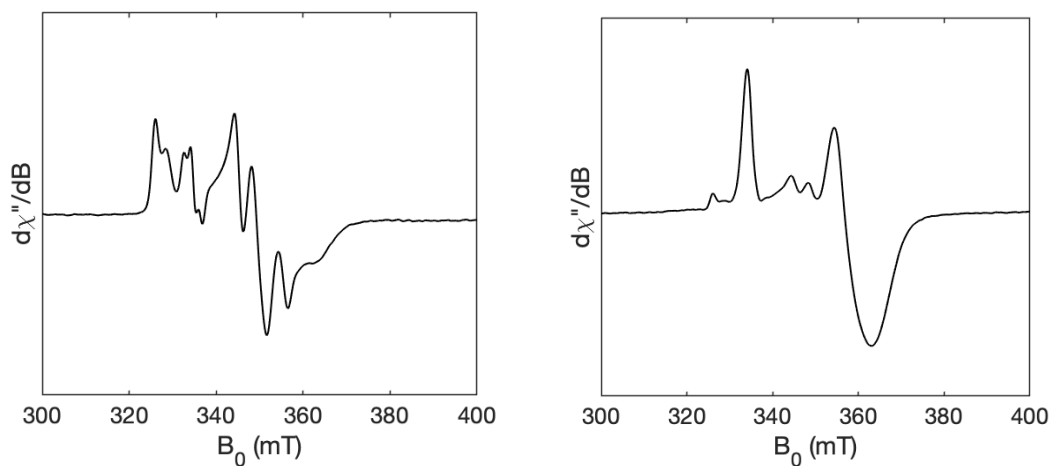
The mutants HydG<sup>R327K</sup> and HydG<sup>Y97F</sup> were first examined for their ability to turnover in the presence of the natural substrate L-Tyr. HydG<sup>R327K</sup> showed no signs of turning over in comparison to wild type enzyme (**Figure 2.7.2.1**). This may be due to the mutant enzyme lacking the “dangler” high spin Fe(II), and being incapable of forming the intermediate Complex A or an inability to bind L-Tyr. Because the mutant did show the resting state  $S = 5/2$  signal, it is likely then that this mutant is unable to bind the natural substrate L-Tyr. The contact formed by L-Arg may also play an important role in triggering the beginning of catalytic turnover. The mutant HydG<sup>Y97F</sup> on the other hand, displayed a small amount of activity with a weak signal at g

= 2.057 (**Figure 2.7.2.2**). This signal at  $g = 2.057$ , a sign of the formation of Complex A, is much smaller in comparison to HydG<sup>wt</sup>. To determine if the overall kinetics had been impeded, EPR spectra at longer time points were recorded. These spectra show an increase in the signal of Complex A at  $g = 2.06$  and a further decrease of the SAM-bound [4Fe-4S] cluster signal seen at  $g = 2.01$  (**Figure 2.7.2.3**). This indicates that the mutation of tyrosine to phenylalanine impedes the ability for L-Tyr to bind but does not completely abolish catalytic activity. The remainder of the protein in HydG<sup>Y97F</sup> mutant is still capable of functioning as normal.

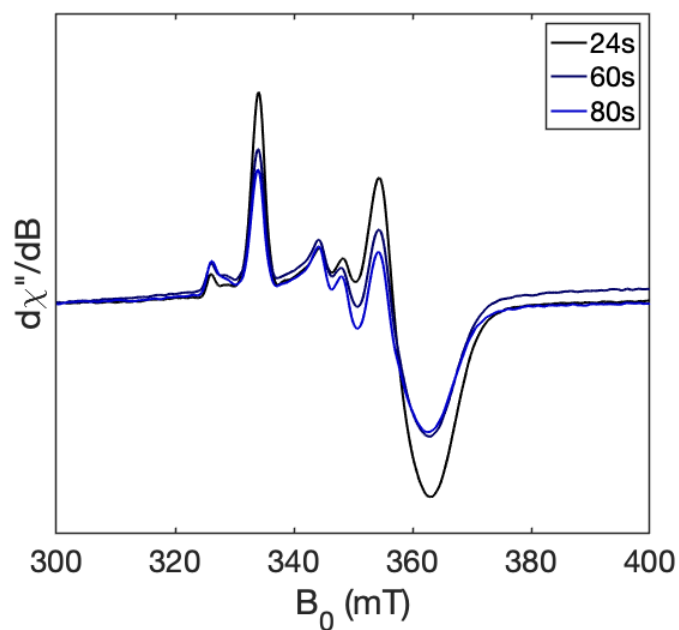




**Figure 2.7.2.1.** X-band (9.4 GHz) CW EPR of *SoHydG* after turnover for (Left) 24s and *HydG<sup>R327K</sup>* (Right) 24 s with DTH, SAM, and L-Tyr. The parameters for X-band (9.4 GHz) CW EPR are temperature, 10 K; microwave power, 0.1 mW; modulation amplitude, 0.5 mT.



**Figure 2.7.2.2.** X-band (9.4 GHz) CW EPR of *SoHydG* after turnover for (Left) 24s and *HydG<sup>Y97F</sup>* (Right) 24 s with DTH, SAM, and L-Tyr. The parameters for X-band (9.4 GHz) CW EPR are temperature, 10 K; microwave power, 0.1 mW; modulation amplitude, 0.5 mT.

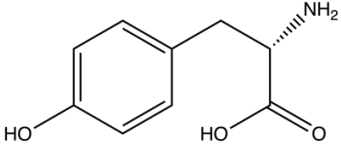
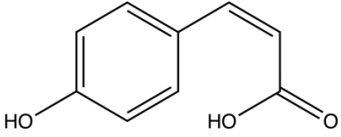
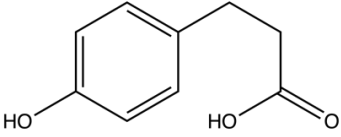
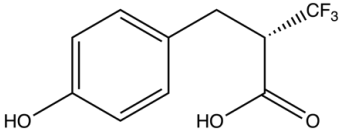
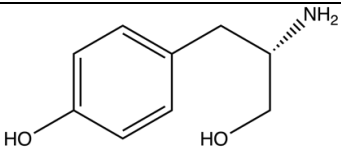


**Figure 2.7.2.3.** X-band (9.4 GHz) CW EPR of HydG<sup>Y97F</sup> after turnover for 24s (black trace), 60s (navy trace), and 80s (blue trace) with DTH, SAM, and L-Tyr. The parameters for X-band (9.4 GHz) CW EPR are temperature, 10 K; microwave power, 0.1 mW; modulation amplitude, 0.5 mT.

### 2.7.3 HydG<sup>R327K</sup> and HydG<sup>Y97F</sup> with Non-natural Substrates

To determine if non-natural substrates could trigger SAM cleavage inside of the HydG mutants, the following substrates were tested in the presence of DTH and SAM.

**Table 2.7.3.1.** Non-natural substrates and catalytic activity

Substrate	Structure	Y97FSoHydG <sup>Y97F</sup>	R327KSoHydG
L-Tyrosine		Yes	No
<i>Cis</i> -p-coumaric acid		No	No
4-hydroxyphenyl propionic acid (HPPA)		No	No
(S)-3,3,3-trifluoro-2-(4-hydroxybenzyl) propanoic acid		No	No
L-Tyrosinol		No	No

Results show that none of the alternative substrates were capable of catalytically activating the mutant HydG<sup>R327K</sup>, including 4-hydroxyphenyl propionic acid and *Cis*-P-coumaric acid which are capable of activating HydG<sup>wt</sup>. This emphasizes the importance of the conserved arginine amino acid residue in enzyme activation. The results with the mutant HydG<sup>Y97F</sup> show

that Tyrosine-97 is necessary to bind substrates with a carboxylic acid end group, and possibly in triggering the enzyme to cleave SAM. While the mutant HydG<sup>Y97F</sup> had a small amount of activity towards natural substrate, it surprisingly did not show any activity to the non-natural substrates tested. *Cis*-p-coumaric acid and 4-hydroxyphenyl propionic acid also did not show any catalytic activity. This demonstrates that the hydrogen bonding network has likely been disrupted by this mutation, preventing proper activation of the enzyme. The natural substrate L-Tyr to a small extent must be able to maintain or restore this hydrogen bonding network through the substrate amine group. Future experiments to test these observations would involve using non-natural substrates that retain the hydrogen bonding nature of the amine group.

## 2.8. References

1. Landgraf, B. J.; McCarthy, E. L.; Booker, S. J., Radical S-Adenosylmethionine Enzymes in Human Health and Disease. *Annu Rev Biochem* **2016**, *85*, 485-514.
2. Broderick, J. B.; Duffus, B. R.; Duschene, K. S.; Shepard, E. M., Radical S-Adenosylmethionine Enzymes. *Chem Rev* **2014**, *114* (8), 4229-4317.
3. Sofia, H. J.; Chen, G.; Hetzler, B. G.; Reyes-Spindola, J. F.; Miller, N. E., Radical SAM, a novel protein superfamily linking unresolved steps in familiar biosynthetic pathways with radical mechanisms: functional characterization using new analysis and information visualization methods. *Nucleic Acids Res* **2001**, *29* (5), 1097-1106.
4. Holliday, G. L.; Akiva, E.; Meng, E. C.; Brown, S. D.; Calhoun, S.; Pieper, U.; Sali, A.; Booker, S. J.; Babbitt, P. C., Atlas of the Radical SAM Superfamily: Divergent Evolution of Function Using a "Plug and Play" Domain. *Radical Sam Enzymes* **2018**, *606*, 1-71.
5. Roje, S., S-Adenosyl-L-methionine: Beyond the universal methyl group donor. *Phytochemistry* **2006**, *67* (15), 1686-1698.
6. Walsby, C. J.; Hong, W.; Broderick, W. E.; Cheek, J.; Ortillo, D.; Broderick, J. B.; Hoffman, B. M., Electron-nuclear double resonance spectroscopic evidence that S-adenosylmethionine binds in contact with the catalytically active [4Fe-4S](+) cluster of pyruvate formate-lyase activating enzyme. *J Am Chem Soc* **2002**, *124* (12), 3143-3151.
7. Henshaw, T. F.; Cheek, J.; Broderick, J. B., The [4Fe-4S](1+) cluster of pyruvate formate-lyase activating enzyme generates the glycy radical on pyruvate formate-lyase: EPR-detected single turnover. *J Am Chem Soc* **2000**, *122* (34), 8331-8332.
8. Broderick, J. B., BIOCHEMISTRY A radically different enzyme. *Nature* **2010**, *465* (7300), 877-878.
9. Yang, H.; McDaniel, E. C.; Impano, S.; Byer, A. S.; Jodts, R. J.; Yokoyama, K.; Broderick, W. E.; Broderick, J. B.; Hoffman, B. M., The Elusive 5'-Deoxyadenosyl Radical: Captured and Characterized by Electron Paramagnetic Resonance and Electron Nuclear Double Resonance Spectroscopies. *J Am Chem Soc* **2019**, *141* (30), 12139-12146.
10. Saylor, R. I.; Stich, T. A.; Joshi, S.; Cooper, N.; Shaw, J. T.; Begley, T. P.; Tantillo, D. J.; Britt, R. D., Trapping and Electron Paramagnetic Resonance Characterization of the 5'

dAdo(center dot) Radical in a Radical S-Adenosyl Methionine Enzyme Reaction with a Non-Native Substrate. *Acs Central Sci* **2019**, *5* (11), 1777-1785.

11. Vignais, P. M.; Billoud, B., Occurrence, classification, and biological function of hydrogenases: An overview. *Chem Rev* **2007**, *107* (10), 4206-4272.
12. Lubitz, W.; Reijerse, E.; van Gastel, M., [NiFe] and [FeFe] hydrogenases studied by advanced magnetic resonance techniques. *Chem Rev* **2007**, *107* (10), 4331-4365.
13. Barber, J.; Tran, P. D., From natural to artificial photosynthesis. *J R Soc Interface* **2013**, *10* (81).
14. Peters, J. W.; Lanzilotta, W. N.; Lemon, B. J.; Seefeldt, L. C., X-ray crystal structure of the Fe-only hydrogenase (Cpl) from *Clostridium pasteurianum* to 1.8 angstrom resolution. *Science* **1998**, *282* (5395), 1853-1858.
15. Nicolet, Y.; Piras, C.; Legrand, P.; Hatchikian, C. E.; Fontecilla-Camps, J. C., *Desulfovibrio desulfuricans* iron hydrogenase: the structure shows unusual coordination to an active site Fe binuclear center. *Structure* **1999**, *7* (1), 13-23.
16. Schilter, D.; Camara, J. M.; Huynh, M. T.; Hammes-Schiffer, S.; Rauchfuss, T. B., Hydrogenase Enzymes and Their Synthetic Models: The Role of Metal Hydrides. *Chem Rev* **2016**, *116* (15), 8693-8749.
17. Moss, D.; Nabedryk, E.; Breton, J.; Mantele, W., Redox-Linked Conformational-Changes in Proteins Detected by a Combination of Infrared-Spectroscopy and Protein Electrochemistry - Evaluation of the Technique with Cytochrome-C. *Eur J Biochem* **1990**, *187* (3), 565-572.
18. Silakov, A.; Kamp, C.; Reijerse, E.; Happe, T.; Lubitz, W., Spectroelectrochemical Characterization of the Active Site of the [FeFe] Hydrogenase HydA1 from *Chlamydomonas reinhardtii*. *Biochemistry-Us* **2009**, *48* (33), 7780-7786.
19. Adamska, A.; Silakov, A.; Lambert, C.; Rudiger, O.; Happe, T.; Reijerse, E.; Lubitz, W., Identification and Characterization of the "Super-Reduced" State of the H-Cluster in [FeFe] Hydrogenase: A New Building Block for the Catalytic Cycle? *Angew Chem Int Edit* **2012**, *51* (46), 11458-11462.
20. Lubitz, W.; Ogata, H.; Rudiger, O.; Reijerse, E., Hydrogenases. *Chem Rev* **2014**, *114* (8), 4081-4148.

21. Mulder, D. W.; Ratzloff, M. W.; Bruschi, M.; Greco, C.; Koonce, E.; Peters, J. W.; King, P. W., Investigations on the Role of Proton-Coupled Electron Transfer in Hydrogen Activation by [FeFe]-Hydrogenase. *J Am Chem Soc* **2014**, *136* (43), 15394-15402.
22. Lubitz, W.; Reijerse, E. J.; Messinger, J., Solar water-splitting into H<sub>2</sub> and O<sub>2</sub>: design principles of photosystem II and hydrogenases. *Energ Environ Sci* **2008**, *1* (1), 15-31.
23. Fan, H. J.; Hall, M. B., A capable bridging ligand for Fe-only hydrogenase: Density functional calculations of a low-energy route for heterolytic cleavage and formation of dihydrogen. *J Am Chem Soc* **2001**, *123* (16), 3828-3829.
24. Zhao, X.; Georgakaki, I. P.; Miller, M. L.; Mejia-Rodriguez, R.; Chiang, C. Y.; Darensbourg, M. Y., Catalysis of H<sub>2</sub>/D<sub>2</sub> scrambling and other H/D exchange processes by [Fe]-hydrogenase model complexes. *Inorg Chem* **2002**, *41* (15), 3917-3928.
25. Zhao, X.; Chiang, C. Y.; Miller, M. L.; Rampersad, M. V.; Darensbourg, M. Y., Activation of alkenes and H<sub>2</sub> by [Fe]-H(2)ase model complexes. *J Am Chem Soc* **2003**, *125* (2), 518-524.
26. Bruschi, M.; Fantucci, P.; De Gioia, L., Density functional theory investigation of the active site of Fe-hydrogenases. Systematic study of the effects of redox state and ligands hardness on structural and electronic properties of complexes related to the [2Fe](H) subcluster. *Inorg Chem* **2004**, *43* (12), 3733-3741.
27. van der Vlugt, J. I.; Rauchfuss, T. B.; Whaley, C. M.; Wilson, S. R., Characterization of a diferrous terminal hydride mechanistically relevant to the Fe-only hydrogenases. *J Am Chem Soc* **2005**, *127* (46), 16012-16013.
28. Zampella, G.; Greco, C.; Fantucci, P.; De Gioia, L., Proton reduction and dihydrogen oxidation on models of the [2Fe](H) cluster of [Fe] hydrogenases. A density functional theory investigation. *Inorg Chem* **2006**, *45* (10), 4109-4118.
29. Ezzaher, S.; Capon, J. F.; Gloaguen, F.; Petillon, F. Y.; Schollhammer, P.; Talarmin, J., Evidence for the formation of terminal hydrides by protonation of an asymmetric iron hydrogenase active site mimic. *Inorg Chem* **2007**, *46* (9), 3426-3428.
30. Cammack, R., Bioinorganic chemistry - Hydrogenase sophistication. *Nature* **1999**, *397* (6716), 214-215.

31. Posewitz, M. C.; King, P. W.; Smolinski, S. L.; Zhang, L. P.; Seibert, M.; Ghirardi, M. L., Discovery of two novel radical S-adenosylmethionine proteins required for the assembly of an active [Fe] hydrogenase. *J Biol Chem* **2004**, *279* (24), 25711-25720.
32. Kuchenreuther, J. M.; George, S. J.; Grady-Smith, C. S.; Cramer, S. P.; Swartz, J. R., Cell-free H-cluster Synthesis and [FeFe] Hydrogenase Activation: All Five CO and CN- Ligands Derive from Tyrosine. *Plos One* **2011**, *6* (5).
33. Pagnier, A.; Balci, B.; Shepard, E. M.; Yang, H.; Warui, D. M.; Impano, S.; Booker, S. J.; Hoffman, B. M.; Broderick, W. E.; Broderick, J. B., [FeFe]-Hydrogenase: Defined Lysate-Free Maturation Reveals a Key Role for Lipoyl-H-Protein in DTMA Ligand Biosynthesis. *Angew Chem Int Edit* **2022**.
34. Britt, R. D.; Tao, L.; Rao, G.; Chen, N.; Wang, L. P., Proposed Mechanism for the Biosynthesis of the [FeFe] Hydrogenase H-Cluster: Central Roles for the Radical SAM Enzymes HydG and HydE. *ACS Bio Med Chem Au* **2022**, *2* (1), 11-21.
35. Mulder, D. W.; Boyd, E. S.; Sarma, R.; Lange, R. K.; Endrizzi, J. A.; Broderick, J. B.; Peters, J. W., Stepwise [FeFe]-hydrogenase H-cluster assembly revealed in the structure of HydA(Delta EFG). *Nature* **2010**, *465* (7295), 248-U143.
36. McGlynn, S. E.; Ruebush, S. S.; Naumov, A.; Nagy, L. E.; Dubini, A.; King, P. W.; Broderick, J. B.; Posewitz, M. C.; Peters, J. W., In vitro activation of [FeFe] hydrogenase: new insights into hydrogenase maturation. *J Biol Inorg Chem* **2007**, *12* (4), 443-447.
37. Kuchenreuther, J. M.; Britt, R. D.; Swartz, J. R., New Insights into [FeFe] Hydrogenase Activation and Maturase Function. *Plos One* **2012**, *7* (9).
38. Berggren, G.; Adamska, A.; Lambertz, C.; Simmons, T. R.; Esselborn, J.; Atta, M.; Gambarelli, S.; Mouesca, J. M.; Reijerse, E.; Lubitz, W.; Happe, T.; Artero, V.; Fontecave, M., Biomimetic assembly and activation of [FeFe]-hydrogenases. *Nature* **2013**, *499* (7456), 66-+.
39. Esselborn, J.; Lambertz, C.; Adamska-Venkatesh, A.; Simmons', T.; Berggren, G.; Nothl, J.; Siebel, J.; Hemschemeier, A.; Artero, V.; Reijerse, E.; Fontecave, M.; Lubitz, W.; Happe, T., Spontaneous activation of [FeFe]-hydrogenases by an inorganic [2Fe] active site mimic. *Nat Chem Biol* **2013**, *9* (10), 607-609.



40. Pilet, E.; Nicolet, Y.; Mathevon, C.; Douki, T.; Fontecilla-Camps, J. C.; Fontecave, M., The role of the maturase HydG in [FeFe]-hydrogenase active site synthesis and assembly. *Febs Lett* **2009**, *583* (3), 506-511.
41. Kriek, M.; Martins, F.; Challand, M. R.; Croft, A.; Roach, P. L., Thiamine biosynthesis in *Escherichia coli*: Identification of the intermediate and by-product derived from tyrosine. *Angew Chem Int Edit* **2007**, *46* (48), 9223-9226.
42. Shepard, E. M.; Duffus, B. R.; George, S. J.; McGlynn, S. E.; Challand, M. R.; Swanson, K. D.; Roach, P. L.; Cramer, S. P.; Peters, J. W.; Broderick, J. B., [FeFe]-Hydrogenase Maturation: HydG-Catalyzed Synthesis of Carbon Monoxide. *J Am Chem Soc* **2010**, *132* (27), 9247-9249.
43. Shepard, E. M.; Mus, F.; Betz, J. N.; Byer, A. S.; Duffus, B. R.; Peters, J. W.; Broderick, J. B., [FeFe]-Hydrogenase Maturation (vol 53, pg 4090, 2014). *Biochemistry-Us* **2014**, *53* (34), 5588-5588.
44. Kuchenreuther, J. M.; Myers, W. K.; Suess, D. L. M.; Stich, T. A.; Pelmeshnikov, V.; Shiigi, S. A.; Cramer, S. P.; Swartz, J. R.; Britt, R. D.; George, S. J., The HydG Enzyme Generates an Fe(CO)(2)(CN) Synthone in Assembly of the FeFe Hydrogenase H-Cluster. *Science* **2014**, *343* (6169), 424-427.
45. Rao, G. D.; Britt, R. D., Electronic Structure of Two Catalytic States of the [FeFe] Hydrogenase H-Cluster As Probed by Pulse Electron Paramagnetic Resonance Spectroscopy. *Inorg Chem* **2018**, *57* (17), 10935-10944.
46. Suess, D. L. M.; Burstel, I.; De La Paz, L.; Kuchenreuther, J. M.; Pham, C. C.; Cramer, S. P.; Swartz, J. R.; Britt, R. D., Cysteine as a ligand platform in the biosynthesis of the FeFe hydrogenase H cluster. *P Natl Acad Sci USA* **2015**, *112* (37), 11455-11460.
47. Kuchenreuther, J. M.; Myers, W. K.; Stich, T. A.; George, S. J.; Nejatjahromy, Y.; Swartz, J. R.; Britt, R. D., A radical intermediate in tyrosine scission to the CO and CN<sup>-</sup> ligands of FeFe hydrogenase. *Science* **2013**, *342* (6157), 472-5.
48. Rao, G. D.; Chen, N. H.; Marchiori, D. A.; Wang, L. P.; Britt, R. D., Accumulation and Pulse Electron Paramagnetic Resonance Spectroscopic Investigation of the 4-Oxidobenzyl Radical Generated in the Radical S-Adenosyl-L-methionine Enzyme HydG. *Biochemistry-Us* **2022**, *61* (2), 107-116.

49. Chen, N. H.; Rao, G. D.; Britt, R. D.; Wang, L. P., Quantum Chemical Study of a Radical Relay Mechanism for the HydG-Catalyzed Synthesis of a Fe(II)(CO)<sub>2</sub>(CN)cysteine Precursor to the H-Cluster of [FeFe] Hydrogenase. *Biochemistry-Us* **2021**, *60* (40), 3016-3026.
50. Rao, G. D.; Tao, L. Z.; Suess, D. L. M.; Britt, R. D., A [4Fe-4S]-Fe(CO)(CN)-L-cysteine intermediate is the first organometallic precursor in [FeFe] hydrogenase H-cluster bioassembly. *Nat Chem* **2018**, *10* (5), 555-560.
51. Rao, G.; Pattenaude, S. A.; Alwan, K.; Blackburn, N. J.; Britt, R. D.; Rauchfuss, T. B., The binuclear cluster of [FeFe] hydrogenase is formed with sulfur donated by cysteine of an [Fe(Cys)(CO)<sub>2</sub>(CN)] organometallic precursor. *P Natl Acad Sci USA* **2019**, *116* (42), 20850-20855.
52. Tao, L. Z.; Pattenaude, S. A.; Joshi, S.; Begley, T. P.; Rauchfuss, T. B.; Britt, R. D., Radical SAM Enzyme HydE Generates Adenosylated Fe(I) Intermediates En Route to the [FeFe]-Hydrogenase Catalytic H-Cluster. *J Am Chem Soc* **2020**, *142* (24), 10841-10848.
53. Rohac, R.; Martin, L.; Liu, L.; Basu, D.; Tao, L. Z.; Britt, R. D.; Rauchfuss, T. B.; Nicolet, Y., Crystal Structure of the [FeFe]-Hydrogenase Maturase HydE Bound to Complex-B. *J Am Chem Soc* **2021**, *143* (22), 8499-8508.
54. Dinis, P.; Suess, D. L. M.; Fox, S. J.; Harmer, J. E.; Driesener, R. C.; De La Paz, L.; Swartz, J. R.; Essex, J. W.; Britt, R. D.; Roach, P. L., X-ray crystallographic and EPR spectroscopic analysis of HydG, a maturase in [FeFe]-hydrogenase H-cluster assembly. *P Natl Acad Sci USA* **2015**, *112* (5), 1362-1367.
55. Suess, D. L. M.; Britt, R. D., EPR Spectroscopic Studies of [FeFe]-Hydrogenase Maturation. *Top Catal* **2015**, *58* (12-13), 699-707.
56. Rao, G. D.; Alwan, K. B.; Blackburn, N. J.; Britt, R. D., Incorporation of Ni<sup>2+</sup>, Co<sup>2+</sup>, and Selenocysteine into the Auxiliary Fe-S Cluster of the Radical SAM Enzyme HydG. *Inorg Chem* **2019**, *58* (19), 12601-12608.
57. Stoll, S.; Schweiger, A., EasySpin, a comprehensive software package for spectral simulation and analysis in EPR. *J Magn Reson* **2006**, *178* (1), 42-55.
58. Blumberg, W. E.; Peisach, J., Measurement of Zero-Field Splitting and Determination of Ligand Composition in Mononuclear Nonheme Iron Proteins. *Ann Ny Acad Sci* **1973**, *222* (Dec31), 539-560.

## Chapter 3

### Characterizing the biosynthesis of the [Fe(II)(CN)(CO)<sub>2</sub>(cysteinate)]<sup>-</sup> organometallic product from fully labeled <sup>57</sup>Fe HydG

#### 3.1. <sup>57</sup>Fe Mössbauer of [FeFe]-hydrogenase and Biomimetic compounds

Hydrogenases, [FeFe], [NiFe] and the [Fe] only form utilize low valent Fe at the active site to perform catalysis (Section 2.2.). Mössbauer spectroscopy of the dinuclear center of [FeFe]-hydrogenase was first accomplished with the organism *Clostridium pasteurianum*.<sup>1</sup> The H<sub>red</sub> state of the enzyme showed a single quadrupole doublet with  $\delta = 0.08 \text{ mm s}^{-1}$ ,  $\Delta E_Q = 0.87 \text{ mm s}^{-1}$  indicating low spin Fe. Mössbauer spectra of the different H-cluster oxidation states were later reported with only minor changes to  $\delta$  and  $\Delta E_Q$ .<sup>2</sup> Table 3.1.1. lists Mössbauer values for the H-cluster in [FeFe]-hydrogenase. Low  $\delta$  values between 0.08 - 0.18 with small  $\Delta E_Q$  values 0.55 - 1.09 are characteristic of the low spin Fe seen in the H-cluster.

**Table 3.1.1. Mössbauer parameters for low spin Fe in the active site of [FeFe]-hydrogenase**

Compounds	$\delta$ , mm s <sup>-1</sup>	$\Delta E_Q$ , mm s <sup>-1</sup>	Ref.
<b>[FeFe]-hydrogenase</b>			
H <sub>red</sub> , <i>Clostridium pasteurianum</i>	0.08	0.87	1
H <sub>red</sub> , <i>Desulfovibrio vulgaris</i>	0.13	0.85	2
H <sub>ox</sub>	0.16	1.09	
H <sub>ox</sub> -CO	0.17, 0.13	0.70, 0.65	
H <sub>ox</sub> -CO, <i>Chlamydomonas reinhardtii</i>	0.16, 0.08	0.89, 0.55	3

In a semisynthetic approach, [<sup>57</sup>Fe<sub>2</sub>(adt)(CN)<sub>2</sub>(CO)<sub>4</sub>]<sup>2-</sup> was synthesized and used to mature an apo-[FeFe]-hydrogenase enzyme from *Chlamydomonas reinhardtii*.<sup>3</sup> The result is a holo-[FeFe]-hydrogenase that is selectively labeled with a [2<sup>57</sup>Fe]<sub>H</sub> subcluster. This enzyme poised in an H<sub>ox</sub>-CO state gave the following Mössbauer values:  $\delta_1 = 0.16 \text{ mm s}^{-1}$ ,  $\delta_2 = 0.08 \text{ mm s}^{-1}$  and

$\Delta E_{Q1} = 0.89 \text{ mm s}^{-1}$ ,  $\Delta E_{Q2} = 0.55 \text{ mm s}^{-1}$ . These results differ slightly from a fully  $^{57}\text{Fe}$  labeled enzyme, likely due the increased accuracy of a selectively labeled experiment over a fully labeled enzyme.

### 3.2. Oxidation states and Spin Dependent delocalization of Iron-Sulfur Clusters

To correctly interpret Mössbauer spectra of Radical SAM maturase enzymes, it is important to understand and review the electronic structure for the various types of Fe-S cluster motifs.<sup>4</sup> Because radial distributions of d and s electrons overlap, isomer shifts  $\delta$  provide a measure of the d electron density and serve as good indicators of oxidation state for Fe (**Section 1.2.3.1**).  $[\text{Fe}_2\text{-S}_2]^+$  clusters exhibit two distinct quadrupole doublets with  $\delta_1 = 0.30 \text{ mm s}^{-1}$  and  $\delta_2 = 0.72 \text{ mm s}^{-1}$ , indicating two valence localized species of  $\text{Fe}^{3+}$  and  $\text{Fe}^{2+}$  respectively. Fe ions in this case antiferromagnetically couple to give an overall  $S = \frac{1}{2}$  (**Figure 3.2.1**). Mössbauer spectra of  $[\text{Fe}_3\text{S}_4]^+$  exhibit one quadrupole doublet  $\delta = 0.27 \text{ mm s}^{-1}$ , indicating three equivalent  $\text{Fe}^{3+}$ . Reduction gives an overall  $S = 2$  state with a Mössbauer spectrum containing a 1:2 ratio of quadrupole doublets. The minor doublet has  $\delta = 0.32 \text{ mm s}^{-1}$  characteristic of  $\text{Fe}^{3+}$  whereas the major doublet has  $\delta = 0.46 \text{ mm s}^{-1}$ , a value halfway between  $\text{Fe}^{2+}$  and  $\text{Fe}^{3+}$  suggesting a valence delocalized pair with an oxidation state of  $\text{Fe}^{2.5+}$ . The overall spin state of  $S = 2$  arises from the antiferromagnetic coupling of the  $\text{Fe}^{3+}$  ( $S = 5/2$ ) to the  $\text{Fe}^{2.5+}$  pair ( $S = 9/2$ ). Spin state delocalization can explain the behavior of the delocalized  $\text{Fe}^{2.5+}$  pair, in which two  $\text{Fe}^{3+}$  ions ferromagnetically align their spins allowing the additional electron to delocalize across the dimer with opposite spin.<sup>5,6</sup>  $[\text{4Fe-4S}]$  clusters can exist in three common oxidation states (**Figure 3.2.1**). In the most oxidized state, the cluster exists as a pair of  $\text{Fe}^{3+}$  ions and a  $\text{Fe}^{2.5+}$  pair. One

electron reduction gives a  $[4\text{Fe-4S}]^{2+}$  cluster composed of two  $\text{Fe}^{2.5+}$  pairs, and reduction by a final electron gives the fully reduced state  $[4\text{Fe-4S}]^+$  containing a  $\text{Fe}^{2.5+}$  pair along with a pair of  $\text{Fe}^{2+}$  ions. NMR studies have shown that the delocalized  $\text{Fe}^{2.5+}$  pair can reside on different  $\text{Fe}_2\text{S}_2$  faces and exists in rapid equilibrium between different forms.<sup>7</sup>

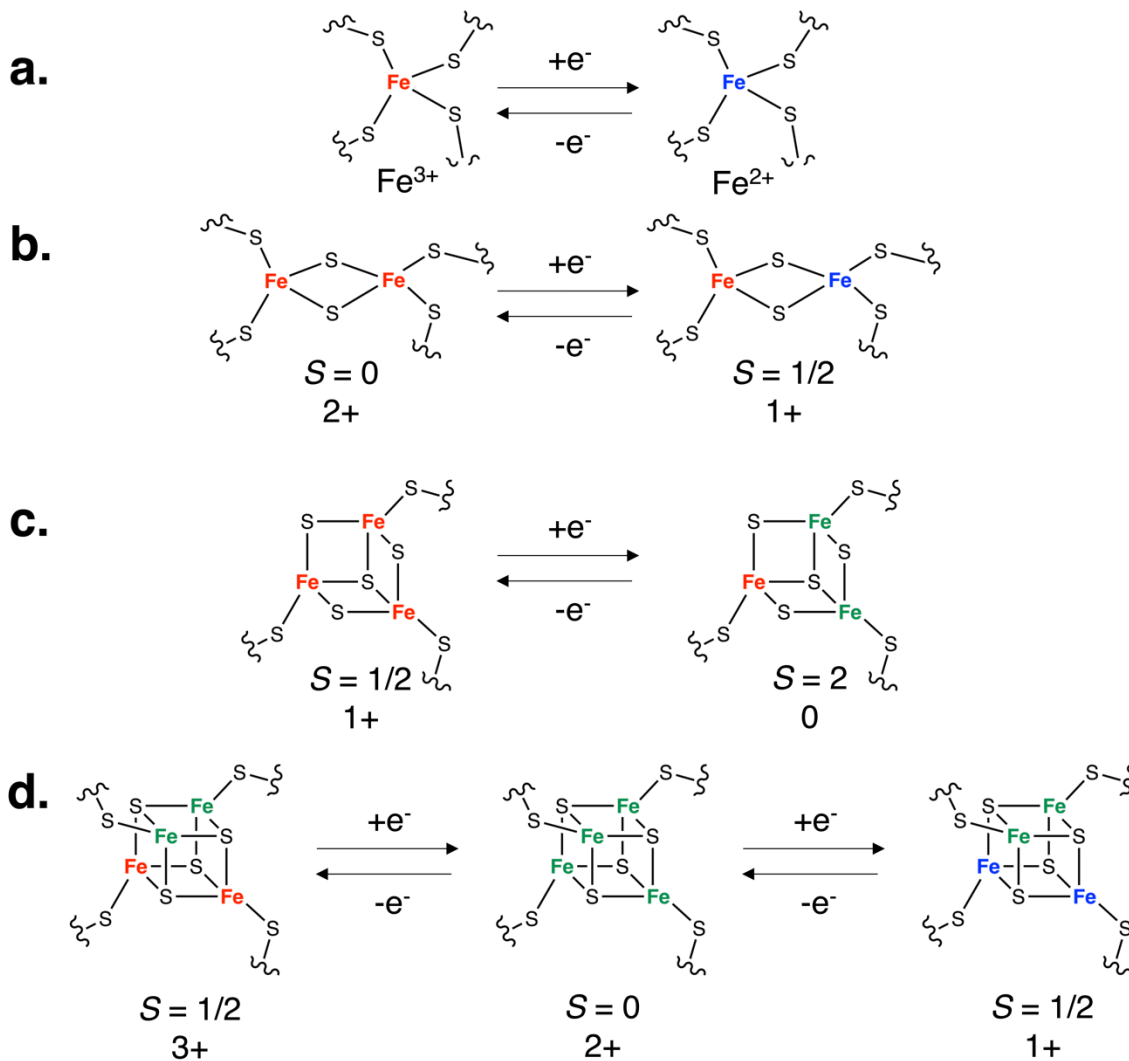


**Figure 3.2.1.** Fe-S clusters showing localized and delocalized oxidation states. Localized  $\text{Fe}^{3+}$  (red), localized  $\text{Fe}^{2+}$  (blue), and delocalized  $\text{Fe}^{2.5+}$  pairs (green).<sup>4</sup>

### 3.3. <sup>57</sup>Fe Mössbauer and EPR Spectroscopy of fully labeled HydG

To pursue observation of diamagnetic, EPR silent intermediate(s) and product from the HydG catalytic cycle we turned to Mössbauer spectroscopy. The first requirement for these experiments is to prepare HydG enzyme containing the <sup>57</sup>Fe isotope. Given the simplicity in experimental design, fully labeled enzyme was chosen to pursue first.

#### 3.3.1. Expression and Purification of <sup>57</sup>Fe HydG

<sup>57</sup>Fe was purchased from Isoflex and had a purity of 95.56%. All additives except for tyrosine were dissolved in 100 mM HEPES buffer (pH = 7.2) with 50 mM KCl and adjusted to pH = 7.5 before use. <sup>57</sup>Fe solution was prepared in a fume hood, using ice baths to chill the reacting solution. To prepare ~50 mL of ~56 mM <sup>57</sup>Fe (final pH of ~5), metallic <sup>57</sup>Fe was dissolved using *aqua regia*. First, 3 mL of nitric acid (> 65%) was added to 100 mg of metallic <sup>57</sup>Fe in a 250 mL Erlenmeyer flask. Next, 4 mL of 12 M hydrochloric acid was added dropwise. After the <sup>57</sup>Fe had completely dissolved, 14 mL of 5 M sodium hydroxide was slowly added for partial neutralization, followed by 5 mL of 1.5 M sodium citrate and 5 mL of 1 M ammonium hydroxide.

<sup>57</sup>Fe fully labeled HydG was prepared by expressing in *E. coli* grown in medium supplemented with ~200 μM <sup>57</sup>Fe instead of natural abundance Fe (as described in **Section 2.3.1.**). Using a colorimetric assay described by Fish<sup>8</sup>, the growth medium prepared from commercial LB Broth Miller (RPI Research Products International) contained < 7 μM natural abundance Fe.

**Fe assay procedure:**

Reagent A: Iron-releasing agent (prepared fresh). 0.6 N HCl, 2.25% (w/v) (0.142 M)  $\text{KMnO}_4$

Reagent B: Reducing, Iron-chelating reagent. 6.5 mM Ferrozine, 13.1 mM neocuprine, 2 M ascorbic acid, 5 M ammonium acetate.

Iron standard: 6  $\mu\text{g}/\text{mL}$  ferrous ethylenediammonium sulfate, 0.01 N HCl.

**Directions:**

0.5 mL of Reagent A was added to 1.0 mL of growth media containing LB broth (20 g/L), MOPs buffer (100 mM, pH = 8.0), glucose (0.50%), kanamycin (40  $\mu\text{g}/\text{L}$ ), and ampicillin (100  $\mu\text{g}/\text{L}$ ). This digestion mixture was incubated for 2 hr at 60°C. Following digestion, 0.1 mL of reagent B was added to each sample and standard solution. The result is a magenta colored Fe(II) [Ferrozine] $_3^{2+}$  complex which can be measured at 562 nm.

The resulting Fe content assay resulted in a value of 6.4 +/- 0.7  $\mu\text{M}$  of natural abundance Fe. The growth media had been enriched with 220  $\mu\text{M}$  of  $^{57}\text{Fe}$  (95.56% purity), resulting in 93.5%  $^{57}\text{Fe}$  enrichment of HydG protein.

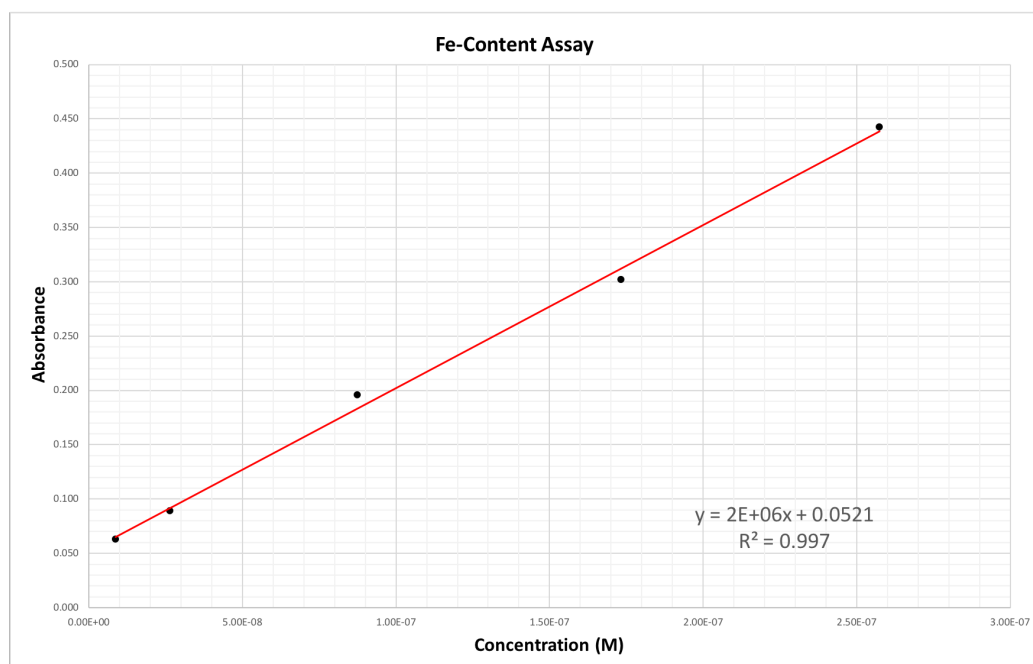


**Figure 3.3.1.1.** Fe Standard Curve

### 3.3.2. Materials and Methods

EPR and Mössbauer samples were prepared as described in **Section 2.4.1**. EPR and Mössbauer samples that were prepared in parallel originated from the same reacting protein solution and were separated into their respective sample holders immediately before freezing in liquid nitrogen simultaneously.

### 3.3.3. Observing the $[\text{Fe(II)(CN)(CO)}_2(\text{cysteinate})]$ product, Complex B, by $^{57}\text{Fe}$ Mössbauer Spectroscopy

Mössbauer experiments were performed to directly observe the formation of Complex B and gain insight into its electronic structure. Fully labeled  $^{57}\text{Fe}$  HydG was prepared by expressing the enzyme in excess soluble  $^{57}\text{Fe}$  as ferric ammonium citrate. EPR analysis of this fully labeled enzyme displays the expected  $^{57}\text{Fe}$  broadening in the SAM-bound  $[\text{4Fe-4S}]_{\text{RS}}$  resting state (**Figure 3.3.3.1**). The  $^{57}\text{Fe}$  Mössbauer spectrum at zero field (**Figure 3.3.3.2 and**



**Figure 3.3.3.3.)** features well-resolved quadrupole doublets for the  $[4\text{Fe-4S}]_{\text{RS}}$  cluster,  $[4\text{Fe-4S}]_{\text{aux}}$  cluster, and the dangler  $\text{Fe}^{2+}$ , which is high spin. These findings are in close agreement with Mössbauer parameters previously published for HydG.<sup>9</sup> Having established that our HydG was fully  $^{57}\text{Fe}$ -labeled, experiments were initiated by the addition of DTH, SAM, and L-Tyr. Samples were frozen at various times and analyzed by Mössbauer and EPR spectroscopy. After 60 min, the EPR spectrum reveals the expected shoulder at  $g = 2.084$ , assigned to the cyanide-bound  $[4\text{Fe-4S}]_{\text{aux}}$  cluster. Concomitantly, the low field  $S = 5/2$  signal associated with  $[4\text{Fe-4S}]_{\text{aux}}$  had diminished (**Figure 3.3.3.1. and Figure 3.3.3.4.**). Directly overlaying the Mössbauer spectra clarifies apparent changes that occur during turnover (**Figure 3.3.3.6.**). Notably the high spin  $\text{Fe}^{2+}$  dangler species has decreased and an increase in gamma ray absorption can be observed at lower velocity, indicating the presence of new Fe species. Also observed was a slight shift in the signals for the  $[4\text{Fe-4S}]_{\text{aux}}$  cluster. This shift may be attributed to the dangler Fe and cysteine molecule now being detached from the  $[4\text{Fe-4S}]_{\text{aux}}$  cluster, and the apical 4<sup>th</sup> Fe is now bound by  $\text{CN}^-$ . The best fit Mössbauer parameters for the cyanide-bound  $[4\text{Fe-4S}]_{\text{aux}}$  cluster are  $\delta_1 = 0.47 \text{ mm s}^{-1}$ ,  $\Delta E_{\text{Q1}} = 1.20 \text{ mm s}^{-1}$  for the  $\text{Fe}^{2.5+}$  pair, and  $\delta_2 = 0.51 \text{ mm s}^{-1}$ ,  $\Delta E_{\text{Q2}} = 1.61 \text{ mm s}^{-1}$  for the  $\text{Fe}^{2+}$  pair. Subtracting the total  $^{57}\text{Fe}$  Mössbauer parameters of resting state HydG, including observed auxiliary cluster and “dangler”  $\text{Fe}^{2+}$  changes, reveals a new Fe species that is apparently generated during turnover (**Figure 3.3.3.7.**). EPR spectroscopy of samples that were prepared in parallel, freeze-quenched at 60 min confirms the presence of Complex B, with no trace of the intermediate Complex A (**Figure 3.3.3.4.**). The new Fe species observed by Mössbauer, can be simulated as a single quadrupole doublet species with the parameters  $\delta = 0.10 \text{ mm s}^{-1}$ ,  $\Delta E_{\text{Q}} = 0.66 \text{ mm s}^{-1}$  (**Figure 3.3.3.7.**), which is taken to be those associated with the  $[\text{Fe(II)(CN)(CO)}_2(\text{cysteinate})]^-$ , Complex B, product.

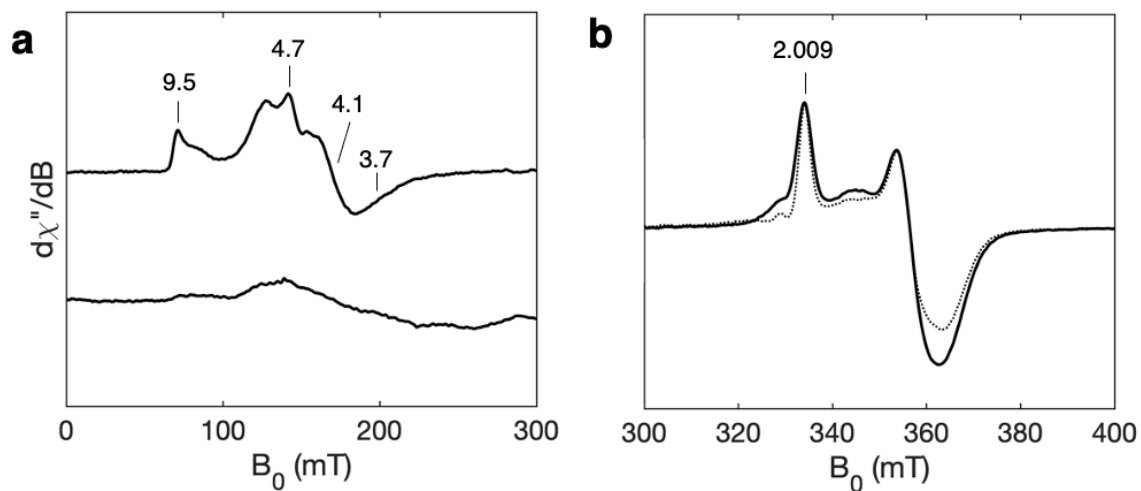


**Figure 3.3.3.1.** **a.** Top: CW EPR of  $^{57}\text{Fe}$  HydG auxiliary cluster. Bottom: CW EPR of  $^{57}\text{Fe}$  HydG auxiliary cluster after turnover for 60 min with DTH, SAM, and L-Tyr. **b.** CW EPR of  $^{57}\text{Fe}$  HydG SAM-bound  $[4\text{Fe-4S}]_{\text{RS}^+}$  cluster (black trace) and natural abundance Fe HydG SAM-bound  $[4\text{Fe-4S}]_{\text{RS}^+}$  (dotted trace). The parameters for X-band (9.4 GHz) CW EPR are temperature, 10 K; microwave power, 5 mW (**a**), 0.1 mW (**b**); modulation amplitude, 0.5 mT.

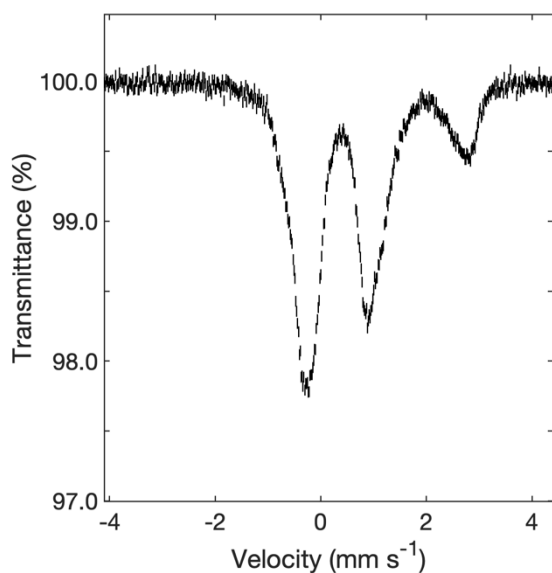


**Figure 3.3.3.2.** Mössbauer spectrum (zero field, 85 K) of  $^{57}\text{Fe}$  HydG.

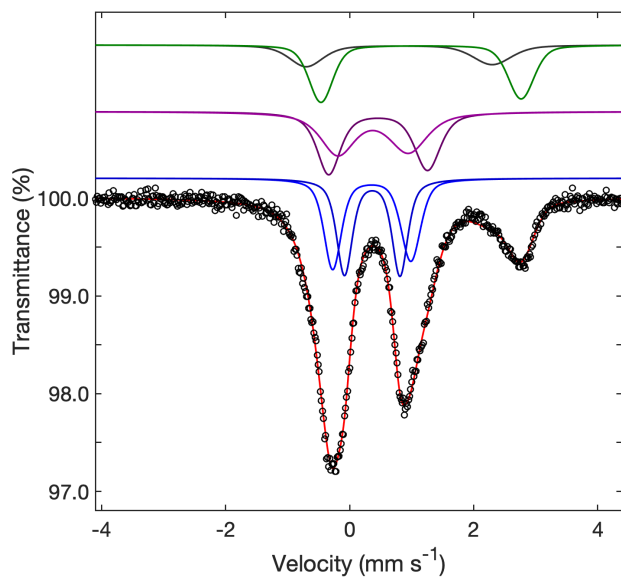


**Figure 3.3.3.3.** Mössbauer spectrum (zero field, 80 K) of  $^{57}\text{Fe}$  HydG with the total fit (red trace) and components corresponding to the dangler  $\text{Fe}^{2+}$  (green trace), the  $[\text{4Fe-4S}]^+_{\text{aux}}$  (purple trace) and  $[\text{4Fe-4S}]^+_{\text{RS}}$  (blue trace) mixed valence pairs, and adventitiously bound Fe (black trace). (See appendix SI Table 1 for fitting details).

$\chi^2 = 1.347$	$\delta$ (mm s <sup>-1</sup> )	$\Delta E_Q$ (mm s <sup>-1</sup> )	Area (%)	Relative Ratio
Adventitious Fe	0.80	3.00	8.8	0.9
Dangler Fe	1.15	3.23	15.7	1.6
Aux1	0.46	1.59	18.8	2.0
Aux2	0.38	1.14	18.8	2.0
RS1	0.37	1.26	19.1	2.0
RS2	0.35	0.89	18.8	2.0

**Table 3.3.3.1.** Mössbauer fitting parameters corresponding to SI Fig. 2

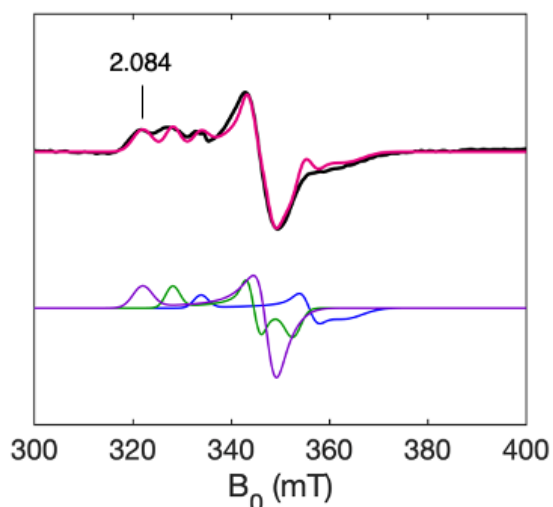


**Figure 3.3.3.4.** Top: CW EPR of <sup>57</sup>Fe HydG after turnover for 60 min with DTH, SAM, and L-Tyr (black trace), and total simulation (magenta trace). Bottom: simulations of the top black trace with three species SAM-bound [4Fe-4S]<sub>RS</sub><sup>+</sup> cluster  $g = [2.009 \ 1.884 \ 1.843]$  (22%, blue trace), unknown structure  $g = [2.045 \ 1.947 \ 1.903]$  (10%, green trace), and cyanide-bound [4Fe-4S]<sub>aux</sub><sup>+</sup> cluster  $g = [2.084 \ 1.929 \ 1.920]$  (50%, purple trace). The parameters for X-band (9.4 GHz) CW EPR are temperature, 10 K; microwave power, 0.1 mW; modulation amplitude, 0.5 mT.

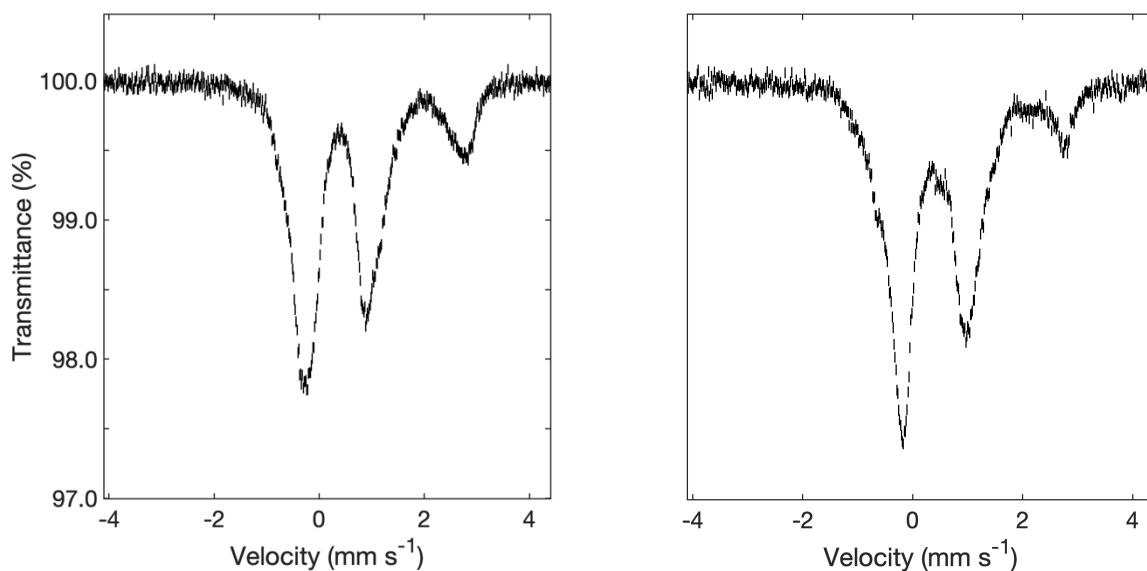


**Figure 3.3.3.5.** (Left) Mössbauer spectrum (zero field, 85 K) of  $^{57}\text{Fe}$  HydG. (Right) Mössbauer spectrum (zero field, 85 K) of  $^{57}\text{Fe}$  HydG after turnover for 60 min with DTH, SAM, and L-Tyr.

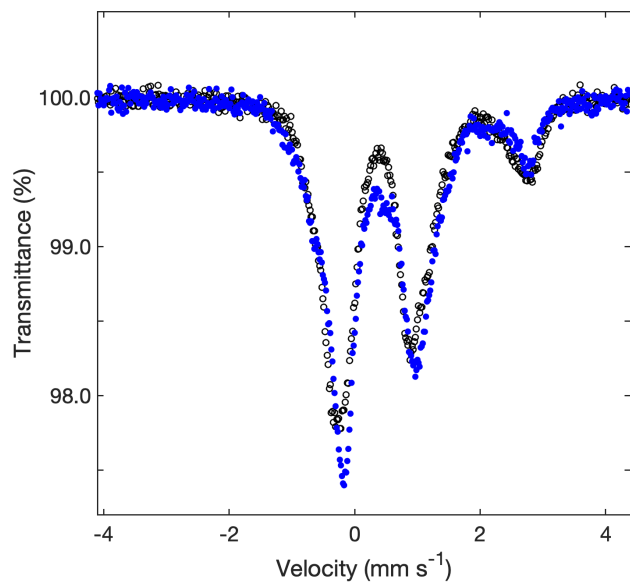


**Figure 3.3.3.6.** Mössbauer spectra (zero field, 85 K) of  $^{57}\text{Fe}$  HydG after turnover with 10 mM DTH, 10 L-Tyr, and 5 mM SAM after 60 min (blue circles) directly overlaid on resting state HydG control sample (black circles).

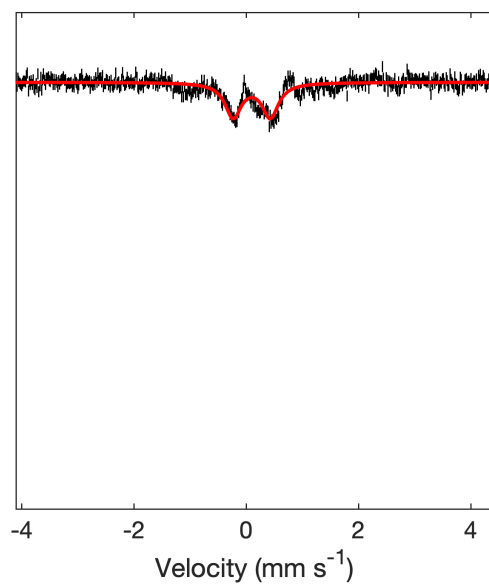


**Figure 3.3.3.7.** Difference spectrum (black trace) between 60 min experimental spectrum and resting state simulation, total simulation (red trace)(See **Table 1** for Mössbauer fitting parameters).

### 3.4. References

1. Popescu, C. V.; Munck, E., Electronic structure of the H cluster in [Fe]-hydrogenases. *J Am Chem Soc* **1999**, *121* (34), 7877-7884.
2. Pereira, A. S.; Tavares, P.; Moura, I.; Moura, J. J. G.; Huynh, B. H., Mossbauer characterization of the iron-sulfur clusters in *Desulfovibrio vulgaris* hydrogenase. *J Am Chem Soc* **2001**, *123* (12), 2771-2782.
3. Gilbert-Wilson, R.; Siebel, J. F.; Adamska-Venkatesh, A.; Pham, C. C.; Reijerse, E.; Wang, H. X.; Cramer, S. P.; Lubitz, W.; Rauchfuss, T. B., Spectroscopic Investigations of [FeFe] Hydrogenase Maturated with [Fe-57(2)(adt)(CN)(2)(CO)(4)](2-). *J Am Chem Soc* **2015**, *137* (28), 8998-9005.
4. Beinert, H.; Holm, R. H.; Munck, E., Iron-sulfur clusters: Nature's modular, multipurpose structures. *Science* **1997**, *277* (5326), 653-659.
5. Zener, C., Interaction between the D-Shells in the Transition Metals. *Phys Rev* **1951**, *81* (3), 440-444.
6. Anderson, P. W.; Hasegawa, H., Considerations on Double Exchange. *Phys Rev* **1955**, *100* (2), 675-681.
7. Birrell, J. A.; Pelmeshnikov, V.; Mishra, N.; Wang, H. X.; Yoda, Y.; Tamasaku, K.; Rauchfuss, T. B.; Cramer, S. P.; Lubitz, W.; DeBeer, S., Spectroscopic and Computational Evidence that [FeFe] Hydrogenases Operate Exclusively with CO-Bridged Intermediates. *J Am Chem Soc* **2020**, *142* (1), 222-232.
8. Fish, W. W., Rapid Colorimetric Micromethod for the Quantitation of Complexed Iron in Biological Samples. *Methods in Enzymology* **1988**, *158*, 357-364.
9. Suess, D. L. M.; Burstel, I.; De La Paz, L.; Kuchenreuther, J. M.; Pham, C. C.; Cramer, S. P.; Swartz, J. R.; Britt, R. D., Cysteine as a ligand platform in the biosynthesis of the FeFe hydrogenase H cluster. *P Natl Acad Sci USA* **2015**, *112* (37), 11455-11460.

## Chapter 4

### Characterizing the biosynthesis of the $[\text{Fe(II)(CN)(CO)}_2(\text{cysteinate})]^-$ organometallic product from selectively labeled $^{57}\text{Fe}$ HydG

#### 4.1. Introduction to the “dangler” Fe of HydG

Enzymes containing Fe-S clusters that incorporate heteroatoms are known to catalyze a variety of biochemical reactions. Nitrogenase enzymes may contain Mo or V in their Fe-S active sites to reduce  $\text{N}_2$  to  $\text{NH}_3$ , and Carbon monoxide dehydrogenase/acetyl-CoA synthase utilize a Ni-Fe-S cluster to reduce  $\text{CO}_2$  in CO fixation.<sup>1,2</sup> An artificial method to incorporate heteroatoms into an Fe-S cluster is to remove a corner site Fe with a metal chelator and reconstitute with a different metal ion. Removing the non-cysteinal-coordinated Fe from the 4Fe-4S cubane in *Pyrococcus furiosus* ferredoxin, and replacing it with a another metal ( $\text{M} = \text{Co}, \text{Ni}, \text{Zn}, \text{Cd}, \text{Cu}, \text{Cr}$ ) has previously produced a series of new  $\text{MFe}_3\text{S}_4$  clusters with new redox and spectroscopic properties.<sup>3-7</sup> HydG has a labile Fe capable of exchange, such as that seen in *Pyrococcus furiosus* ferredoxin. The 5<sup>th</sup> “dangler” Fe, found at the auxiliary cluster by catalytic design is more labile than the Fe found in the auxiliary or Radical SAM Fe-S clusters.<sup>8-10</sup> The Fe and L-Cys at the “dangler” position have shown to be exchangeable for Ni, Co, and Selenocysteine.<sup>8,11</sup> The auxiliary Fe-S cluster typically displays a resting state  $S = 5/2$ , the coupling between a high spin  $\text{Fe}^{2+}$   $S = 2$  and [4Fe-4S] cluster  $S = 1/2$  (**Section 2.3.2**). If the dangler Fe is removed and a  $\text{Ni}^{2+}$  ion ( $S = 1$ ) is incorporated then a unique  $S = 3/2$  signal can be observed by EPR, the result of coupling between  $\text{Ni}^{2+}$   $S = 1$  and [4Fe-4S] cluster  $S = 1/2$ . Whereas if the auxiliary cluster is reconstituted with  $\text{Co}^{2+}$  ( $S = 3/2$ ) the coupling with the  $[\text{4Fe-4S}]_{\text{aux}}$  cluster results in an EPR silent  $S = 2$  or  $S = 1$  state. This spin state can derive from either ferromagnetic or antiferromagnetic coupling. The results of these previous experiments indicate that HydG will also easily be



susceptible to exchange with different isotopes of Fe, opening it up to selective Mössbauer Spectroscopy experiments.

#### **4.1.1. Metal chelators removing the Dangler Fe**

Various metal chelators were tested to find a chelator capable of removing the “dangler” Fe at the auxiliary cluster without causing damage to the protein. Imidazole, nitrilotriacetic acid (NTA), 2,2'-bipyridine, and ethylene diamine triacetic acid (EDTA) were all incubated with HydG for 20 min, then washed away using amicon filters (10-kDa cutoff). After 3 centrifuge/wash cycles with buffer, the remaining protein was frozen into EPR samples (**Figure 4.1.1.1. and Figure 4.1.1.2.**). Results display the metal chelators potential to remove the “dangler” Fe. The resulting  $S = \frac{1}{2}$  EPR signal after treatment with metal chelator is associated with the auxiliary cluster,  $g = 2.06$ . Imidazole showed only a slight ability to remove the high spin Fe(II) ion, whereas NTA and 2,2'-bipyridine were more successful. EDTA was the most efficient at removing large amounts of the dangler Fe. EPR taken at lower field also reflect these results. The extent to which the  $S = 5/2$  signal decreases relative to a control sample is proportional to the amount of dangler Fe that had been removed. An important observation in addition to these results, was that all metal chelators caused some level of protein precipitation except for 2,2'-bipyridine. This gentle nature, along with the visible red color that 2,2'-bipyridine produces when it binds ferrous Fe made it a suitable choice for experiments removing the “dangler” Fe.

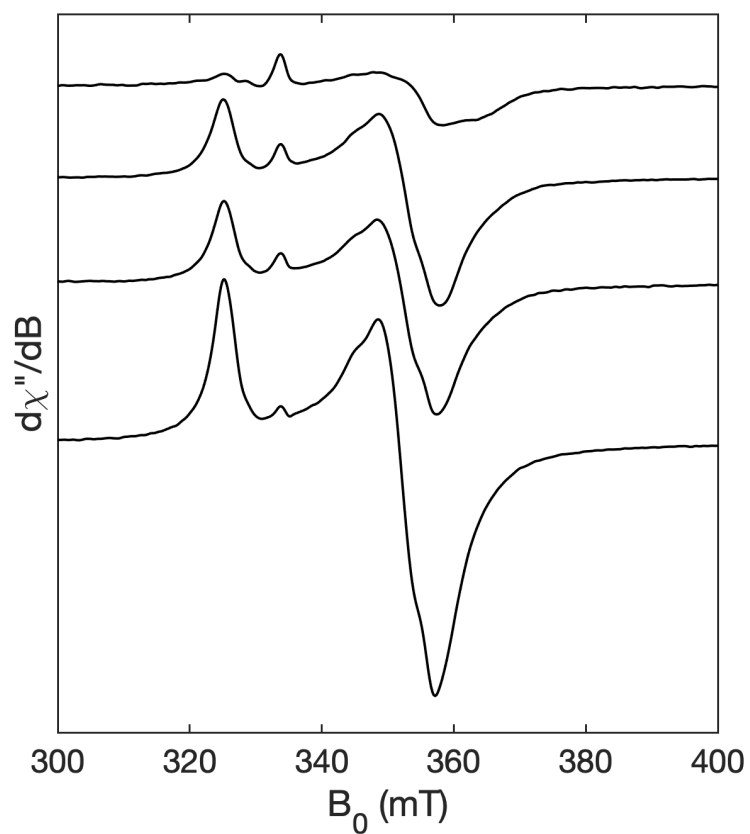


**Figure 4.1.1.1.** X-band (9.4 GHz) CW EPR of HydG treated with the metal chelators (Top to Bottom) imidazole, nitrilotriacetic acid, 2,2'-bipyridine, and EDTA in the presence of DTH and SAM. The parameters for X-band (9.4 GHz) CW EPR are temperature, 10 K; microwave power, 0.1 mW; modulation amplitude, 0.5 mT.

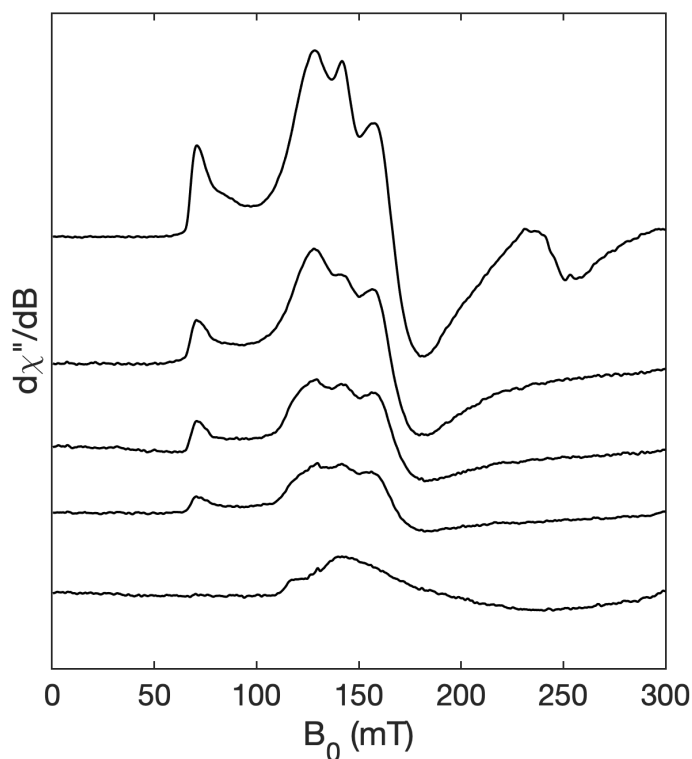


**Figure 4.1.1.2.** X-band (9.4 GHz) CW EPR of HydG auxiliary cluster treated with the metal chelators (Top to Bottom) control sample, imidazole, nitrilotriacetic acid, 2,2'-bipyridine, and EDTA in the presence of DTH and SAM. The parameters for X-band (9.4 GHz) CW EPR are temperature, 10 K; microwave power, 0.1 mW; modulation amplitude, 0.5 mT.

#### 4.1.2. Preparing $^{57}\text{Fe}$ dangler labeled HydG

DTH, SAM, L-Cys, and either EDTA or Bipyridine solutions were added to freshly thawed solutions of HydG (in that order). The resulting solution was mixed gently and allowed to stand at room temperature for 5 min. The solution was then diluted 10-fold with buffer containing DTH, SAM, and L-Cys and subsequently concentrated 10-fold using an Amicon centrifugal filter (10-kDa cutoff). This was repeated as many times as necessary. In the case for Bipyridine, the process was repeated until any visible red color had completely washed through.

Samples were then incubated with excess  $^{57}\text{Fe}^{2+}$  (ferrous ammonium citrate) along with DTH, SAM, and L-Cys. The protein solution was then washed a total of 3 times as previously described<sup>9</sup> until all the excess  $^{57}\text{Fe}^{2+}$  had been removed.

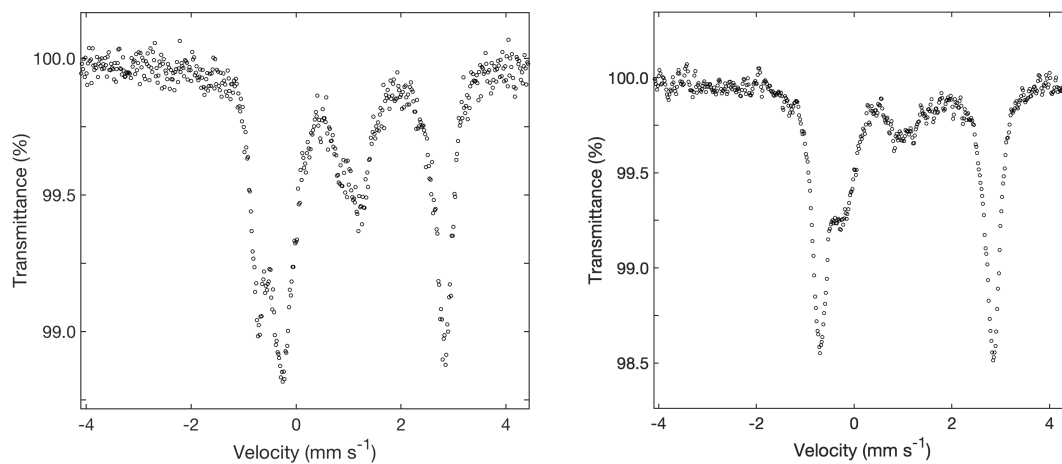


**Figure 4.1.2.1.** Mössbauer spectra comparing resting state HydG prepared by removal of the “dangler” Fe with (Left) EDTA and (Right) 2,2'-bipyridine, followed by reconstitution with  $^{57}\text{Fe}^{2+}$ .

### 4.1.3. Observing the $[\text{Fe(II)(CN)(CO)}_2(\text{cysteinate})]$ product, Complex B, by $^{57}\text{Fe}$ Mössbauer Spectroscopy in selectively labeled HydG

Experiments were next carried out on the prepared HydG with the dangler  $\text{Fe}^{2+}$  selectively labeled with  $^{57}\text{Fe}$ . The goal of these measurements was to further confirm the newly observed Fe species from Complex B, through  $^{57}\text{Fe}$  Mössbauer spectroscopy (**Section 3.3.3**). Labeling was achieved in two steps, starting with isotope exchange of the dangler Fe followed by activation to poise the selectively-labeled HydG in a state relevant to catalysis. In the first step, freshly thawed samples HydG were treated with a metal chelator bipyridine to give the metastable  $\text{HydG}^{\text{-danglerFe}}$ . This species was immediately reconstituted with  $^{57}\text{Fe}^{2+}$  in the form of soluble ferrous ammonium citrate. In this way, the dangler position was selectively labeled (**Figure 4.1.3.2**). The demetallation-remetallation sequence introduces some impurities as indicated by weak absorptions that match  $^{57}\text{Fe}$  Mössbauer values seen for  $[\text{4Fe-4S}]_{\text{RS}}$  and  $[\text{4Fe-4S}]_{\text{aux}}$  clusters. This labile behavior of Fe "corner sites" is typical of site-differentiated  $[\text{4Fe-4S}]$  clusters (**Figure 4.1.3.3**).<sup>12-20</sup> The dominant signals in the Mössbauer spectrum of the  $^{57}\text{Fe}$ -labeled sample are from the high spin dangler Fe. Allowing this selectively  $^{57}\text{Fe}$  labeled HydG to undergo catalysis in the presence of DTH, SAM, and L-Tyr for 60 min produces changes in the Mössbauer and EPR spectra. In the Mössbauer spectrum the high spin dangler  $\text{Fe}^{2+}$  signal decreases and a new Fe species appears at a low isomer shift value. Signals for the  $[\text{4Fe-4S}]_{\text{RS}}$  and  $[\text{4Fe-4S}]_{\text{aux}}$  clusters had no noticeable change (**Figure 4.1.3.1**). The observable changes are consistent with those seen in the MB spectra of fully  $^{57}\text{Fe}$ -labeled HydG. The EPR spectrum of a sample prepared in parallel contained the cyanide-bound  $[\text{4Fe-4S}]_{\text{aux}}$  cluster signal and displayed a decrease in the characteristic  $S = 5/2$  signal at low-field (**Figure 4.1.3.1** and **Figure 4.1.3.4**). EPR simulation also reveals the presence of the intermediate Complex A, a result of the enzyme

not completely turning over to Complex B. This partial conversion is tentatively attributed to damage to HydG reactivity from the  $^{57}\text{Fe}$  labeling process. Nevertheless, the  $^{57}\text{Fe}$  Mössbauer spectrum after 60 min under turnover conditions displays a clear decrease in the signal for the high spin dangler  $\text{Fe}^{2+}$  along with the appearance of at least two new Fe species at lower velocity (Figure 4.1.3.6). The change in the Mössbauer spectrum is now simulated as a mixture of two species, Complex A and Complex B. By holding the parameters for Complex B constant, it is then possible to extract the parameters for Complex A:  $\delta = 0.12 \text{ mm s}^{-1}$  and  $\Delta E_Q = 0.45 \text{ mm s}^{-1}$  (Figure 4.1.3.7). Being very similar structurally, Complex A and Complex B have nearly indistinguishable  $^{57}\text{Fe}$  Mössbauer parameters at zero-field.

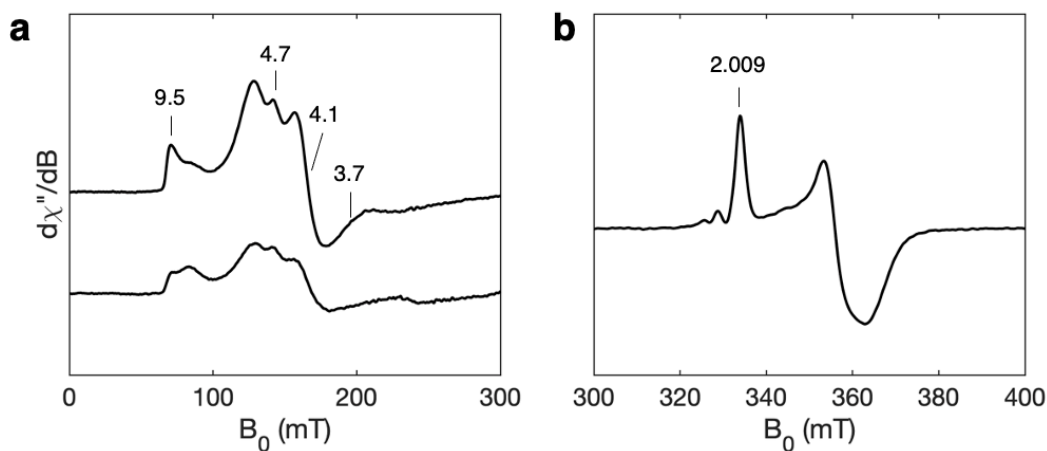


**Figure 4.1.3.1. a.** Top: CW EPR of  $^{57}\text{Fe}$  selectively labeled HydG auxiliary cluster. Bottom: CW EPR of  $^{57}\text{Fe}$  selectively labeled HydG auxiliary cluster after turnover for 60 min with DTH, SAM, and L-Tyr. **b.** CW EPR of selectively  $^{57}\text{Fe}$  labeled HydG SAM-bound  $[4\text{Fe-4S}]_{\text{RS}}^+$  cluster (black trace). The parameters for X-band (9.4 GHz) CW EPR are temperature, 10 K; microwave power, 5 mW (a), 0.1 mW (b); modulation amplitude, 0.5 mT.

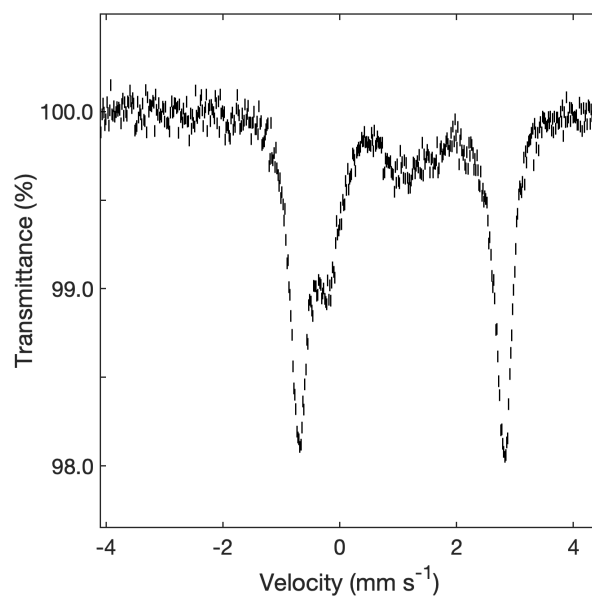


**Figure 4.1.3.2.** Mössbauer spectrum (zero field, 90 K) of  $^{57}\text{Fe}$  selectively labeled HydG.

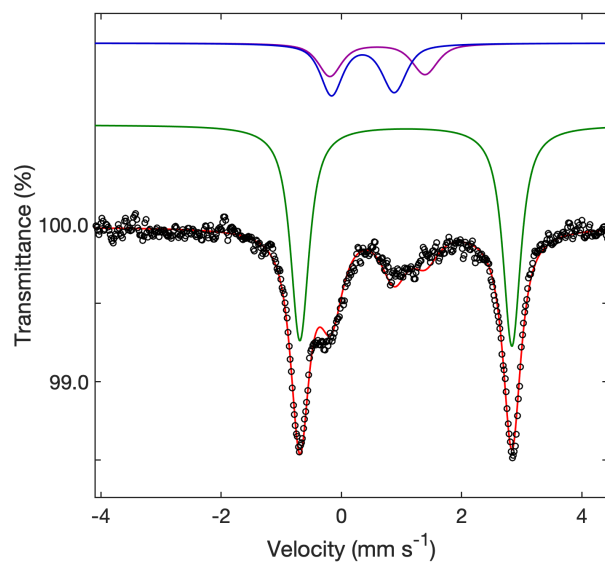


**Figure 4.1.3.3.** Mössbauer spectrum (zero field, 90 K) of selectively labeled  $^{57}\text{Fe}$  HydG with the total fit (red trace) and components corresponding to the dangler  $\text{Fe}^{2+}$  (green trace), Fe Impurity #1 (blue trace) and Fe Impurity #2 (purple trace).

$\chi^2 = 1.42$	$\delta$	$\Delta E_Q$	Area (%)
	(mm s <sup>-1</sup> )	(mm s <sup>-1</sup> )	
Dangler Fe	1.07	3.53	68.9
Fe Impurity	0.36	1.05	18.4
Fe Impurity	0.60	1.58	12.7

**Table 4.1.3.1.** Mössbauer fitting parameters corresponding to Figure 4.1.3.3.



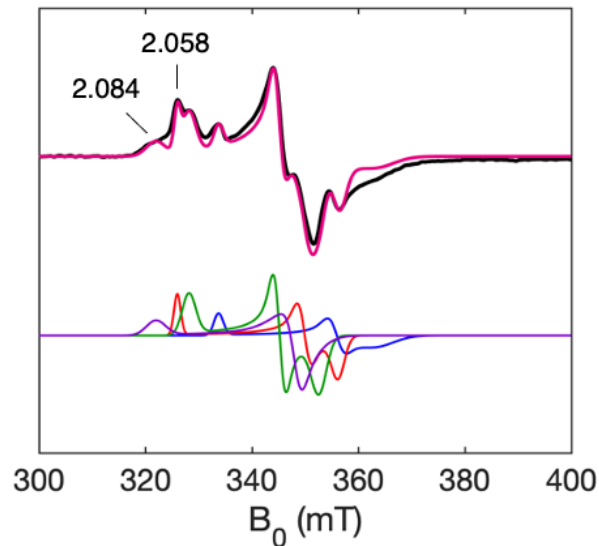


**Figure 4.1.3.4.** Top: CW EPR of selectively  $^{57}\text{Fe}$  labeled HydG after turnover for 60 min with DTH, SAM, and L-Tyr (black trace), and total simulation (magenta trace). Bottom: simulations of the top black trace with four species SAM-bound  $[\text{4Fe-4S}]_{\text{RS}}^+$  cluster  $g = [2.009 \ 1.883 \ 1.843]$  (17%, blue trace), unknown structure  $g = [2.044 \ 1.943 \ 1.902]$  (36%, green trace), Complex A  $g = [2.058 \ 1.917 \ 1.883]$  (24%, red trace), and cyanide-bound  $[\text{4Fe-4S}]_{\text{aux}}^+$  cluster  $g = [2.083 \ 1.925 \ 1.920]$  (23%, purple trace) (Full simulation details in Supplemental Information). The parameters for X-band (9.4 GHz) CW EPR are temperature, 10 K; microwave power, 0.1 mW; modulation amplitude, 0.5 mT.

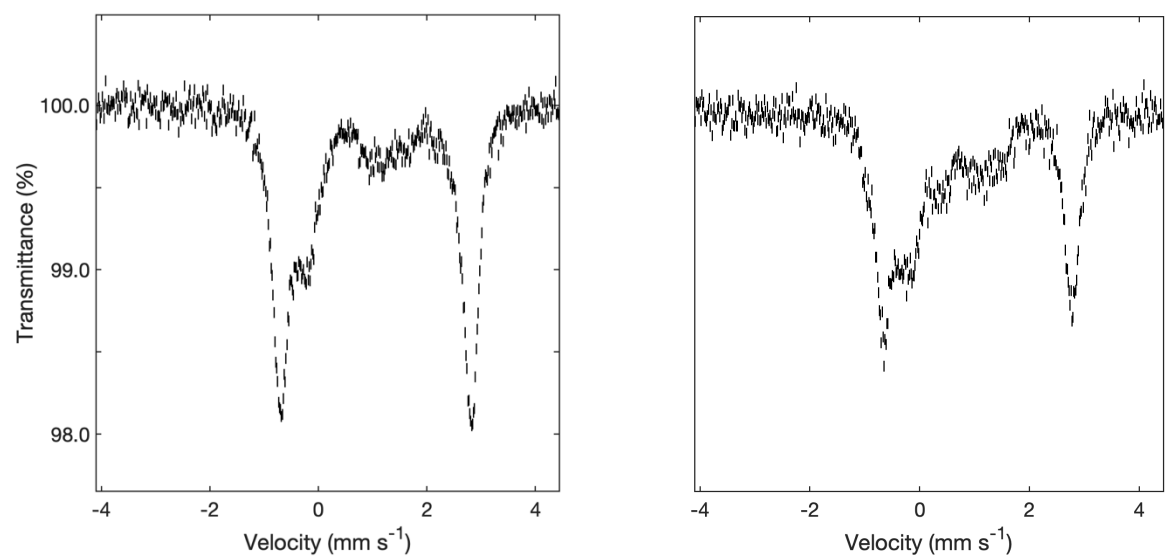


**Figure 4.1.3.5.** (Left) Mössbauer spectrum (zero field, 90 K) of  $^{57}\text{Fe}$  selectively labeled HydG. (Right) Mössbauer spectrum (zero field, 90 K) of  $^{57}\text{Fe}$  selectively labeled HydG after turnover for 60 min with DTH, SAM, and L-Tyr.

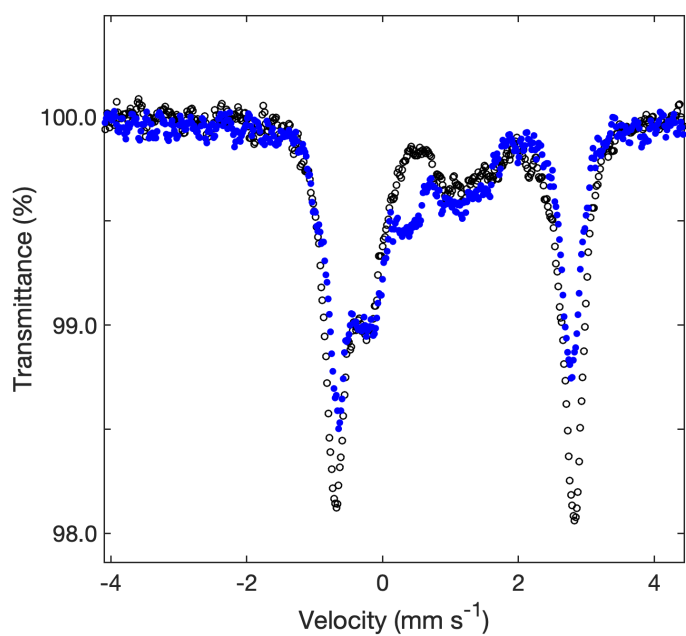


**Figure 4.1.3.6.** Mössbauer spectra (zero field, 90 K) of selective <sup>57</sup>Fe labeled HydG after turnover with 10 mM DTH, 10 mM L-Tyr, and 10 mM SAM after 60 min (blue circles) directly overlaid on selective <sup>57</sup>Fe labeled resting state HydG control (black circles).

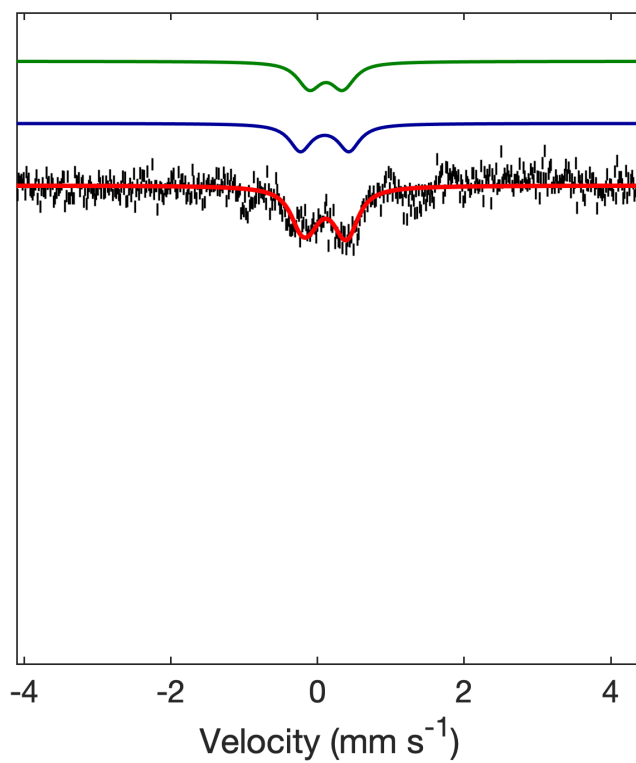


**Figure 4.1.3.7.** Difference spectrum (black trace) between 60 min experimental spectrum and resting state simulation, total simulation (red trace). Complex A (50%, green trace) and Complex B (50%, blue trace).

## 4.2. $^{57}\text{Fe}$ Mössbauer of SynB

It has been shown previously that HydG can be functionally replaced by a synthetic compound, Syn-B, in the in vitro maturation of the H-cluster.<sup>21-23</sup> Syn-B can serve as the substrate for the radical SAM enzyme HydE.<sup>22,23</sup> As previously described,<sup>21</sup> while not amenable for single crystal diffraction, Syn-B is most consistent with a chemical formula of  $(\text{Et}_4\text{N})_4\{\text{FeI}_2[\text{Fe}(\text{Cys})(\text{CN})(\text{CO})_2(\text{H}_2\text{O})]_4\}^{++}$ , i.e., a cluster composed of 4  $[\text{Fe}(\text{Cys})(\text{CN})(\text{CO})_2(\text{H}_2\text{O})]$  centers bound to  $\text{FeI}_2$ . It clearly contains the  $[\text{Fe}(\text{Cys})(\text{CN})(\text{CO})_2]$  core structure necessary for its reactivity in H-cluster maturation. The presence of a high spin Fe(II) center could additionally help to stabilize Complex B. To compare the electronic structure of the Fe centers in Syn-B to that of the  $\text{Fe}(\text{CN})(\text{CO})$  species formed in HydG, we went on to characterize Syn-B by Mossbauer spectroscopy. To this end, Syn-B was prepared as an all  $^{57}\text{Fe}$  version. This  $^{57}\text{Fe}$ -SynB exhibits consistent physical properties as that prepared with natural-abundance Fe. (**Section 4.4.**) The Mössbauer spectrum for Syn-B exhibits signals at  $\delta = 0.11$   $\text{mm s}^{-1}$  and  $\Delta E_Q = 0.68$   $\text{mm s}^{-1}$  assigned to low spin  $\text{Fe}^{2+}$  ion bound by L-cysteine, CO, and CN<sup>-</sup> (**Figure 4.2.1., Table 4.3.1.**) A second signal with  $\delta = 1.41$   $\text{mm s}^{-1}$  and  $\Delta E_{Q1} = 3.00$  is consistent with high spin  $\text{Fe}^{2+}$ .

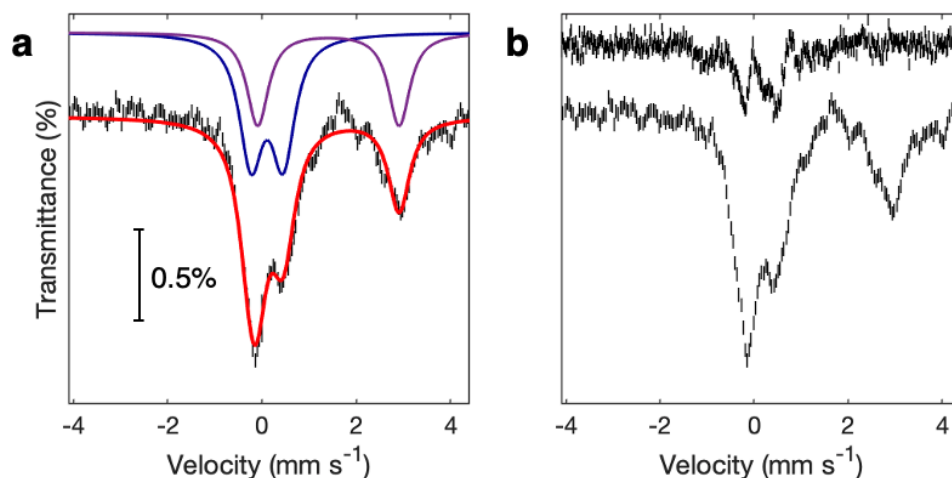


**Figure 4.2.1. a.** Mössbauer spectrum (1kG field, 4.2 K) of  $^{57}\text{Fe}$  Syn-B with total fit (red trace) and components corresponding to low spin ferrous species (59%, blue trace) and high spin ferrous species (41%, purple trace). **b.**  $^{57}\text{Fe}$  SynB Mössbauer spectrum (bottom) and  $^{57}\text{Fe}$  HydG Mössbauer difference spectrum (top) displaying Complex B. (Difference spectrum of  $^{57}\text{Fe}$  HydG has been resized for comparison).

#### 4.3. Discussion of $^{57}\text{Fe}$ Mössbauer Results for Fully and Selectively Labeled Experiments

The  $^{57}\text{Fe}$  Syn-B Mössbauer results can serve as a basis for comparison to Mössbauer parameters seen for Complex B (**Figure 4.2.1.1.**) along with  $^{57}\text{Fe}$  Mössbauer results from the prior studies of mono-nuclear Fe biomimetic models of [FeFe]-hydrogenases (**Table 4.3.1.**). In all of these examples, the Fe ion has a low spin Fe(II) oxidation state and is hexacoordinated by a comparable set of ligands, which includes carbonyls. These similarities result in observed low isomer shifts  $\delta = 0.007 - 0.15 \text{ mm s}^{-1}$  and small quadrupole splittings  $\Delta E_Q = 0.43 - 0.91$ .<sup>24, 25</sup>

**Table 4.3.1. Mössbauer parameters for low spin Fe in Complex B, Syn-B, and select biomimetic models of [FeFe]-hydrogenase**

Compounds	$\delta$ , mm s <sup>-1</sup>	$\Delta E_Q$ , mm s <sup>-1</sup>	Ref.
<b>Complex B</b> , <i>Shewanella oneidensis</i>	0.10	0.66	This work
<b>Biomimetic models</b>			
[Fe(PS <sub>3</sub> )(CO)(CN)] <sup>2-</sup>	0.15	0.91	34
[FeI <sub>2</sub> (CO) <sub>3</sub> IMes]	0.007	0.48	35
[FeI <sub>2</sub> (CO) <sub>2</sub> PMe <sub>3</sub> ]	0.063	0.69	35
[FeI <sub>2</sub> (CO) <sub>3</sub> PPh <sub>3</sub> ]	0.090	0.43	35
(Et <sub>4</sub> N) <sub>4</sub> {FeI <sub>2</sub> [Fe(Cys)(CN)(CO) <sub>2</sub> (H <sub>2</sub> O)] <sub>4</sub> }, <b>Syn-B</b>	0.11	0.68	This work

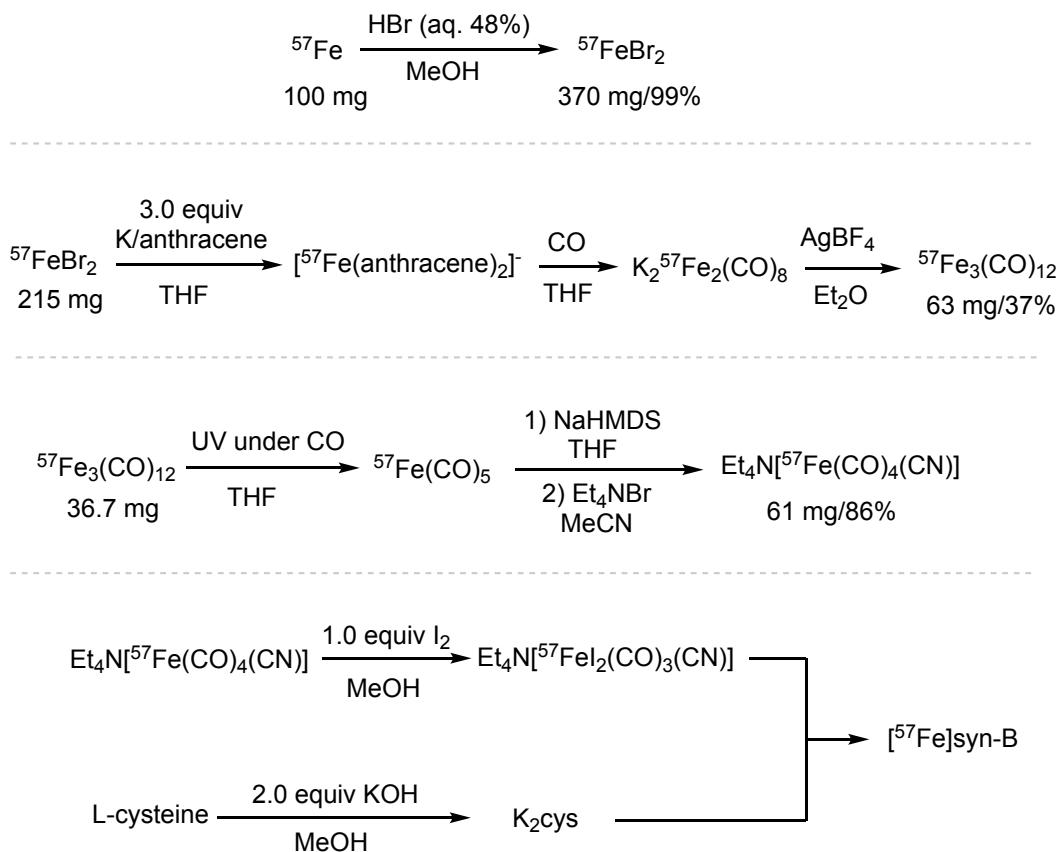
Compounds 1, 6, and 7 from ref 35

Prior to this work, the characterization of the two early biosynthetic intermediates, Complexes A and B, rested on stopped flow FTIR and EPR spectroscopy.<sup>26,27</sup> Here we have employed <sup>57</sup>Fe Mössbauer spectroscopy to observe the formation of these two Fe species produced within HydG. Both fully and selectively “dangler-Fe” <sup>57</sup>Fe labeled HydG show consistent results in the production of the product Complex B, with Mössbauer simulation parameters  $\delta = 0.10$  mm s<sup>-1</sup>,  $\Delta E_Q = 0.66$  mm s<sup>-1</sup>. The Mössbauer values for the observed product Complex B are consistent with its assignment as [Fe(II)(CN)(CO)<sub>2</sub>(cysteinate)]<sup>-</sup>. Specifically, the observed low isomer shift of  $\delta = 0.10$  mm s<sup>-1</sup> is typical of low spin ferrous species. Both of the strong field ligands CO and CN<sup>-</sup> increase the s-electron density at the Fe nucleus through  $\sigma$ -donation and  $\pi$  back bonding.<sup>28</sup> However, the most significant contributing factor that CO and CN<sup>-</sup> have to the observed low isomer shift would be the shorter bonds that they form through back bonding. The shortened bonds result in a contraction of orbitals on Fe, increasing the s-electron density experienced at the nucleus.<sup>29</sup> The small quadrupole splitting for Complex B of  $\Delta E_Q = 0.66$  mm s<sup>-1</sup> is the expected result of a low spin ferrous electron configuration, with a coordination structure of high symmetry.

Taking the simulation parameters from the fully labeled experiment has also allowed for us to extract the parameters of Complex A, having values of  $\delta = 0.12 \text{ mm s}^{-1}$ ,  $\Delta E_Q = 0.45 \text{ mm s}^{-1}$ . We also report Mössbauer results for the  $^{57}\text{Fe}$  Syn-B complex, with  $\delta = 0.11 \text{ mm s}^{-1}$ ,  $\Delta E_Q = 0.68 \text{ mm s}^{-1}$ . The excellent agreement of Complex B with published  $^{57}\text{Fe}$  Mössbauer parameters for mononuclear biomimetic models of the H-cluster and  $^{57}\text{Fe}$  Syn-B establishes the key role that HydG plays. Not only in producing CO and  $\text{CN}^-$ , but in resetting the electronic structure of a ferrous ion from high to low spin, on path towards H-cluster maturation. The addition of CO,  $\text{CN}^-$ , and thiolate ligation by HydG is an important prerequisite to the catalytic transformations that occur on the rSAM enzyme HydE. Although further mechanistic details for HydE and the maturase enzyme HydF must still be resolved, including how the electronic structure evolves as two  $[\text{Fe}(\text{II})(\text{CN})(\text{CO})_2(\text{cysteinate})]^-$  synthons are activated for dimerization by HydE, and as the azadithiolate bridge is installed in the final completion of the H-cluster.



#### 4.4. Preparation of $^{57}\text{Fe}$ SynB



**Scheme 4.4.1.** Preparation of  $^{57}\text{Fe}$  SynB

##### 4.4.1. $^{57}\text{FeBr}_2$

$^{57}\text{FeBr}_2$  was prepared by a modified procedure<sup>30</sup>. A 100 mL Schlenk flask was charged with  $^{57}\text{Fe}$  metal powder (1.75 mmol, 100 mg) and 20 mL degassed MeOH in a glovebox. To this was added degassed HBr (10.5 mmol, 1.2 mL, 48% aqueous). The mixture was allowed to heat at 60 °C under  $\text{N}_2$  atmosphere. A light-yellow homogenous solution was obtained after overnight, at which point iron particles were completely consumed. The solvents were removed under vacuum at 60 °C. The resulting orange solid,  $^{57}\text{Fe}(\text{MeOH})_6\text{Br}_2$ , was further heated at 160

°C in an oil bath under vacuum for 5 h to remove coordinating MeOH. Oily residue adsorbed on the interior wall of the flask was carefully washed down to the bottom with THF in the glovebox and the mixture was subject to heating at 160 C° under vacuum again to afford a bright-yellow solid of anhydrous  $^{57}\text{FeBr}_2$  (370 mg, 99%).

#### 4.4.2. $\text{K}_2^{57}\text{Fe}_2(\text{CO})_8$

$\text{K}_2^{57}\text{Fe}_2(\text{CO})_8$  was prepared by a modified procedure<sup>31,32</sup>. In a 20 mL vial, freshly cut potassium (3.6 mmol, 141 mg) was stirred with anthracene (3.6 mmol, 641 mg) in dry THF (18 mL) overnight, leaving a deep blue solution. In a separate 20 mL vial,  $^{57}\text{FeBr}_2$  (1 mmol, 215 mg) was stirred in THF (4 mL) overnight to prepare a pale suspension. The above two solutions were respectively transferred to 100 mL round-bottomed flasks and cooled to -78 °C. At this temperature, the suspension of  $^{57}\text{FeBr}_2$  was cannula transferred to the solution of potassium anthracene slowly. The resulting dark solution (~ 50 mL) was allowed to warm to room temperature gradually over a course of 5 h. A dark brown solution of  $\text{K}[^{57}\text{Fe}(\text{anthracene})_2]$  was formed and then subject to a cooling bath at -78 C°. Dry CO (99.999%) was bubbled into the solution at this temperature for 1.5 h. After that, a CO balloon (1.5 L) was attached to the headspace of the flask to keep a constant atmosphere of CO. The reaction mixture was allowed to warm to room temperature overnight, producing a blackish-grey suspension. Et<sub>2</sub>O (50 mL) was added to the suspension to cause a precipitation. The mixture was filtered via an M frit to give a black solid, which was rinsed with THF/Et<sub>2</sub>O (1:1, 80 mL) three times to completely remove anthracene. After vacuum drying, a grey solid (400 mg) was obtained. The solid contains both crude  $\text{K}_2^{57}\text{Fe}_2(\text{CO})_8$  and KBr, which was good enough for the following oxidation reaction (since the KBr salt was not redox active).

#### 4.4.3. $^{57}\text{Fe}_3(\text{CO})_{12}$

$\text{Fe}_3(\text{CO})_{12}$  was prepared by a modified procedure<sup>33</sup>. The solid (400 mg) containing  $\text{K}_2^{57}\text{Fe}_2(\text{CO})_8$  and KBr was ground to a fine powder and then stirred in  $\text{Et}_2\text{O}$  (20 mL) to give a grey suspension. In a separate flask, excess  $\text{AgBF}_4$  (3.2 mmol, 624 mg) was dissolved in  $\text{Et}_2\text{O}$  (30 mL). To this clear solution was added the above grey suspension, causing an immediate color change from colorless to greenish black. After vigorously stirring for 2 h, the reaction mixture was filtered via a pad of silica gel in a glovebox to remove inorganic metal particles and salts ( $\text{Ag}$  metal,  $\text{AgBF}_4$ , KBr, and  $\text{KBF}_4$ ). The green filtrate was concentrated to dryness, affording a black solid of  $^{57}\text{Fe}_3(\text{CO})_{12}$  (63 mg/37% isolated yield based on Fe). The FT-IR spectrum of  $^{57}\text{Fe}_3(\text{CO})_{12}$  was consistent with that reported for  $\text{Fe}_3(\text{CO})_{12}$  (**Figure 4.4.3.1**).  $^{57}\text{Fe}_3(\text{CO})_{12}$  was further confirmed by the high resolution EI mass spectroscopy (HR-MS calculated for  $[\text{M}]^+$ : 506.7455, found: 506.7452) (**Figure 4.4.3.2**).

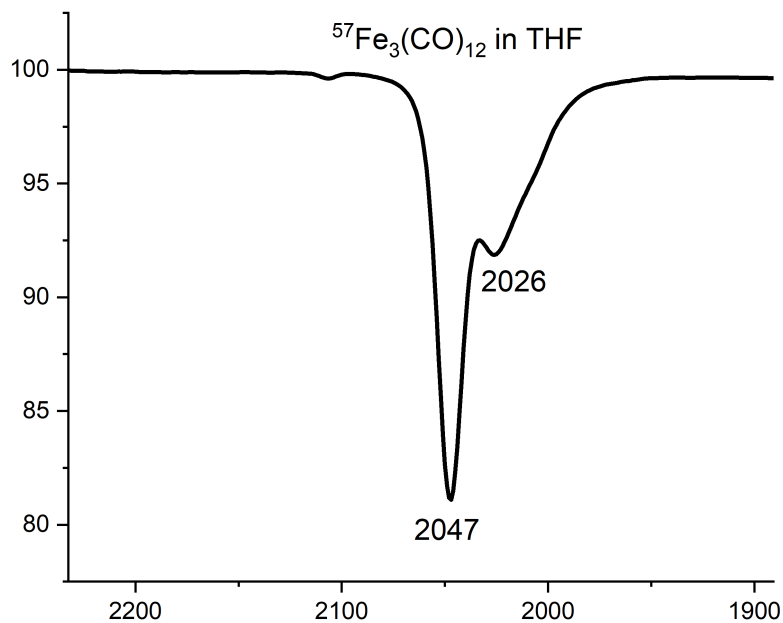


**Figure 4.4.3.1.** IR spectrum of  $^{57}\text{Fe}_3(\text{CO})_{12}$  in a THF solution at 22 °C.

**Elemental Composition Report**

Page 1

**Single Mass Analysis**

Tolerance = 5.0 PPM / DBE: min = -1.5, max = 150.0  
 Element prediction: Off

Monoisotopic Mass, Odd and Even Electron Ions

67 formula(e) evaluated with 1 results within limits (all results (up to 1000) for each mass)

Elements Used:

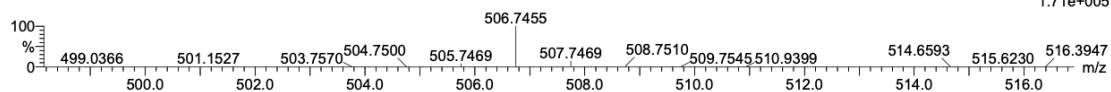
C: 0-100 H: 0-200 O: 0-20  $^{57}\text{Fe}$ : 3-3

GCT\_6136 322 (11.807) Cm (309:322-29:44x10.000)

Liu, Liang, [ $^{57}\text{Fe}$ ]-Fe<sub>3</sub>(CO)<sub>12</sub>

TOF MS EI+

1.71e+005



Minimum: -1.5  
 Maximum: 150.0

Mass	Calc. Mass	mDa	PPM	DBE	i-FIT	Formula
506.7455	506.7452	0.3	0.6	13.0	68.1	C12 O12 $^{57}\text{Fe}$ 3

**Figure 4.4.3.2.** HR-MS spectrum of  $^{57}\text{Fe}_3(\text{CO})_{12}$ .

#### 4.4.4. $^{57}\text{Fe}(\text{CO})_5$ (in THF)

$\text{Fe}(\text{CO})_5$  was prepared in laboratories before<sup>34,35</sup>. However, the reported procedures required the use of hydrogen gas either at high temperature or high pressure, which was not readily available in common synthetic labs. Herein we developed a facile method to prepare  $\text{Fe}(\text{CO})_5$  at ambient conditions. In a 100 mL round-bottomed flask,  $^{57}\text{Fe}_3(\text{CO})_{12}$  (0.072 mmol, 36.7 mg) was dissolved in THF (40 mL). The green solution was sparged with dry CO for 0.5 h and then irradiated with UV light (254 nm). UV irradiation was stopped when the color turned to orange (~ 1.5 h), at which point a clean solution of  $^{57}\text{Fe}(\text{CO})_5$  was afforded.  $^{57}\text{Fe}(\text{CO})_5$  was confirmed by FT-IR and the yield was determined by external standard calibration (98% based on Fe) (**Figure 4.4.4.1. and Figure 4.4.4.2.**). The orange solution was brought into the glovebox and dried over molecular sieves (4Å, 10% w/v) at room temperature for 24 h to obtain a moisture-free solution of  $^{57}\text{Fe}(\text{CO})_5$ .  $^{57}\text{Fe}(\text{CO})_5$  was not separated from the solvent and used as in the solution. Note: A glass stopper instead of rubber septum is recommended for sealing the flask with aid of grease during drying.

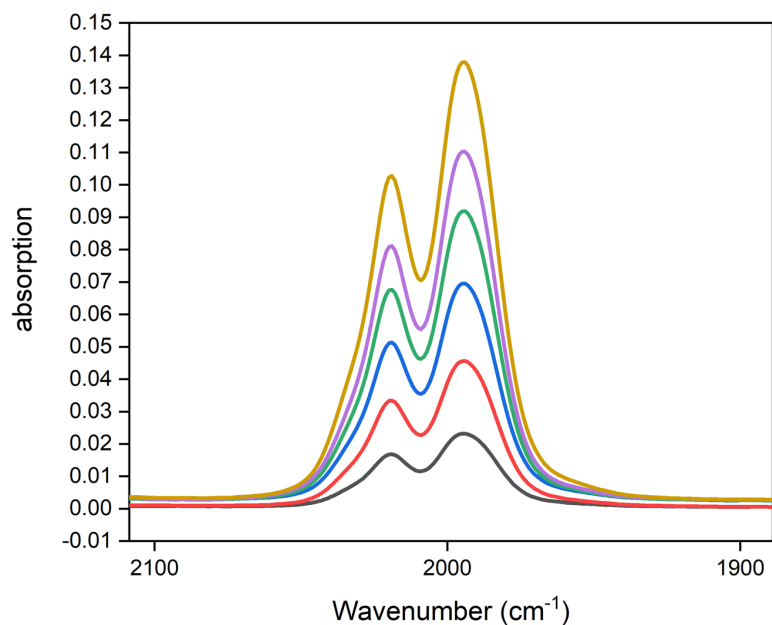


**Figure 4.4.4.1.** IR spectra of  $^{57}\text{Fe}(\text{CO})_5$  in THF solutions with varied concentrations at 22 °C.

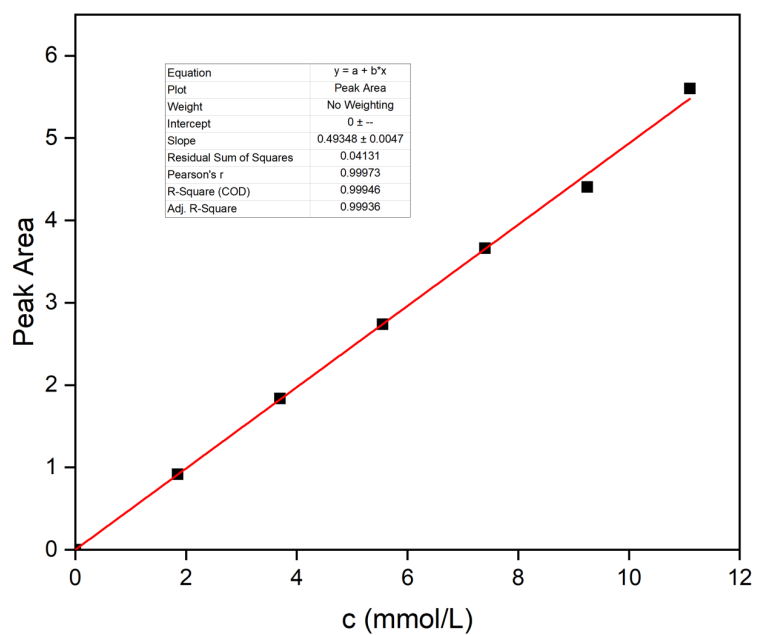


**Figure 4.4.4.2.** Calibration plot of concentration of  $^{57}\text{Fe}(\text{CO})_5$  and peak area.

#### 4.4.5. Et<sub>4</sub>N[<sup>57</sup>Fe(CO)<sub>4</sub>(CN)]

Et<sub>4</sub>N[<sup>57</sup>Fe(CO)<sub>4</sub>(CN)] was prepared by a modified procedure<sup>36</sup>. To the orange solution of <sup>57</sup>Fe(CO)<sub>5</sub> (0.21 mmol) was added NaN(SiMe<sub>3</sub>)<sub>2</sub> (0.23 mmol, 43 mg) in THF. The reaction mixture was stirred at room temperature overnight. The reaction was also monitored by infrared spectroscopy. When <sup>57</sup>Fe(CO)<sub>5</sub> was fully consumed (in ~ 4 h), the solvents were evaporated under vacuum. The residue was dissolved in MeCN (40 mL), to which Et<sub>4</sub>NBr (0.26 mmol, 55 mg) was added. The reaction mixture was kept stirring overnight. This cation exchange reaction was also monitored by the diagnostic peak of CN<sup>-</sup> on FT-IR. When the reaction was going on, the peak at 2120 cm<sup>-1</sup> weakened while a new peak at 2109 cm<sup>-1</sup> grew in (The difference indicates a weak interaction between Na<sup>+</sup> and coordinating CN<sup>-</sup>). The reaction was stopped when the peak at 2120 cm<sup>-1</sup> completely disappeared. The solvent was removed under vacuum. The resulting residue was re-dissolved in THF and filtered via an M frit to remove NaBr. The filtrate was subject to vacuum drying, leaving a light-orange solid with a trace of oily species. High resolution negative-ion ESI mass spectrum (**Figure 4.4.5.1**) showed an intense peak for a sum of [<sup>57</sup>Fe(CO)<sub>4</sub>(CN)]<sup>-</sup> and (Me<sub>3</sub>Si)<sub>2</sub>O (Calcd for {<sup>57</sup>Fe(CO)<sub>4</sub>(CN)[(Me<sub>3</sub>Si)<sub>2</sub>O]}<sup>-</sup>: 357.0077, found: 357.0078). Then the solid was stirred in a mixed solvent of pentane and Et<sub>2</sub>O (5:1) for 2 h. The clear top solution containing (Me<sub>3</sub>Si)<sub>2</sub>O was decanted and the remaining solid was subject to vacuum drying, leaving an orange solid of Et<sub>4</sub>N[<sup>57</sup>Fe(CO)<sub>4</sub>(CN)] (61 mg/86%). The FT-IR spectrum of Et<sub>4</sub>N[<sup>57</sup>Fe(CO)<sub>4</sub>(CN)] (**Figure 4.4.5.2**) was consistent with that reported for natural-abundance Et<sub>4</sub>N[Fe(CO)<sub>4</sub>(CN)].

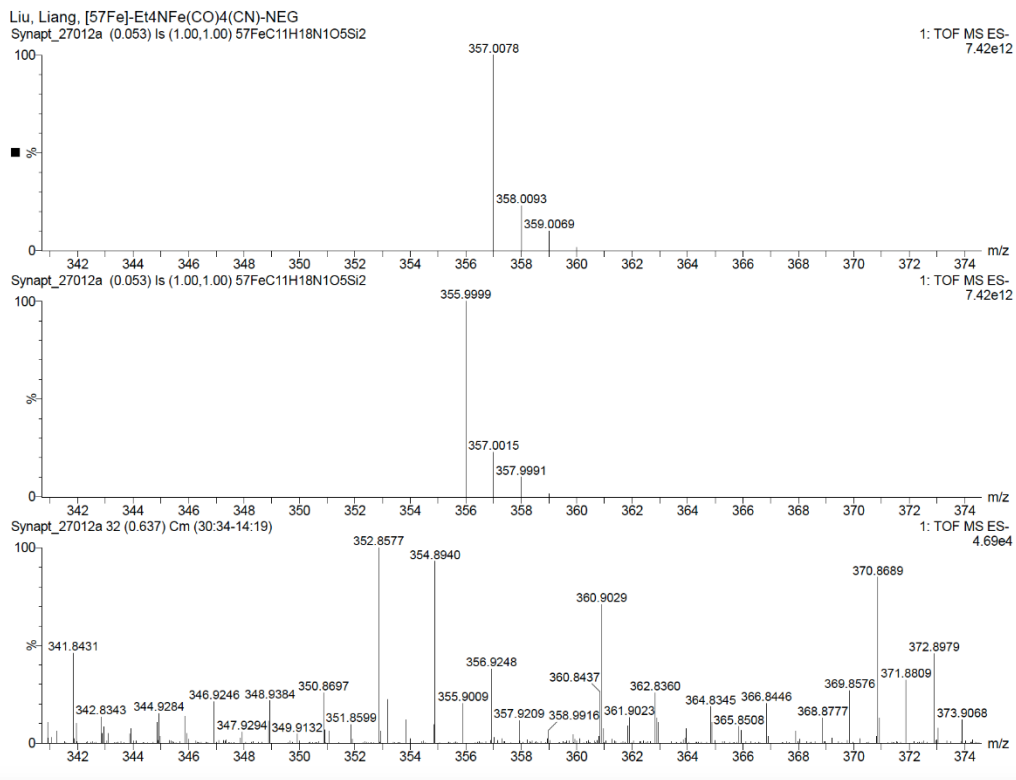


**Figure 4.4.5.1.** Negative-ion ESI mass spectrum of  $\text{Et}_4\text{N}[\text{}^{57}\text{Fe}(\text{CO})_4(\text{CN})]$ .



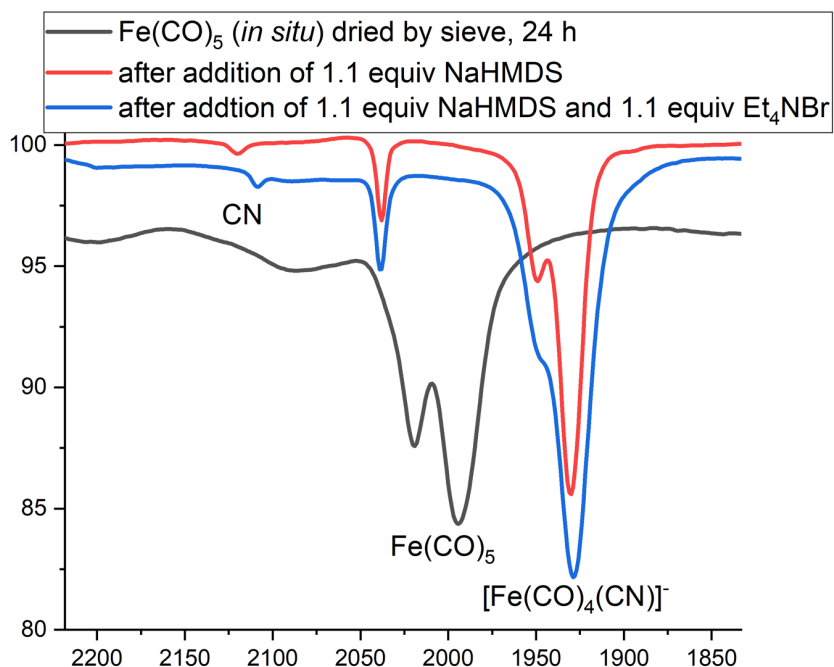


**Figure 4.4.5.2.** IR spectra of dried  $^{57}\text{Fe}(\text{CO})_5$ ,  $\text{Na}[^{57}\text{Fe}(\text{CO})_4(\text{CN})]$  and  $\text{Et}_4\text{N}[\text{Fe}(\text{CO})_4(\text{CN})]$  in THF solutions at 22 °C.

#### 4.4.6. $^{57}\text{Fe}$ Syn-B

$^{57}\text{Fe}$  Syn-B was prepared by a reported procedure for its natural-abundance Syn-B<sup>21</sup>. We would like to emphasize that a freshly-made, clean  $\text{Et}_4\text{N}[^{57}\text{FeI}_2(\text{CO})_3(\text{CN})]$  from the reaction of  $\text{Et}_4\text{N}[^{57}\text{Fe}(\text{CO})_4(\text{CN})]$  and  $\text{I}_2$  is the key to the whole route. For this step, a dilute reaction solution, vigorous stirring and slow addition of  $\text{I}_2$  solution with a pressure-equalizing dropping funnel is strongly recommended. The FT-IR spectrum of  $^{57}\text{Fe}$  Syn-B (**Figure 4.4.6.1**) was consistent with that reported for natural-abundance Syn-B.

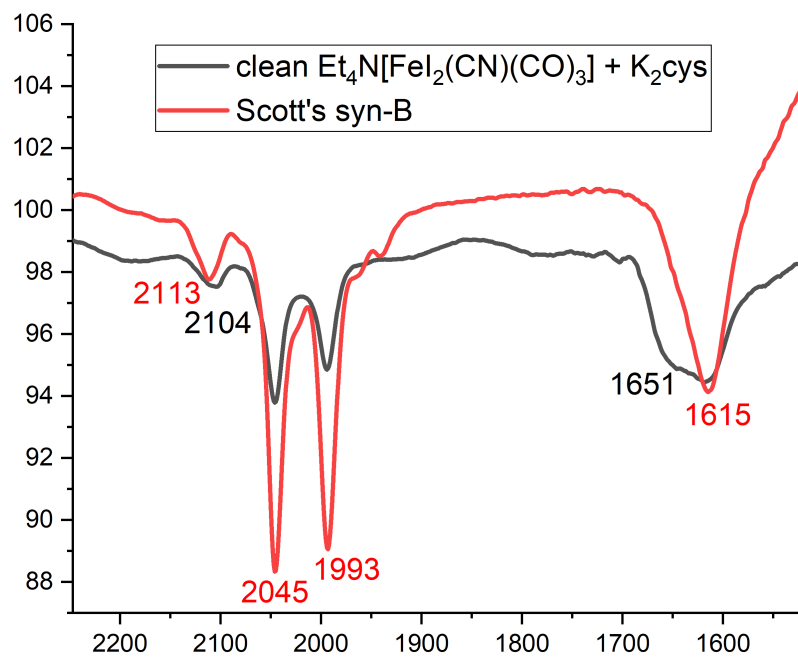


**Figure 4.4.6.1.** IR spectra of Syn-B and <sup>57</sup>Fe Syn-B in MeOH at 22 °C.

#### 4.6. References

1. Burgess, B. K.; Lowe, D. J., Mechanism of molybdenum nitrogenase. *Chem Rev* **1996**, *96* (7), 2983-3011.
2. Can, M.; Armstrong, F. A.; Ragsdale, S. W., Structure, Function, and Mechanism of the Nickel Metalloenzymes, CO Dehydrogenase, and Acetyl-CoA Synthase. *Chem Rev* **2014**, *114* (8), 4149-4174.
3. Moura, I.; Moura, J. J. G.; Munck, E.; Papaefthymiou, V.; Legall, J., Evidence for the Formation of a Cofe<sub>3</sub>s<sub>4</sub> Cluster in *Desulfovibrio-Gigas* Ferredoxin-H. *J Am Chem Soc* **1986**, *108* (2), 349-351.
4. Surerus, K. K.; Munck, E.; Moura, I.; Moura, J. J. G.; Legall, J., Evidence for the Formation of a Znfe<sub>3</sub>s<sub>4</sub> Cluster in *Desulfovibrio-Gigas* Ferredoxin-Ii. *J Am Chem Soc* **1987**, *109* (12), 3805-3807.
5. Conover, R. C.; Park, J. B.; Adams, M. W. W.; Johnson, M. K., Formation and Properties of a Nife<sub>3</sub>s<sub>4</sub> Cluster in *Pyrococcus-Furiosus* Ferredoxin. *J Am Chem Soc* **1990**, *112* (11), 4562-4564.
6. Staples, C. R.; Dhawan, I. K.; Finnegan, M. G.; Dwinell, D. A.; Zhou, Z. H.; Huang, H. S.; Verhagen, M. F. J. M.; Adams, M. W. W.; Johnson, M. K., Electronic, magnetic, and redox properties of [MFe<sub>3</sub>S<sub>4</sub>] clusters (M = Cd, Cu, Cr) in *Pyrococcus furiosus* ferredoxin. *Inorg Chem* **1997**, *36* (25), 5740-5749.
7. Ebrahimi, K. H.; Silveira, C.; Todorovic, S., Evidence for the synthesis of an unusual high spin (S=7/2) [Cu-3Fe-4S] cluster in the radical-SAM enzyme RSAD2 (viperin). *Chem Commun* **2018**, *54* (62), 8614-8617.
8. Suess, D. L. M.; Burstel, I.; De La Paz, L.; Kuchenreuther, J. M.; Pham, C. C.; Cramer, S. P.; Swartz, J. R.; Britt, R. D., Cysteine as a ligand platform in the biosynthesis of the FeFe hydrogenase H cluster. *P Natl Acad Sci USA* **2015**, *112* (37), 11455-11460.
9. Dinis, P.; Suess, D. L. M.; Fox, S. J.; Harmer, J. E.; Driesener, R. C.; De La Paz, L.; Swartz, J. R.; Essex, J. W.; Britt, R. D.; Roach, P. L., X-ray crystallographic and EPR spectroscopic analysis of HydG, a maturase in [FeFe]-hydrogenase H-cluster assembly. *P Natl Acad Sci USA* **2015**, *112* (5), 1362-1367.

10. Nicolet, Y.; Pagnier, A.; Zeppieri, L.; Martin, L.; Amara, P.; Fontecilla-Camps, J. C., Crystal Structure of HydG from *Carboxydotherrmus hydrogenoformans*: A Trifunctional [FeFe]-Hydrogenase Maturase. *Chembiochem* **2015**, *16* (3), 397-402.
11. Rao, G. D.; Alwan, K. B.; Blackburn, N. J.; Britt, R. D., Incorporation of Ni<sup>2+</sup>, Co<sup>2+</sup>, and Selenocysteine into the Auxiliary Fe-S Cluster of the Radical SAM Enzyme HydG. *Inorg Chem* **2019**, *58* (19), 12601-12608.
12. Emptage, M. H.; Kent, T. A.; Kennedy, M. C.; Beinert, H.; Munck, E., Mossbauer and Electron-Paramagnetic-Res Studies of Activated Aconitase - Development of a Localized Valence State at a Subsite of the [4Fe-4S] Cluster on Binding of Citrate. *P Natl Acad Sci-Biol* **1983**, *80* (15), 4674-4678.
13. Kent, T. A.; Dreyer, J. L.; Kennedy, M. C.; Huynh, B. H.; Emptage, M. H.; Beinert, H.; Munck, E., Mossbauer Studies of Beef-Heart Aconitase - Evidence for Facile Interconversions of Iron-Sulfur Clusters. *P Natl Acad Sci-Biol* **1982**, *79* (4), 1096-1100.
14. Moura, J. J. G.; Moura, I.; Kent, T. A.; Lipscomb, J. D.; Huynh, B. H.; Legall, J.; Xavier, A. V.; Munck, E., Interconversions of [3Fe-3S] and [4Fe-4S] Clusters - Mossbauer and Electron-Paramagnetic Resonance Studies of *Desulfovibrio-Gigas* Ferredoxin-Ii. *J Biol Chem* **1982**, *257* (11), 6259-6267.
15. Beinert, H.; Kennedy, M. C., Engineering of Protein-Bound Iron-Sulfur Clusters - a Tool for the Study of Protein and Cluster Chemistry and Mechanism of Iron-Sulfur Enzymes. *Eur J Biochem* **1989**, *186* (1-2), 5-15.
16. Zhou, J.; Holm, R. H., Synthesis and Metal-Ion Incorporation Reactions of the Cuboidal Fe<sub>3</sub>S<sub>4</sub> Cluster. *J Am Chem Soc* **1995**, *117* (45), 11353-11354.
17. Zhou, J.; Hu, Z. G.; Munck, E.; Holm, R. H., The cuboidal Fe<sub>3</sub>S<sub>4</sub> cluster: Synthesis, stability, and geometric and electronic structures in a non-protein environment. *J Am Chem Soc* **1996**, *118* (8), 1966-1980.
18. Telser, J.; Huang, H. S.; Lee, H. I.; Adams, M. W. W.; Hoffman, B. M., Site valencies and spin coupling in the 3Fe and 4Fe (S = 1/2) clusters of *Pyrococcus furiosus* ferredoxin by Fe-57 ENDOR. *J Am Chem Soc* **1998**, *120* (5), 861-870.
19. Krebs, C.; Broderick, W. E.; Henshaw, T. F.; Broderick, J. B.; Huynh, B. H., Coordination of adenosylmethionine to a unique iron site of the [4Fe-4S] of pyruvate formate-

lyase activating enzyme: A Mossbauer spectroscopic study. *J Am Chem Soc* **2002**, *124* (6), 912-913.

20. Srisantitham, S.; Badding, E. D.; Suess, D. L. M., Postbiosynthetic modification of a precursor to the nitrogenase iron-molybdenum cofactor. *P Natl Acad Sci USA* **2021**, *118* (11).

21. Rao, G.; Pattenaude, S. A.; Alwan, K.; Blackburn, N. J.; Britt, R. D.; Rauchfuss, T. B., The binuclear cluster of [FeFe] hydrogenase is formed with sulfur donated by cysteine of an [Fe(Cys)(CO)(2)(CN)] organometallic precursor. *P Natl Acad Sci USA* **2019**, *116* (42), 20850-20855.

22. Tao, L. Z.; Pattenaude, S. A.; Joshi, S.; Begley, T. P.; Rauchfuss, T. B.; Britt, R. D., Radical SAM Enzyme HydE Generates Adenosylated Fe(I) Intermediates En Route to the [FeFe]-Hydrogenase Catalytic H-Cluster. *J Am Chem Soc* **2020**, *142* (24), 10841-10848.

23. Rohac, R.; Martin, L.; Liu, L.; Basu, D.; Tao, L. Z.; Britt, R. D.; Rauchfuss, T. B.; Nicolet, Y., Crystal Structure of the [FeFe]-Hydrogenase Maturase HydE Bound to Complex-B. *J Am Chem Soc* **2021**, *143* (22), 8499-8508.

24. Hsu, H. F.; Koch, S. A.; Popescu, C. V.; Munck, E., Chemistry of iron thiolate complexes with CN<sup>-</sup> and CO. Models for the [Fe(CO)(CN)(2)] structural unit in Ni-Fe hydrogenase enzymes. *J Am Chem Soc* **1997**, *119* (35), 8371-8372.

25. Li, B.; Liu, T.; Popescu, C. V.; Bilko, A.; Darensbourg, M. Y., Synthesis and Mossbauer characterization of octahedral iron(II) carbonyl complexes FeI<sub>2</sub>(CO)<sub>3</sub>L and FeI<sub>2</sub>(CO)<sub>2</sub>L<sub>2</sub>: developing models of the [Fe]-H(2)ase active site. *Inorg Chem* **2009**, *48* (23), 11283-9.

26. Kuchenreuther, J. M.; Myers, W. K.; Suess, D. L. M.; Stich, T. A.; Pelmeshnikov, V.; Shiigi, S. A.; Cramer, S. P.; Swartz, J. R.; Britt, R. D.; George, S. J., The HydG Enzyme Generates an Fe(CO)(2)(CN) Synthron in Assembly of the FeFe Hydrogenase H-Cluster. *Science* **2014**, *343* (6169), 424-427.

27. Rao, G. D.; Tao, L. Z.; Suess, D. L. M.; Britt, R. D., A [4Fe-4S]-Fe(CO)(CN)-L-cysteine intermediate is the first organometallic precursor in [FeFe] hydrogenase H-cluster bioassembly. *Nat Chem* **2018**, *10* (5), 555-560.

28. Parish, R. V.; Koerner von Gustorf, E. A.; Grevels, F. W.; Fischler, I., *Mössbauer Spectroscopy. The Organic Chemistry of Iron Volume 1. Organometallic Chemistry Series*. Academic Press: London, England, 1978.

29. Gutlich, P.; Bill, E.; Trautwein, A. X., Mossbauer Spectroscopy and Transition Metal Chemistry: Fundamentals and Applications. *Mossbauer Spectroscopy and Transition Metal Chemistry: Fundamentals and Applications* **2011**, 1-568.
30. Winter, G.; Thompson, D. W.; Loehe, J. R., *Iron(II) Halides*. John Wiley & Sons, Ltd: 2007; Vol. 14.
31. Brennessel, W. W.; Jilek, R. E.; Ellis, J. E., Bis(1,2,3,4-eta(4)-anthracene)ferrate(1-): A paramagnetic homoleptic polyarene transition-metal anion. *Angew Chem Int Edit* **2007**, *46* (32), 6132-6136.
32. Gilbert-Wilson, R.; Siebel, J. F.; Adamska-Venkatesh, A.; Pham, C. C.; Reijerse, E.; Wang, H. X.; Cramer, S. P.; Lubitz, W.; Rauchfuss, T. B., Spectroscopic Investigations of [FeFe] Hydrogenase Maturated with [Fe-57(2)(adt)(CN)(2)(CO)(4)](2-). *J Am Chem Soc* **2015**, *137* (28), 8998-9005.
33. Bockman, T. M.; Cho, H. C.; Kochi, J. K., Charge-Transfer Crystals of Octacarbonyldiferrate - Solid-State Structure and Oxidation-Reduction of an Iron-Iron-Bonded Electron-Donor. *Organometallics* **1995**, *14* (11), 5221-5231.
34. Bernard, B.; Daniels, L.; Hance, R.; Hutchinson, B., Facile Synthesis of Fe-57 (Co)5. *Syn React Inorg Met* **1980**, *10* (1), 1-7.
35. Lazar, K.; Matusek, K.; Mink, J.; Dobos, S.; Guzzi, L.; Viziorosz, A.; Marko, L.; Reiff, W. M., Spectroscopic and Catalytic Study on Metal-Carbonyl Clusters Supported on Cab-O-Sil .1. Impregnation and Decomposition of Fe<sub>3</sub>(Co)<sub>12</sub>. *J Catal* **1984**, *87* (1), 163-178.
36. DuBois, D. L.; DuBois, M. R.; Ringenberg, M. R.; Rauchfuss, T. B., *Bio-Inspired Iron and Nickel Complexes*. John Wiley & Sons, Ltd: 2010; Vol. 35, p 129-147.

## Chapter 5

### Electron Paramagnetic Resonance (EPR) characterization of Actinide Compounds and Free Radicals

#### 5.1. Introduction to EPR of heavy elements

On the periodic table Lanthanides occupy atomic numbers  $Z = 58$  through  $Z = 71$ , generally having the electronic ground state  $[\text{Xe}]4f^n5s^25p^6$  (where  $n$  varies between 1 and 14). The paramagnetism of Lanthanides arises from the  $4f^n$  subshell, giving its unique magnetic properties. The  $4f$  subshell is physically more *internal*, exposing the electrons in this subshell to high effective nuclear charge, which increases spin-orbit coupling and hyperfine interactions.<sup>1</sup> This *internal* positioning also causes the electrons to interact less with ligands if the Lanthanide nuclei is part of a complex. The following row on the periodic table includes Actinides which occupy atomic numbers  $Z = 90$  through  $Z = 103$ , typically having the electronic ground state  $[\text{Rn}]5f^n6s^26p^6$ . It is important to note there are deviations from these general electronic ground states for specific elements in the Lanthanide and Actinide series. Actinides contain similar magnetic properties to Lanthanides, though the  $5f$  orbital is less *internal*. The core electrons in Actinides shield  $5f$  electrons to a greater extent than  $4f$  orbitals, reducing the effective nuclear charge and making them easier to oxidize. The  $5f$  subshell being less *internal* also interacts more strongly with ligands when part of a complex. These properties for unpaired electrons in Lanthanides and Actinides determine the observable transitions in magnetic spectra such as EPR and susceptibility measurements.

Lanthanides, and in some cases Actinide compound's, magnetic characteristics are well described by  $(L,S)$  Russell-Saunders coupling.<sup>2</sup> Here the  $(L,S)$ -coupling energy levels can be identified by the total angular momentum  $\mathbf{J} = \mathbf{L} + \mathbf{S}$  of the ion. The value of  $J$  varies from  $J_{\min} =$

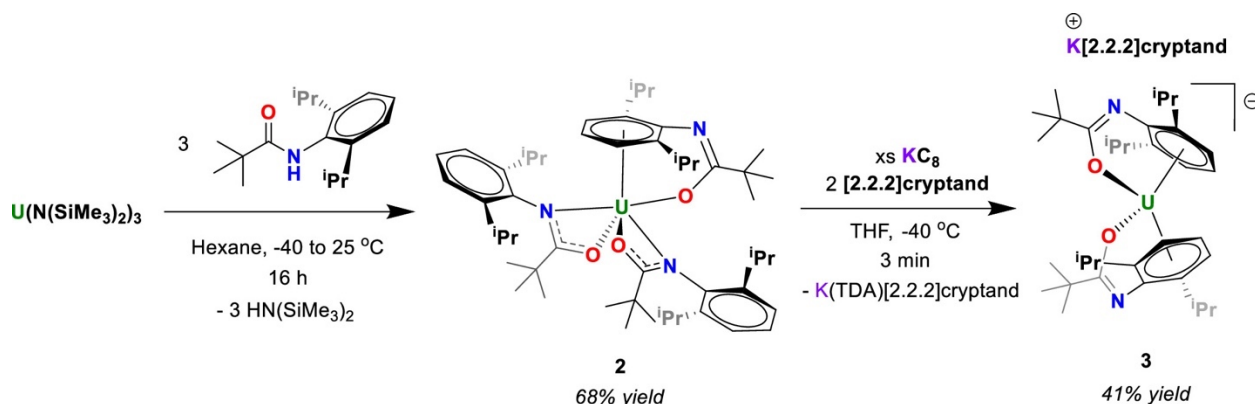
$|L-S|$  to  $J_{\max} = |L+S|$ . Each value of  $J$  is associated with a  $(L,S,J)$  multiplet, which has  $(2J+1)$  states, and the magnetic moment can be written as  $\mu = -g_{L\text{and}S}\beta \mathbf{J}$ .

## 5.2. Uranium(II) that acts like a Uranium (I) Synthron Introduction

Uranium is the heaviest Actinide that can be described by the  $(L,S)$  coupling scheme.<sup>3</sup> Uranium commonly forms ions with the oxidation states +3, +4, +5, and +6 but only recently has it been isolated in a molecular form with a +2 oxidation state. Uranium (II) can be described with  $S = 2$ ,  $L = 6$ ,  $J = 4$  and a  $^5I_4$  ground state term. Depending on the supporting ligands and molecular symmetry, Uranium (II) can be observed with a  $[Rn]5f^4$  ground state or a  $[Rn]5f^36d^1$  ground state as determined by EPR spectroscopy, magnetic measurements, and DFT calculations.<sup>4,5</sup> Uranium (II) complexes produced to date have been supported by cyclopentadienes<sup>6-9</sup>, amides<sup>9,10</sup>, and aryloxides<sup>11,12</sup>. Though overall Uranium (II) complexes remain rare due to their instability, with many of their reactive properties still being unknown. It was the goal then of Straub et al to introduce a ligand system that could act as a  $\sigma$ -donor and  $\delta$ -acceptor, facilitating the stabilization of structurally related uranium complexes across multiple oxidation states to better understand single and multielectron reactivity. Straub et al chose to use an amidate ligand with an N-aryl substituent, a ligand capable of binding to the metal center through a tethered arene moiety in addition to N- and O-donor sites.<sup>13</sup> This work allowed for the isolation of new actinide arene complexes, including a U(II) bis(arene) complex containing a monoreduced arene ligand. The following work was completed as a collaboration, with compounds produced at UC Berkeley and the EPR spectroscopy completed at UC Davis.



### 5.2.1. Uranium(II) that acts like a Uranium (I) Synthron



**Scheme 5.2.1.** Synthesis of the Uranium Mono(arene) Complex  $\text{U}(\text{TDA})_3$  (**2**) and the Uranium Bis(Arene) Complex  $[\text{K}[2.2.2]\text{cryptand}][\text{U}(\text{TDA})_2]$  (**3**) by two-electron reduction of **2**.<sup>14</sup>

The following compounds were prepared at UC Berkeley by Mark Straub, sealed in EPR tubes with glass wool and grease under nitrogen atmosphere and frozen in liquid nitrogen. Previously published results show that reduction of an eight-coordinate U(IV) amidate  $\text{U}(\text{TDA})_4$  with  $\text{KC}_8$ , in the presence of 18-crown-6, gives a four-coordinate U(III) anion  $[\text{K}(18\text{-crown-6})][\text{U}(\text{TDA})_4]$  with all four amidate ligands undergoing a change in coordination mode from  $k^2\text{-O,N}$  to  $k^1\text{-O}$  upon reduction.<sup>15</sup> Using this U(III) complex as starting material, it was speculated that lower valent states should be accessible. Starting with  $\text{U}(\text{N}(\text{SiMe}_3)_2)_3$ , protonolysis by 3 equivalents of  $\text{H}(\text{TDA})$  gives a dark purple product **2** (Scheme 5.2.1). Addition of excess  $\text{KC}_8$  and [2.2.2]cryptand to a THF solution of **2** at  $-40^\circ\text{C}$  resulted in a color change from dark purple to dark brown, the product compound  $[\text{K}[2.2.2]\text{cryptand}][\text{U}(\text{TDA})_2]$  (**3**).

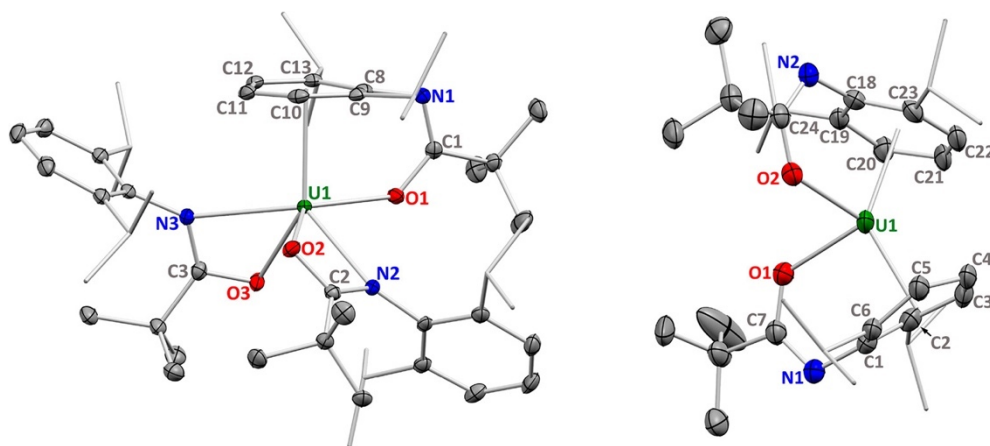


**Figure 5.2.1.** X-ray crystal structures of **2** (left) and **3** (right) with 50% probability ellipsoids.

Hydrogen atoms and [K[2.2.2]cryptand]<sup>+</sup> are omitted, and isopropyl groups are shown as capped sticks.<sup>14</sup>

The crystal structure of **2** (**Figure 5.2.1.**) shows that the six carbons of the bound arene adopt a planar geometry with U-C bond distances between 2.899(2) to 2.988(2) Å and C-C bond lengths of 1.390(3) to 1.423(3) Å. The uranium-centroid distance of 2.602(2) Å is consistent with Uranium (III) arenes.<sup>16</sup> Torsion angles for the bound arene formed by the C-C bonds on opposite sides of the arene, range from 2.5(2)° to 5.0(2)° which suggests that no significant reduced character is present. U-O and U-N distances of 2.310(2) to 2.347(2) Å and 2.581(2) to 2.652(2) Å, respectively, for the amidates in **2** are similar to corresponding distances for **k**<sup>2</sup>-O,N and **k**<sup>1</sup>-O amidates in U(TDA)<sub>4</sub> and 1-crown.<sup>15</sup>

The crystal structure of **3** (**Figure 5.2.1.**) shows that [U(TDA)<sub>2</sub>]<sup>+</sup> possesses approximately C<sub>2</sub> symmetry in the solid state; though of the two arenes, which are bound in an η<sup>6</sup> fashion to the uranium center, one (comprised of carbon atoms C1-C6) is slightly distorted. C2 and C5 have U-C distances of 2.595(6) and 2.604(5) Å, respectively, whereas the remaining carbons in that arene are 0.12 Å farther from the uranium center. Additionally, the C1-C6 and C3-C4 bonds are

slightly shortened relative to the remaining arene C-C bonds, which have torsion angles of 11.5(4)° and 15.5(4)°. These values are consistent with the typical range for a monoreduced arene ligand.<sup>17</sup> In contrast to this, the other bound arene (C18-C23) adopts a planar geometry, with U-C distances of 2.706(6) to 2.763(6) Å and C-C bond lengths of 1.389(7) to 1.440(6) Å. The torsion angles in this arene are minimal, suggesting that this ligand possesses no significant reduced character in the solid state. U-centroid distances are 2.274(6) and 2.334(6) Å for the distorted and undistorted arenes, respectively; this contraction of ~0.3 Å from the U-centroid distance of **2** is consistent with increased U-arene back-bonding upon reduction.<sup>10</sup>

### 5.2.2. EPR of Uranium(II) that acts like a Uranium (I) Synthron

EPR spectroscopy was performed to identify the oxidation state of uranium in **2** and **3**. Continuous wave (CW) X-band EPR of a powdered sample of **2** shows a rhombic system with effective *g*-values of [3.605 1.264 0.626] giving a  $g_{\text{iso}} = 2.24$  (**Figure 5.2.2.1. and 5.2.2.3.**). These *g*-values are consistent with other uranium (III) complexes previously reported with large orbital momentum.<sup>18-20</sup> The splitting in the EPR spectrum of **2** is too large to be accounted for by nuclear hyperfine interactions, and is likely the result of dipolar and/or exchange interactions between molecules in the solid state. Measurements on solution samples did not exhibit such splitting, suggesting that it is intermolecular in origin.

The EPR spectrum of **3** features a sharp, intense peak centered at 330 mT (**Figures 5.2.2.2. and 5.2.2.4.**). This signal can be well simulated as an  $S = 1/2$  spin system with  $g = [2.042 2.021 2.013]$ . This signal persists at temperatures as high as 40 K (**Figure 5.2.2.5.**), indicating that the spin relaxation time is relatively long, which is characteristic of an organic radical. We attribute this signal to an arene ligand radical in **3**. The overall change in signal upon reduction of **2** to give **3** suggests that the uranium center is reduced to a nonmagnetic ( $5f^4$ ) ground state, with an EPR-

silent integer spin,  $S = 2$ . No other signals can be seen in **3** by EPR in the X-band, including an  $S = 3/2$  signal from a coupled metal-ligand system. Parallel-mode X-band CW-EPR of **3** was unable to reveal any integer spin signals that could be attributed to the uranium center, likely due to the low symmetry of **3** (**Figure 5.2.2.4**). The behavior of the Uranium (II) ion in **3** (i.e., EPR nonactive) is fully consistent with the discovery and characterization of the related Uranium (II) arene complexes reported by Odom and co-workers and by Meyer and co-workers. The absence of transitions between spin states at 5 K indicates that the low-lying excited states are well separated, such that only a signal from the ligand radical is observed.

Compound **3** was additionally probed by high-field, high-frequency EPR at 130 GHz. An echo-detected field-sweep EPR spectrum of **3** measured at 4.5 K features an almost-axial signal arising from an  $S = 1/2$  spin that is well simulated by  $g = [2.042\ 2.022\ 2.019]$  (**Figure 5.2.2.6**), in close agreement with  $g$  parameters of the radical ligand extracted from the X-band spectrum. The deviation of the  $g$  factor from the free-electron  $g$  value ( $g_e = 2.002$ ) indicates anisotropy, confirming the proximity of the radical to the heavy uranium center bearing significant spin-orbit coupling.<sup>21</sup> No uranium-based signals were observed in echo-detected EPR at 4.5 K using 130 GHz irradiation, precluding further analysis of the electronic structure of **3**. Overall, EPR measurements indicate that the two-electron reduction of **2** by  $\text{KC}_8$  results in a one-electron reduction of the metal center to give an integer spin  $S = 2$  uranium(II) center and a one-electron reduction of the ligand to give an  $S = 1/2$  arene radical, and that the Uranium (II) atom and arene are decoupled in the ground state.

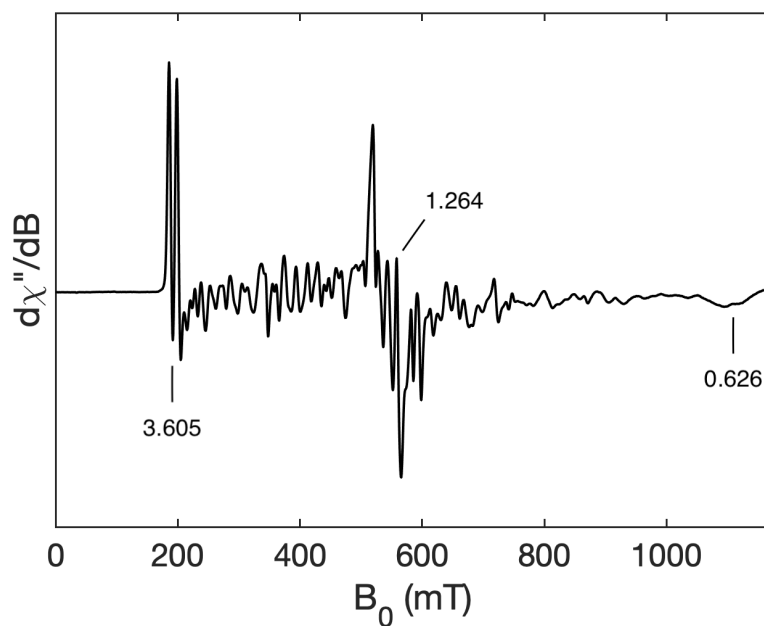


**Figure 5.2.2.1.** X-band (9.7 GHz) CW-EPR spectrum of a solid sample of **2** in perpendicular mode.

Conditions: temperature, 5K; microwave power, 0.2 mW; modulation amplitude 0.8 mT.

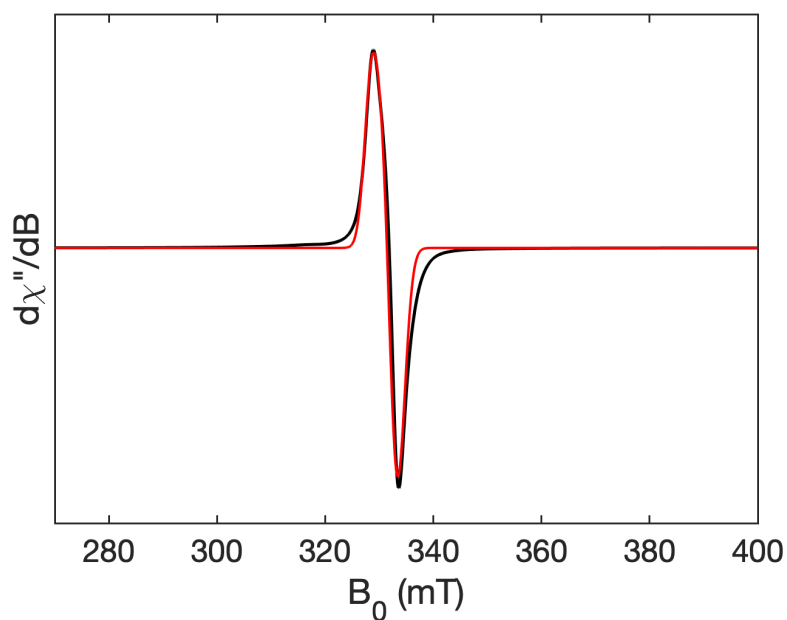


**Figure 5.2.2.2.** X-band (9.4 GHz) CW-EPR spectrum of a solid sample of **3** (black trace) in perpendicular mode. Simulated (red trace) with  $S = 1/2$  spin system,  $g = [2.042 \ 2.021 \ 2.013]$ , and  $g\text{Strain} = [0.019 \ 0.022 \ 0.021]$ . Conditions: temperature = 5K; microwave power = 0.2 mW; modulation amplitude = 0.5 mT.

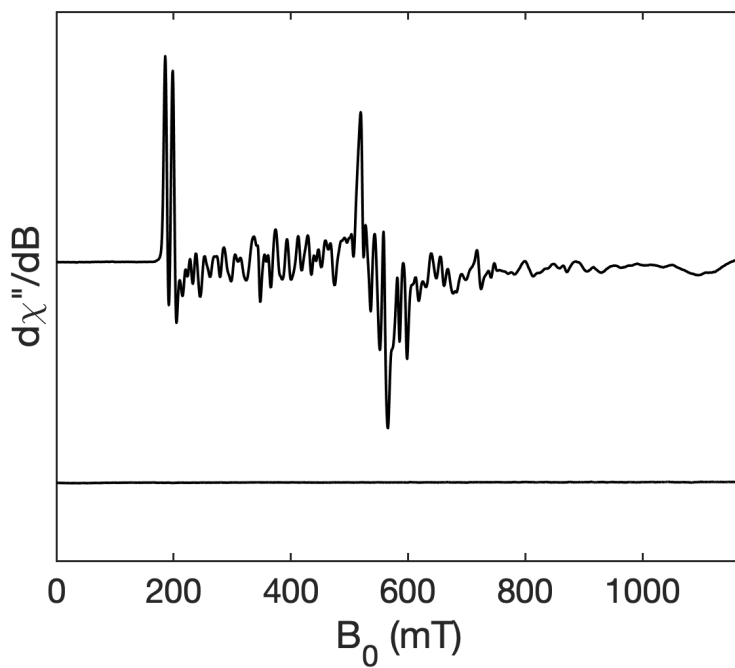


**Figure 5.2.2.3.** (Top) X-band (9.7 GHz) CW-EPR in perpendicular mode of **2**. (Bottom) X-band (9.4 GHz) CW-EPR in parallel mode of **2**. Conditions: temperature, 5K; microwave power, 0.2 mW; modulation amplitude 0.8 mT.

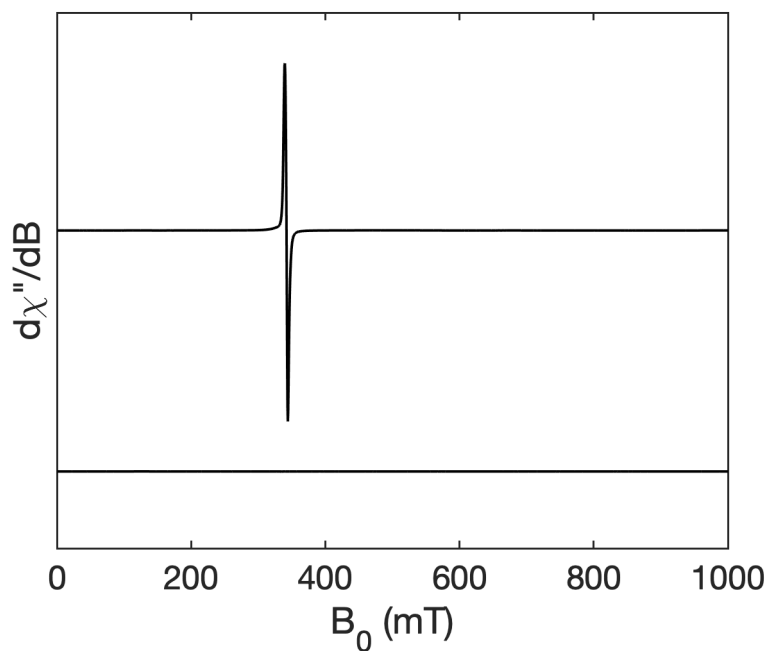


**Figure 5.2.2.4.** (Top) X-band (9.7 GHz) CW-EPR in perpendicular mode of **3**. (Bottom) X-band (9.4 GHz) CW-EPR in parallel mode of **3**. Conditions: temperature, 5K; microwave power, 0.2 mW; modulation amplitude, 0.5 mT.



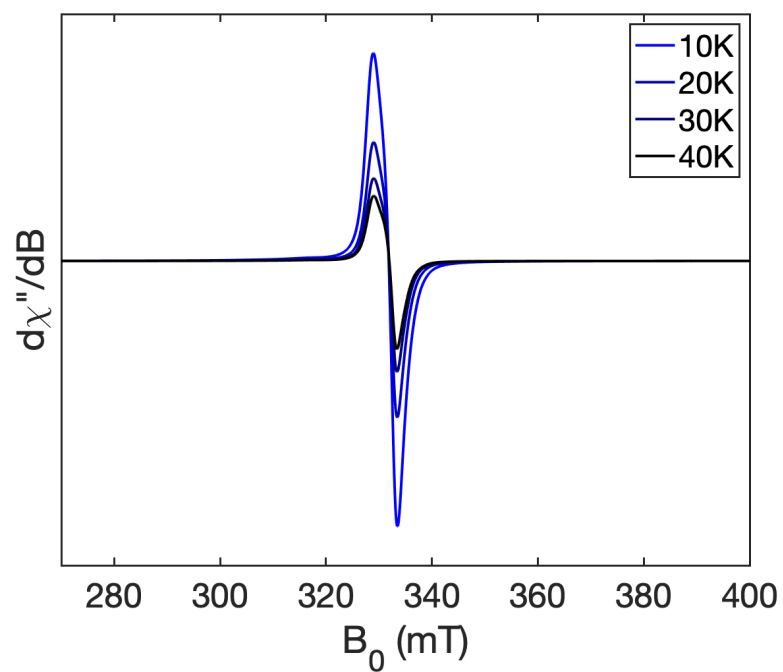


**Figure 5.2.2.5.** X-band (9.4 GHz) CW-EPR in perpendicular mode of **3**. Conditions: temperature, 10K, 20K, 30K, 40K; microwave power, 0.2 mW; modulation amplitude, 0.5 mT.

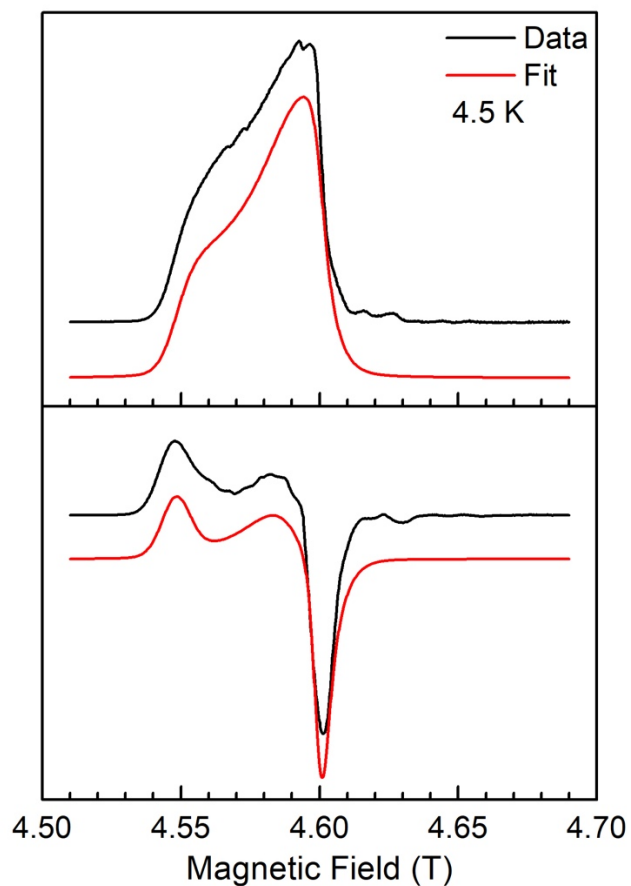


**Figure 5.2.2.6.** (Top) Field-swept echo-detected EPR spectrum of **3** measured at 130 GHz, 4.5 K (black line). Red line depicts simulation using  $S = 1/2$ ,  $g = [2.042 \ 2.022 \ 2.019]$ ,  $g\text{Strain} = [0.005 \ 0.010 \ 0.002]$ . (Bottom) Derivative-like spectrum generated from pseudo-modulation of the echo-detected spectrum (black line) and its corresponding simulation (red line). Pseudo-modulation amplitude, 1 mT.

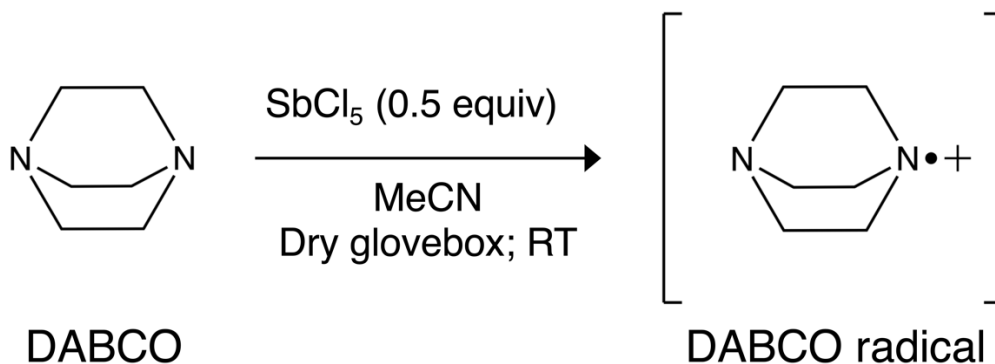
### 5.2.3. EPR of Uranium(II) that acts like a Uranium (I) Synthone Discussion

Overall, the work of Straub et al displayed the successful synthesis of uranium bis(amidate) complex with two tethered arene ligands (**3**) by two-electron reduction of the amidate-supported Uranium (III) mono(arene) **2**. Complex **3** was characterized to be a Uranium (II) complex with an overall monoreduced arene ligand framework based on strong evidence from crystal structure data and EPR spectroscopy. Additional evidence not discussed here included SQUID magnetometry and quantum chemical calculations.<sup>14</sup>

### 5.3. Introduction to EPR Spectroscopy of Free Radicals

For many radicals in solution, their half-life is long enough to allow for their study by CW EPR even at room temperature. These transient radicals can also be studied by rapid freeze quench along the reaction pathway. The unpaired electron on the free radical molecule will likely interact with nuclei that contain nuclear spin  $I = \frac{1}{2}$ , such as  $^1\text{H}$ ,  $^{13}\text{C}$  or  $I = 1$  such as  $^{14}\text{N}$  (**Section 1.1.2**). Therefore, analyzing the hyperfine pattern of the EPR spectrum can serve to locate the spin population on the molecule. In the case where the unpaired electron interacts with two equivalent nuclei of spin of  $I_1 = I_2 = \frac{1}{2}$ , the number of ways the three possible values of  $\Delta E$  can be obtained is (1:2:1). These numbers determine the relative intensities of the three hyperfine lines in the spectrum. As the number of nuclei ( $n$ ) increases with nuclear spin ( $I$ ) the multiplet seen can be predicted by  $2nI + 1$ . This relationship for a growing number of hyperfine lines is known as “Pascal’s triangle” and is useful in predicting splitting patterns for simple free radicals with equivalent nuclei (**Figure 5.3**).<sup>22</sup> Although many free radicals contain inequivalent nuclei making the relationship less straight forward.

### 5.3.1. Generating DABCO Free Radicals



**Scheme 5.3.1.** Generation of free DABCO radical(s)

Heterocyclic structures, including Piperazine, are highly sought after in small molecule design and oligomers.<sup>23-27</sup> Piperazine is often incorporated into small molecule drugs<sup>28-33</sup>, including anticancer agents.<sup>34,35</sup> Piperazine is also widely built into materials with polymer chemistry. The utility of this functional group motivated the work by Baldauf et al to seek out efficient synthetic routes to generating this piperazine moiety. The approach chosen would be to cleave DABCO (1,4-diazobicyclo[2.2.2]octane) molecules (**Scheme 5.3.1.**), to eventually give the resulting piperazine structure. Initiated by oxidation, DABCO is capable of two types of bond cleavage: breaking the weaker C-N bond or the more stable C-C  $\sigma$ -bond. Oxidation of DABCO into a DABCO $\bullet+$  radical followed by fragmentation was first demonstrated using ClO<sub>2</sub> and HOCl as oxidizing agents.<sup>36</sup> The first evidence of DABCO $\bullet+$  radicals in solution was reported by McKinney and Geske in 1965, showing the unexpected delocalization of the radical across the whole molecule and the two nitrogen atoms.<sup>37</sup> Hoffman and others have shown that this unlikely delocalization could be the result of “pseudo-conjugation” from quick cleavage and reformation of one of the ethylene bridges.<sup>38-43</sup> In the work by Baldauf et al, SbCl<sub>5</sub> was used as an oxidant under anaerobic conditions to generate transient DABCO $\bullet+$  radicals on path towards products containing piperazine functional groups.

### 5.3.2. X-band CW EPR of DABCO Free Radicals

EPR was performed to observe evidence of any paramagnetic intermediates along the reaction pathway. A sample of DABCO in dry acetonitrile was frozen shortly (within 10 seconds) after the addition of  $\text{SbCl}_5$ , having a visible deep red color. The X-band CW EPR spectrum of this sample at 100K (Figure 6A, top trace) displays a signal centered at  $g = 2.009$ , indicating the presence of an organic radical species. Cryo-annealing of the EPR sample at 228 K over a period of 10s leads to gradually decreased EPR signal intensity (**Figure 5.3.2.**), accompanied by the disappearance of the dark red color. The final reaction mixture shows a faint yellow color and has barely observable EPR features. These CW-EPR spectra recorded have a strong resemblance to those previously published by Shida et al. (1978)<sup>43</sup>, in which frozen DABCO samples were irradiated with  $\gamma$ -rays to produce cation radicals.

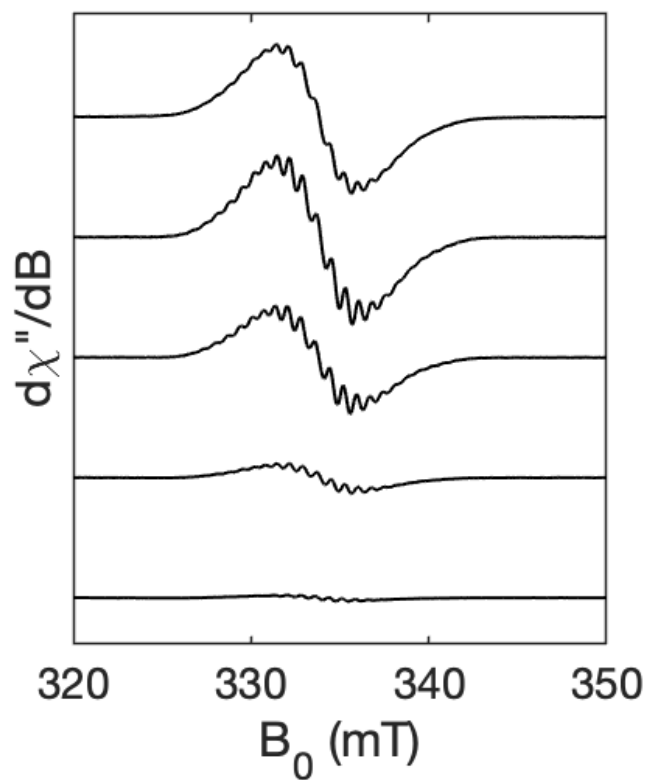


**Figure 5.3.2.** X-band CW EPR of DABCO with  $\text{SbCl}_5$  at various time points along the reaction pathway, from top to bottom. The parameters for X-band CW EPR are: temperature, 100K; microwave power, 0.2 mW; modulation amplitude, 0.2 mT.

### 5.3.3. Pulsed ENDOR of DABCO Radical Intermediate Species

Q-band Davies ENDOR was used to assign the source and strength of the hyperfine observed in the X-band CW spectra. The reaction sample quenched at 10 s shows only one set of near isotropic  $^1\text{H}$  hyperfine coupling, simulated with a  $^1\text{H} = 21.5$  MHz (**Figure 5.3.3.1**). This reaction was a pale yellow when frozen. The reaction sample quenched earlier in the reaction at 5 s shows additional ENDOR features that can be simulated with two additional sets of near isotropic  $^1\text{H}$  hyperfine couplings of 26 and 15 MHz with equal intensities (**Figure 5.3.3.2**). This reaction, unlike the previous sample, was a mixture of deep red and orange. We rationalize that these ENDOR signals correspond to two different radical species, one containing two chemically different  $^1\text{H}$  environments formed at the beginning of the reaction pathway, and the other one with a uniform  $^1\text{H}$  environment and appearing at a later time point.

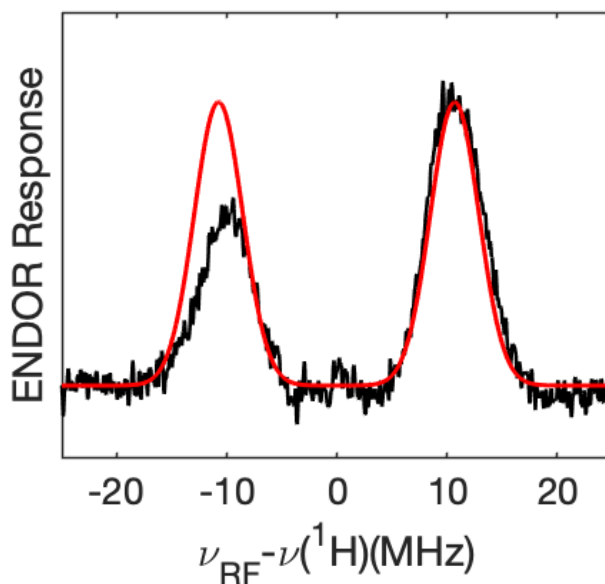


**Figure 5.3.3.1.** Q-band Davies-ENDOR of DABCO reaction mixture quenched at 10 seconds showing one  $^1\text{H}$  hyperfine coupling. Parameters for Q-band Davies-ENDOR measurements are temperature, 10K;  $\pi/2$ , 12 ns;  $\tau = 300$  ns; inversion pulse, 80 ns; radio frequency pulse, 15  $\mu\text{s}$ .

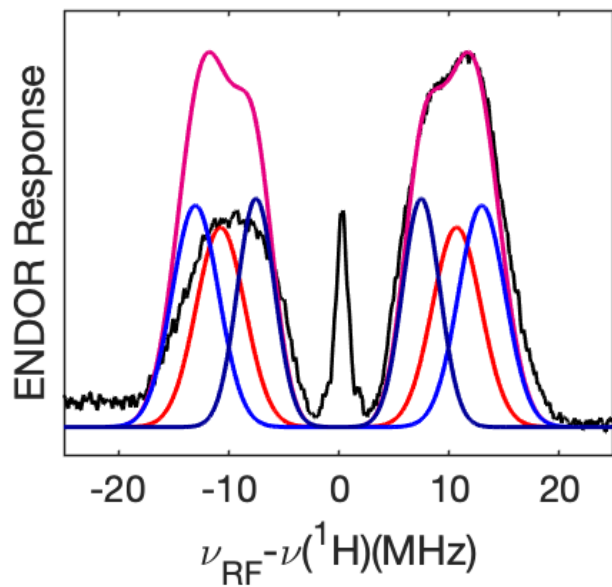


**Figure 5.3.3.2.** Q-band Davies-ENDOR of DABCO reaction mixture quenched at 5 seconds showing three sets of  $^1\text{H}$  hyperfine couplings. Parameters for Q-band Davies-ENDOR measurements are temperature, 10K;  $\pi/2$ , 12 ns;  $\tau = 300$  ns; inversion pulse, 80 ns; radio frequency pulse, 15  $\mu\text{s}$ .



#### 5.3.4. Simulating X-band CW EPR of DABCO Radicals

Indeed, the CW EPR spectra can be simulated using two proposed species and their ENDOR-detected  $^1\text{H}$  hyperfine values (**Figure 5.3.4.**). The first radical species contains equal hyperfine contribution from twelve  $^1\text{H}$  ( $a = 21.5$  MHz) and two  $^{14}\text{N}$  ( $a = 22$  MHz) nuclei. On the contrary, the second radical species has contributions from two sets of  $6\times^1\text{H}$  with  $a = 26$  and  $15$  MHz, respectively, and 2 distinct  $^{14}\text{N}$  nuclei with  $a = 48$  and  $4$  MHz, respectively. In summary, the EPR data suggests that propagation of the reaction pathway sees the existence of at least two DABCO $^+$  organic radicals: one that is nearly delocalized (**Figure 5.3.3.1., Figure 5.3.3.2., Figure 5.3.4.**) with equal hyperfine values and the second localized close to one of the two nitrogen atoms on the molecule (**Figure 5.3.3.2., Figure 5.3.4.**).

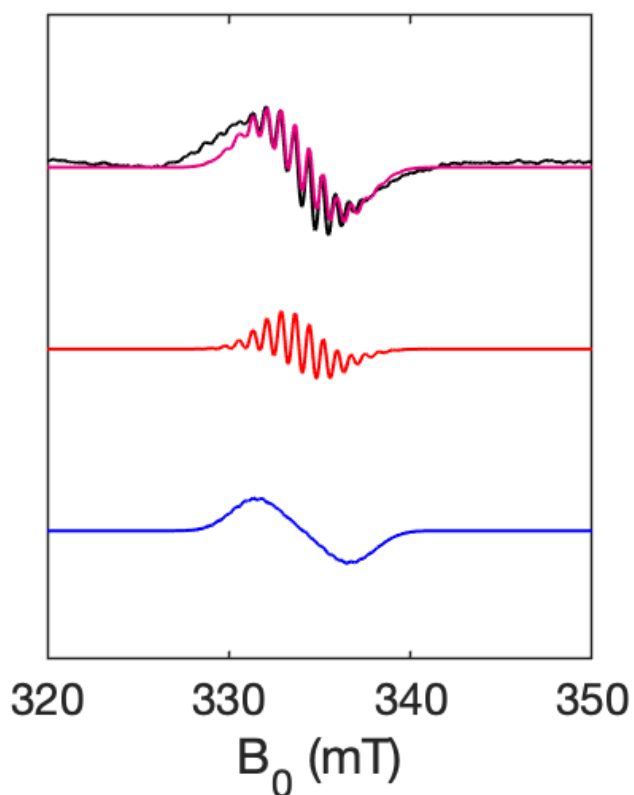


**Figure 5.3.4.** Top: CW EPR of the DABCO<sup>+</sup> radical species (black trace) and total simulation (magenta trace). Middle: Delocalized DABCO<sup>+</sup> radical simulation  $g = [2.007, 1.997]$ ,  $12 \times {}^1\text{H } A = [21.5, 21.5]$  MHz,  $2 \times {}^{14}\text{N } A = [22, 22]$  MHz (red trace). Bottom: Localized DABCO<sup>+</sup> radical simulation  $g = [2.008, 1.999]$ ,  $6 \times {}^1\text{H } A = [26, 26]$  MHz,  $6 \times {}^1\text{H } A = [15, 15]$  MHz,  $1 \times {}^{14}\text{N } A = [48, 48]$  MHz,  $1 \times {}^{14}\text{N } A = [4, 4]$  MHz (blue trace). The parameters for X-band CW EPR are: temperature, 100K; microwave power, 0.2 mW; modulation amplitude, 0.2 mT.

#### 5.4. Materials and Methods

EPR spectroscopy was performed in the CalEPR center in the Department of Chemistry, University of California at Davis. X-band continuous wave (CW) EPR spectroscopy was carried out on the Bruker Biospin EleXsys E500 spectrometer with a super high Q resonator (ER4122SHQE) in perpendicular mode and dual mode cavity (ER4116DM) in both perpendicular and parallel modes. All CW-EPR spectra were recorded on solid samples under slow-passage, non-saturating conditions. Spectrometer settings were: conversion time, 40 ms; modulation amplitude, 0.5 – 0.8 mT; modulation frequency, 100 kHz; and other settings as indicated in figure captions. High-field, high-frequency EPR spectrum was measured at a temperature of 4.5 K using a home-built 130 GHz EPR spectrometer equipped with an Oxford-CF935 liquid helium cryostat as described previously.<sup>5</sup> Magnetic field-swept echo-detected EPR spectrum was acquired using the Hahn echo pulse sequence:  $\pi/2 - \tau - \pi - \text{echo}$ , with a  $\pi/2$  pulse duration of 40 ns,  $\tau$  of 250 ns,  $\pi$  pulse of 80 ns. Simulations of the EPR data were performed using EasySpin toolbox<sup>6</sup> in Matlab software.

## 5.5. References

1. Bertrand, P., *Electron Paramagnetic Spectroscopy: Fundamentals*. Springer International Publishing: 2020.
2. Russell, H. N.; Saunders, F. A., New regularities in the spectra of the alkaline earths. *Astrophys J* **1925**, *61* (1), 38-69.
3. Moore, K. T.; van der Laan, G., Nature of the 5f states in actinide metals. *Rev Mod Phys* **2009**, *81* (1), 235-298.
4. MacDonald, M. R.; Fieser, M. E.; Bates, J. E.; Ziller, J. W.; Furche, F.; Evans, W. J., Identification of the +2 Oxidation State for Uranium in a Crystalline Molecular Complex, [K(2.2.2-Cryptand)][(C<sub>5</sub>H<sub>4</sub>SiMe<sub>3</sub>)<sub>3</sub>U]. *J Am Chem Soc* **2013**, *135* (36), 13310-13313.
5. Moehring, S. A.; Evans, W. J., Evaluating Electron-Transfer Reactivity of Complexes of Actinides in +2 and +3 Oxidation States by using EPR Spectroscopy. *Chem-Eur J* **2020**, *26* (7), 1530-1534.
6. Huh, D. N.; Ziller, J. W.; Evans, W. J., Chelate-Free Synthesis of the U(II) Complex, [(C<sub>5</sub>H<sub>3</sub>(SiMe<sub>3</sub>)<sub>2</sub>)<sub>3</sub>U](1-), Using Li and Cs Reductants and Comparative Studies of La(II) and Ce(II) Analogs. *Inorg Chem* **2018**, *57* (18), 11809-11814.
7. Windorff, C. J.; MacDonald, M. R.; Meihaus, K. R.; Ziller, J. W.; Long, J. R.; Evans, W. J., Expanding the Chemistry of Molecular U<sup>2+</sup> Complexes: Synthesis, Characterization, and Reactivity of the {[C<sub>5</sub>H<sub>3</sub>(SiMe<sub>3</sub>)<sub>2</sub>]<sub>3</sub>U}(-) Anion. *Chem-Eur J* **2016**, *22* (2), 772-782.
8. Guo, F. S.; Tsoureas, N.; Huang, G. Z.; Tong, M. L.; Mansikkamaki, A.; Layfield, R. A., Isolation of a Perfectly Linear Uranium(II) Metallocene. *Angew Chem Int Edit* **2020**, *59* (6), 2299-2303.
9. Ryan, A. J.; Angadol, M. A.; Ziller, J. W.; Evans, W. J., Isolation of U(II) compounds using strong donor ligands, C<sub>5</sub>Me<sub>4</sub>H and N(SiMe<sub>3</sub>)<sub>2</sub>, including a three-coordinate U(II) complex. *Chem Commun* **2019**, *55* (16), 2325-2327.
10. Billow, B. S.; Livesay, B. N.; Mokhtarzadeh, C. C.; McCracken, J.; Shores, M. P.; Boncella, J. M.; Odom, A. L., Synthesis and Characterization of a Neutral U(II) Arene Sandwich Complex. *J Am Chem Soc* **2018**, *140* (50), 17369-17373.

11. La Pierre, H. S.; Scheurer, A.; Heinemann, F. W.; Hieringer, W.; Meyer, K., Synthesis and Characterization of a Uranium(II) Monoarene Complex Supported by delta Backbonding. *Angew Chem Int Edit* **2014**, *53* (28), 7158-7162.
12. La Pierre, H. S.; Kameo, H.; Halter, D. P.; Heinemann, F. W.; Meyer, K., Coordination and Redox Isomerization in the Reduction of a Uranium(III) Monoarene Complex. *Angew Chem Int Edit* **2014**, *53* (28), 7154-7157.
13. Hagadorn, J. R.; Arnold, J., Tethered bis-amidates as supporting ligands: A concerted elimination/sigma-pi rearrangement reaction forming an unusual titanium arene complex. *Angew Chem Int Edit* **1998**, *37* (12), 1729-1731.
14. Straub, M. D.; Ouellette, E. T.; Boreen, M. A.; Britt, R. D.; Chakarawet, K.; Douair, I.; Gould, C. A.; Maron, L.; Del Rosal, I.; Villarreal, D.; Minasian, S. G.; Arnold, J., A Uranium(II) Arene Complex That Acts as a Uranium(I) Synthon. *J Am Chem Soc* **2021**, *143* (47), 19748-19760.
15. Straub, M. D.; Hohloch, S.; Minasian, S. G.; Arnold, J., Homoleptic U(III) and U(IV) amidate complexes. *Dalton T* **2018**, *47* (6), 1772-1776.
16. La Pierre, H. S.; Meyer, K., Activation of Small Molecules by Molecular Uranium Complexes. *Prog Inorg Chem* **2014**, *58*, 303-415.
17. Rosokha, S. V.; Kochi, J. K., Charge-Transfer Effects on Arene Structure and Reactivity. In *Modern Arene Chemistry* Astruc, D., Ed. Wiley 2002; pp 435-478.
18. Formanuk, A.; Ariciu, A. M.; Ortu, F.; Beekmeyer, R.; Kerridge, A.; Tuna, F.; McInnes, E. J. L.; Mills, D. P., Actinide covalency measured by pulsed electron paramagnetic resonance spectroscopy. *Nat Chem* **2017**, *9* (6), 578-583.
19. Altman, A. B.; Brown, A. C.; Rao, G. D.; Lohrey, T. D.; Britt, R. D.; Maron, L.; Minasian, S. G.; Shuh, D. K.; Arnold, J., Chemical structure and bonding in a thorium(III)-aluminum heterobimetallic complex. *Chem Sci* **2018**, *9* (18), 4317-4324.
20. Boreen, M. A.; Lohrey, T. D.; Rao, G.; Britt, R. D.; Maron, L.; Arnold, J., A Uranium Tri-Rhenium Triple Inverse Sandwich Compound. *J Am Chem Soc* **2019**, *141* (13), 5144-5148.
21. Kiernicki, J. J.; Cladis, D. P.; Fanwick, P. E.; Zeller, M.; Bart, S. C., Synthesis, Characterization, and Stoichiometric U-O Bond Scission in Uranyl Species Supported by Pyridine(diimine) Ligand Radicals. *J Am Chem Soc* **2015**, *137* (34), 11115-25.

22. Koster, D. F.; Jones, W., Pascal Type Triangles for Nuclei with 1 Greater-Than 1/2. *J Chem Educ* **1982**, *59* (4), 289-289.
23. Gomtsyan, A., Heterocycles in drugs and drug discovery. *Chem Heterocycl Com+* **2012**, *48* (1), 7-10.
24. Cabrele, C.; Reiser, O., The Modern Face of Synthetic Heterocyclic Chemistry. *J Org Chem* **2016**, *81* (21), 10109-10125.
25. Baumann, M.; Baxendale, I. R., An overview of the synthetic routes to the best selling drugs containing 6-membered heterocycles. *Beilstein J Org Chem* **2013**, *9*, 2265-2319.
26. Vitaku, E.; Smith, D. T.; Njardarson, J. T., Analysis of the Structural Diversity, Substitution Patterns, and Frequency of Nitrogen Heterocycles among US FDA Approved Pharmaceuticals. *J Med Chem* **2014**, *57* (24), 10257-10274.
27. Xie, Y. J.; Wu, J.; Che, X. Z.; Chen, Y.; Huang, H. W.; Deng, G. J., Efficient pyrido[1,2-a]benzimidazole formation from 2-aminopyridines and cyclohexanones under metal-free conditions. *Green Chem* **2016**, *18* (3), 667-671.
28. Moore, J. N.; Healy, J. R.; Kraft, W. K., Pharmacologic and clinical evaluation of posaconazole. *Expert Rev Clin Phar* **2015**, *8* (3), 321-334.
29. Jalageri, M. D.; Nagaraja, A.; Puttaiahgowda, Y. M., Piperazine based antimicrobial polymers: a review. *Rsc Adv* **2021**, *11* (25), 15213-15230.
30. Shaquiquzzaman, M.; Verma, G.; Marella, A.; Akhter, M.; Akhtar, W.; Khan, M. F.; Tasneem, S.; Alam, M. M., Piperazine scaffold: A remarkable tool in generation of diverse pharmacological agents. *Eur J Med Chem* **2015**, *102*, 487-529.
31. Greer, N. D., Posaconazole (Noxafil): a new triazole antifungal agent. *Proc (Bayl Univ Med Cent)* **2007**, *20* (2), 188-96.
32. Nagappan, V.; Deresinski, S., Reviews of anti-infective agents: posaconazole: a broad-spectrum triazole antifungal agent. *Clin Infect Dis* **2007**, *45* (12), 1610-7.
33. Thompson, G. R., 3rd; Rinaldi, M. G.; Pennick, G.; Dorsey, S. A.; Patterson, T. F.; Lewis, J. S., 2nd, Posaconazole therapeutic drug monitoring: a reference laboratory experience. *Antimicrob Agents Chemother* **2009**, *53* (5), 2223-4.
34. McNair, T. J.; Wibin, F. A.; Hoppe, E. T.; Schmidt, J. L.; Depeyster, J. A., Antitumor action of several new piperazine derivatives compared to certain standard anticancer agents. *J Surg Res* **1963**, *3*, 130-6.

35. Capdeville, R.; Silberman, S.; Dimitrijevic, S., Imatinib: the first 3 years. *Eur J Cancer* **2002**, *38 Suppl 5*, S77-82.
36. Hull, L. A.; Giordano, W. P.; Rosenblat, D.; Davis, G. T.; Mann, C. K.; Milliken, S. B., Oxidations of Amines .8. Role of Cation Radical in Oxidation of Triethylenediamine by Chlorine Dioxide and Hypochlorous Acid. *J Phys Chem-Us* **1969**, *73 (7)*, 2147-&.
37. McKinney, T. M.; Geske, D. H., Triethylenediamine Cation Radical. *J Am Chem Soc* **1965**, *87 (13)*, 3013-&.
38. Hoffmann, R.; Imamura, A.; Hehre, W. J., Benzynes Dehydroconjugated Molecules and Interaction of Orbitals Separated by a Number of Intervening Sigma Bonds. *J Am Chem Soc* **1968**, *90 (6)*, 1499-&.
39. Staley, R. H.; Beauchamp, J.L., Relationship of Nitrogen Lone Pair Interactions to Thermodynamic Parameters Associated with Amine Basicities. *J Am Chem Soc* **1974**, *96 (5)*, 1604-1606.
40. Zheng, Z. R.; Evans, D. H.; Nelsen, S. F., Studies of the anodic oxidation of 1,4-diazabicyclo [2.2.2]octane. Reactions of the radical cation. *J Org Chem* **2000**, *65 (6)*, 1793-1798.
41. Heilbronner, E.; Muszkat, K. A., On Relative Importance of through-Space Vs through-Bond Interaction between Lone Pairs in 1,4-Diazabicyclo[2.2.2]Octane. *J Am Chem Soc* **1970**, *92 (12)*, 3818-+.
42. Bischof, P.; Hashmall, J. A.; Heilbronner, E.; Hornung, V., Nitrogen Lone Pair Interaction in 1,4-Diaza-Bicyclo[2.2.2]Octane. *Tetrahedron Lett* **1969**, (46), 4025-&.
43. Shida, T.; Nosaka, Y.; Kato, T., Electronic Absorption-Spectra of Some Cation Radicals as Compared with Ultraviolet Photoelectron-Spectra. *J Phys Chem-Us* **1978**, *82 (6)*, 695-698.